Titre: Title:	Spectroscopic diagnostics of atmospheric pressure dielectric barrier discharges
Auteur: Author:	Viorel Poenariu
Date:	2006
Type:	Mémoire ou thèse / Dissertation or Thesis
Référence: Citation:	Poenariu, V. (2006). Spectroscopic diagnostics of atmospheric pressure dielectric barrier discharges [Mémoire de maîtrise, École Polytechnique de Montréal]. PolyPublie. https://publications.polymtl.ca/7735/

UNIVERSITÉ DE MONTRÉAL

SPECTROSCOPIC DIAGNOSTICS OF ATMOSPHERIC PRESSURE DIELECTRIC BARRIER DISCHARGES

VIOREL POENARIU
DÉPARTEMENT DE GÉNIE PHYSIQUE
ÉCOLE POLYTECHNIQUE DE MONTRÉAL

MÉMOIRE PRÉSENTÉ EN VUE DE L'OBTENTION
DU DIPLÔME DE MAÎTRISE ÈS SCIENCES APPLIQUÉES
(GÉNIE PHYSIQUE)
AVRIL 2006

Your file Votre référence
ISBN: 978-0-494-17965-9
Our file Notre référence
ISBN: 978-0-494-17965-9

UNIVERSITÉ DE MONTRÉAL

ÉCOLE POLYTECHNIQUE DE MONTRÉAL

Ce mémoire intitulé :

SPECTROSCOPIC DIAGNOSTICS OF
ATMOSPHERIC PRESSURE DIELECTRIC BARRIER DISCHARGES

présenté par : POENARIU Viorel
en vue de l'obtention du diplôme de : Maîtrise ès sciences appliquées
a été dûment accepté par le jury d'examen constitué de :

M. BERTRAND Lionel, D. d'État, président
M. WERTHEIMER Michael R., D.Sc.A., membre et directeur de recherche
M. BARTNIKAS Raymond, Ph.D., membre et codirecteur de recherche
M. MOISAN Michel, Ph.D., membre

REMERCIEMENTS

Je tiens tout d'abord à remercier mon directeur de recherche, le professeur Michael Wertheimer, pour m'avoir accepté, soutenu et guidé tout au long de ma maîtrise. Ses conseils judicieux, sa rigueur scientifique, sa disponibilité ainsi que sa bienveillance m'ont grandement aidé et encouragé.

Je voudrais aussi remercier mon codirecteur de recherche, Dr Ray Bartnikas. Ses conseils ainsi que ses encouragements ont été fort appréciés.

Je remercie également les autres membres du jury, le professeur Lionel Bertrand pour avoir bien voulu accepter la présidence et le professeur Michel Moisan pour l'intérêt qu'il a manifesté pour cette recherche.

Je tiens à remercier la professeure Suzanne Lacroix pour son aide concernant la mise-au-point d'un montage expérimental et pour le prêt de certains composants optiques.

Je tiens à remercier aussi le Dr Véronique François (École de Technologie Supérieure) pour son support et encouragements.

J'aimerais remercier Cornelia, Florina, Rodica, Pierre-Luc, Luke, Gregory, Mohamed, Ion et tous les autres, tout spécialement Yves pour son support technique et son amitié.

Enfin, je tiens à remercier Anca et Florin du fond du cœur pour le bonheur qu'ils m'apportent quotidiennement et pour le support qu'ils m'ont donné durant cette maîtrise.

RÉSUMÉ

L'objectif de cette recherche était l'évaluation de la température, T, dans une décharge à barrière diélectrique (DBD) en utilisant la spectroscopie d'émission optique (OES), qui a le grand avantage d'être non perturbatrice. Nous arrivons à ce résultat en analysant le spectre rotationnel qui provient d'une espèce moléculaire excitée dans la décharge. Dans le passé, plusieurs molécules ont été utilisées pour mesurer la température du gaz dans la décharge; parmi elles, la molécule la plus souvent utilisée a été N_2 avec ses deux bandes rotationnelles d'émission les plus connues : Le Deuxième Système Positif (SPS) de N_2 et le Premier Système Négatif (FNS) de l'ion N_2^+. Ce dernier a l'avantage que sa structure rotationnelle peut être bien résolue même en utilisant un spectrographe de performance moyenne, et la température rotationnelle, T_{rot}, peut être facilement déterminée à l'aide d'un diagramme de Boltzmann conventionnel.

En utilisant un système expérimental pour l'observation des DBD, nous avons étudié les décharges à pression atmosphérique dans l'He ou mélanges de He et N_2. Ces décharges, excitées par une haute tension alternative (~ kV) à fréquence audio (1 – 10kHz), ont été créées dans quatre différentes configurations d'électrodes : plane, cylindrique, sphérique et aiguille pour l'électrode supérieure à haute tension, et plane pour l'électrode inférieure. Cette dernière, qui est mise à la terre à travers une résistance de 50 Ω, est couverte par un diélectrique qui limite le courant de la décharge. Les spectres optiques d'émission ont été acquis à l'aide d'un spectrographe ayant une distance focale de 0,5 m et d'un détecteur ICCD; une camera numérique ultra-rapide a permis l'enregistrement d'images avec des temps d'exposition allant jusqu'à 2,5 ns. En utilisant la branche R de FNS $N_2^+(B^2\Sigma_u^+, v'=0 \rightarrow X^2\Sigma_g^+, v''=0)$, nous avons déterminé la distribution axiale et radiale de T_{rot} dans des décharges luminescentes à pression atmosphérique (APGD) dans les différentes configurations géométriques d'électrodes, différents espacements d'électrodes et pour différentes pressions partielles de N_2 dans l'He.

Même si le réacteur de la décharge est alimenté avec un écoulement d'He pur à un taux relativement élevé de 5,7 litres standards par minute (slm), la concentration d'impureté de N_2 est suffisante pour une bonne précision de mesure de T_{rot}. Les résultats expérimentaux montrent une augmentation presque linéaire de T_{rot} avec l'accroissement jusqu'à ≈ 1 vol % de la concentration de N_2 dans l'He. La valeur de T_{rot} à mi-distance entre les électrodes est en accord avec la

littérature scientifique, tandis que les valeurs de T_{rot} proches des deux électrodes sont sensiblement plus grandes dans le cas de la configuration plan-plan. Si l'espacement entre les deux électrodes est réduit, la valeur de T_{rot} augmente substantiellement, à cause de la diminution du transfert thermique. Les résultats expérimentaux obtenus dans d'autres configurations géométriques des électrodes sont aussi présentés, ainsi que des images qui montrent l'évolution spatio-temporelle soit de l'émission lumineuse totale, soit de certaines espèces excitées dans la décharge. L'interprétation physique des ces résultats est présentée, avec référence à d'autres travaux publiés par ce laboratoire et par d'autres auteurs, contribuant à la compréhension de la physique des décharges à pression atmosphérique.

ABSTRACT

The purpose of this research has been to measure temperature, T, in dielectric barrier discharges (DBD) using optical emission spectroscopy (OES), which has the great advantage of being non-intrusive and non-perturbing. This is accomplished by analyzing high-resolution rotational bands in the emission spectra of suitable electronically-excited molecular species in the discharge. Several molecules have in the past been used for this purpose, but the most frequently studied are nitrogen bands from the Second Positive System (SPS) of N_2 and the First Negative System (FNS) of N_2^+. The latter has the advantage that rotational structure can be fully resolved even with a spectrograph of average performance, and that the rotational temperature, T_{rot}, can be determined from a conventional Boltzmann plot.

Using a glass-walled DBD apparatus, we have studied atmospheric pressure discharges in flowing helium (He) or He/N_2 mixtures, these being excited by audio-frequency (1 to 10 kHz) high voltage (HV). Four different metallic HV electrode geometries have been examined, namely planar, cylindrical, spherical and needle, the grounded dielectric-covered electrode being planar. OE spectra were acquired with a 0.5 m focal length spectrograph, coupled to an intensified charge coupled device (ICCD) detector. Using the (0-0) R-branch of FNS $N_2^+(B^2\Sigma_u^+ - X^2\Sigma_g^+)$ bands near 391 nm, we have measured radial and axial distributions of T_{rot} for different electrode geometries, gap spacings and He-N_2 gas mixture compositions.

Even in a flow of nominally very pure He, N_2 impurity at the ppm level is sufficient to yield high enough spectral intensity for accurate T_{rot} measurements, T_{rot} increasing linearly with rising N_2 concentration (up to ~ 1 vol %). Mid-gap T_{rot} values agree well with literature data, while those at the two electrode surfaces are appreciably higher in the 3.0 mm wide plane-plane gap. If the inter-electrode gap is narrowed, T_{rot} of pure He flow is seen to rise substantially, as expected, on account of reduced heat transfer. Results are also presented for the other electrode geometries, including spatiotemporally- and spectrally-resolved measurements. The physical interpretations of these results are discussed with reference to recent work from this laboratory and that reported by others. These provide much additional fundamental information about the discharge physics.

CONDENSÉ EN FRANÇAIS

Au cours des dernières années, l'étude de décharges à barrière diélectrique (DBD) est devenue un thème de plus en plus important en recherche sur les plasmas dans le monde, à cause de la possibilité de réduire le coût des applications utilisant le plasma à basse pression, qui ont besoin de systèmes à vide dispendieux.

La DBD est un plasma « froid » à pression atmosphérique, pouvant opérer en mode « filamentaire » ainsi que diffus. La décharge est obtenue dans l'espace entre deux électrodes dont au moins l'une (ou les deux) est couverte par un diélectrique. Normalement, une DBD à pression atmosphérique est une décharge filamentaire, mais en 1968, Bartnikas [17-19] a rapporté l'existence d'une décharge luminescente uniforme dans l'He, dite « Atmospheric Pressure Glow Discharge (APGD) », c'est-à-dire « décharge luminescente à pression atmosphérique », caractérisée par une seule impulsion de courrant par demi-cycle de la tension alternante appliquée. Ultérieurement, plusieurs chercheurs dans différents laboratoires ont rapporté des décharges uniformes à pression atmosphérique dans d'autres gaz ou mélanges gazeux [20-33]. La plupart des recherches ont été faits sur l'He, puisqu'il représente un milieu gazeux inerte, c'est à dire sans réactions chimiques et sans problèmes de décomposition, donc un gaz qui peut être relativement facilement étudié et modélisé.

Les phénomènes qui ont lieu dans un plasma froid à pression atmosphérique sont très complexes, même dans le cas de l'He, et ils ne sont pas encore très bien compris. La température du gaz dans la décharge est évidemment un paramètre très important pour plusieurs applications, puisqu'une température trop élevée peut causer la destruction de matériaux thermo-sensibles comme, par exemple, les polymères.

L'objectif de cette recherche a été de déterminer la température du gaz dans des APGDs en utilisant la spectroscopie d'émission optique (OES), qui a l'avantage d'être une technique diagnostique non perturbatrice. Ceci a été accompli en utilisant le spectre rotationnel provenant du « First Negative System » (FNS) $N_2^+(B^2\Sigma_u^+,\ v'=0 \rightarrow X^2\Sigma_g^+,\ v''=0)$ qui a l'avantage de pouvoir être résolu même avec un spectrographe de performance moyenne. La température rotationnelle, T_{rot}, peut alors être déterminée simplement à partir d'un graphique de Boltzmann conventionnel.

Nous avons restreint cette étude à l'He et aux mélanges He/N_2 pour ce qui est de l'évaluation de la température du gaz, et aux gaz He, Ne et N_2 pour l'analyse des évolutions spatiales de l'émission lumineuse totale provenant de la décharge, ces dernières en utilisant une camera numérique ultra-rapide. En plus, nous avons considéré seulement les décharges luminescentes uniformes, caractérisées par une seule impulsion par demi-cycle, ou celles caractérisées par plusieurs impulsions par demi-cycle, décharges dites « pseudo-glow ».

Nous avons modifié l'appareillage expérimental décrit dans les publications de Radu *et al* [21, 22, 28, 29, 31] pour nos fins actuelles. Les décharges ont étés obtenues dans quatre différentes configurations géométriques, dépendant de celle de l'électrode métallique supérieure : plane, cylindrique, sphérique et aiguille; l'électrode inférieure, reliée à la terre par une résistance de faible valeur servant à mesurer le courant de la décharge, avait une géométrie plane et elle était couverte d'un diélectrique.

Les spectres d'émission ont été enregistrés à l'aide d'un spectrographe avec une distance focale de 0,5 m, couplé à un détecteur ICCD numérique très rapide (avec un temps d'exposition allant jusqu'à de 2,5 ns) et très sensible Ce détecteur fait aussi partie de la camera ultra-rapide permettant la détection de signaux lumineux très faibles et l'accumulation de signaux périodiques. La lumière provenant de la décharge fut dirigée vers la fente du spectrographe à l'aide d'un dispositif optique mobile, capable de fournir une résolution spatiale d'environ 100 µm. Cependant, afin d'obtenir un meilleur rapport signal/bruit, la plupart des expériences ont été réalisées avec une résolution spatiale de 250 µm.

Les spectres d'émission provenant d'APGDs ont été enregistrés entre λ = 350 nm (limité par la sensibilité du détecteur ICCD et par la paroi en verre « pyrex » du réacteur) et 860 nm et ils ressemblent à ceux rapportés dans la littérature [33]. Dans tous les spectres de décharges dans l'He ou de mélanges de He/N_2, on observe les bandes « Second Positive System » (SPS) $N_2(C^3\Pi_u - B^3\Pi_g)$ et FNS $N_2^+(B^2\Sigma_u^+ - X^2\Sigma_g^+)$, le triplet de l'oxygène correspondant à la transition $3^5P \rightarrow 3^5S$ à λ = 777 nm, et la transition $3^3S \rightarrow 2^3P$ à λ = 706,5 nm qui provient de l'He. La plus intense émission provient de la bande P du système $N_2^+(B^2\Sigma_u^+, v'=0 \rightarrow X^2\Sigma_g^+, v''=0)$ à 391,44 nm. Dans plusieurs décharges l'on remarque la présence d'autres raies d'émission de l'He : 667,8 nm ($3^1D \rightarrow 2^1P$), 587,6 nm ($3^3D \rightarrow 2^3P$) ou 388,8 nm ($3^3P \rightarrow 2^3S$).

La température rotationnelle, T_{rot}, a été déterminée à partir de la bande R du système FNS $N_2^+(B^2\Sigma_u^+, v'=0 \rightarrow X^2\Sigma_g^+, v''=0)$ en utilisant la méthode du graphique de Boltzmann. L'intensité de chaque raie de la bande R utilisée pour cette fin est le résultat d'une moyenne sur 25 mesures.

Nous avons déterminé les distributions axiale et radiale de T_{rot} dans la décharge en fonction de la distance entre les électrodes, d, de l'amplitude, V_{pp}, et la fréquence, f, de la tension alternative appliquée, et en fonction de la pression partielle de N_2 dans l'He, et ceci dans les configurations géométriques suivantes : aiguille-plan, cylindre-plane, sphère-plan et plan-plan. La température cinétique du gaz, T, est supposée être égale à T_{rot}, hypothèse confirmée par plusieurs travaux publiés dans la littérature [38, 106, 107]. Nous avons observé une augmentation linéaire de T_{rot} en augmentant jusqu'à environ 1 vol % la concentration de N_2 dans l'He. Les valeurs de T_{rot} à mi-distance entre les électrodes planes s'accordent avec celles tirées de la littérature, alors que les valeurs de T_{rot} proches des deux électrodes sont sensiblement plus grandes. Si la distance entre les électrodes, d, est réduite, la valeur de T_{rot} augmente substantiellement à cause du transfert thermique réduit. Les résultats expérimentaux obtenus dans d'autres configurations géométriques des électrodes sont aussi présentés dans ce mémoire, ainsi que des images montrant l'évolution spatio-temporelle de l'émission lumineuse totale, ou celles provenant de certaines espèces excitées dans la décharge. L'interprétation physique des ces résultats est présentée avec référence aux récents travaux de notre propre laboratoire et ceux publiés par d'autres auteurs. Enfin, nous croyons que cette recherche contribue de façon significative à la physique des décharges luminescentes dans les gaz à pression atmosphérique.

TABLE OF CONTENTS

LIST OF FIGURES

LIST OF SYMBOLS

a.c.	Alternative current
a_i	Fractional flow values of gases i
$A_{J'J''}$	Einstein transition probability
APGD	Atmospheric Pressure Glow Discharges
$B_{v'}$	Rotational constant
c	Velocity of light
C	Capacitor of test
CCD	Charge Coupled Device
C_d	Dielectric equivalent capacitance
C_g	Gas gap equivalent capacitance
c_{pi}	Specific heats at constant pressure
d	Gap length
d.c.	Direct current
DBD	Dielectric Barrier Discharges
DLAS	Diode-Laser Absorption Spectroscopy
$D_{v'}$	Rotational constant
f	Frequency of applied voltage
F(J')	Rotational term
FDBD	Filamentary Dielectric Barrier Discharge
FNS	First Negative System
γ	Secondary electron emission coefficient
GCF	Gas correction factor
GDBD	Glow Dielectric Barrier Discharge
h	Planck's constant
HV	High Voltage
I	Emission intensity
I(391)	Intensity of R-band bandhead at 391.44nm
ICCD	Intensified Charge Coupled Device

i_d	Discharge current
$I_{J'J}$	Intensity of a spectral line in emission
I_{PM}	Photomultiplier signal
J', J"	Rotational quantum number
k	Boltzmann's constant
K	Total angular momentum apart from spin
l	Dielectric thickness
Λ	Angular momenta
LIF	Laser-Induced Fluorescence
LTE	Local Thermodynamic Equilibrium
MFC	Mass Flow Controller
N	Number of molecules
$N_{J'}$	Number of atoms in the initial state, J'
$\nu_{J'J"}$	Wavenumber
OES	Optical Emission Spectroscopy
PDP	Plasma Display Panels
PM	Photomultiplier
ppm	Part per million
q(t)	Charge transferred across the electrode gap
Q_r	Rotational state sum (or partition function)
r	Radius
R	Resistor connected in series with the unbiased electrode and ground
R_g	The equivalent gas gap resistor
$R^{J'J"}$	Matrix element of the electrical dipole moment
S	Quantum number of spin
sccm	Standard cube centimetres per minute
SEE	Secondary Electron Emission
s_i	Molecular structure factors
$S_{J'}$	Line strength
slm	Standard litres per minute
SPS	Second Positive System

T	Temperature
t	Time
t_m	Time for the PM intensity to reach its maximum
t_p	Discharges front to propagate from the needle tip to the dielectric surface
T_{rot}	Rotational temperature
$u_{app}(t)$	Applied voltage
$u_d(t)$	Voltage across the dielectric
$u_g(t)$	Voltage across the gas gap
UHSI	Ultra-High Speed Imaging
$u_m(t)$	Memory voltage
$u_m(t_0)$	Voltage determined by the charge accumulated on the dielectric surface from the previous discharge
$u_R(t)$	Voltage across the resistor R
$u_T(t)$	Voltage across the test capacitor
UV	Ultra-Violet
V	Amplitude of the applied voltage
v', v"	Vibrational quantum numbers of the upper and lower vibrational state
V_b	Breakdown voltage
VLSI	Very-Large-Scale Integrated Circuits
V_{pp}	Voltage across the test cell
V_r	Residual voltage
V_R	Voltage across the resistor R
z	Axial position

LIST OF APPENDIXES

Chapter 1 INTRODUCTION

1.1 Background

Nonequilibrium plasma has become an essential tool in the production of advanced microelectronics such as semiconductors, optical and photovoltaic devices. The manufacturing of very-large-scale integrated circuits (VLSI) computer chips, or the development of materials with special properties such as amorphous silicon or diamondlike carbon has become possible due to plasma technology. However, most of the technological processes operate at low-pressure, between 0.01 and 10 Torr, which requires expensive and time-consuming vacuum system. The reduction of production costs and the facilitation of integration into production lines can in principle be realised by using nonequilibrium atmospheric pressure plasma, for example dielectric barrier discharges (DBD).

For a long period of time the primary application of DBD was in industrial ozone generation, used mainly in water treatment. However, in the last few years, as a result of extensive research activity started around 1970 and of technical progress in diagnostics and modeling tools, this "cold" non-equilibrium plasma at atmospheric pressure has begun to have new fields of applications such as modification and etching of polymers surfaces [1, 2], deposition of thin films [3, 4, 5], plasma display panels (PDP) [6, 7], synthesis of aligned carbon nanotubes [8], mercury-free fluorescent lamps and excimer lamps [9], abatement of pollutants from gaseous and aqueous media [10-12], biological applications (sterilization or decontamination) [13], even applications in VLSI [14, 15], etc.

The DBD, known also under the name of "silent discharge" due to the absence of sparks, is an atmospheric pressure cold plasma that can operate in both filamentary and diffuse modes. This discharge is obtained in the gap between two electrode surfaces, at least one of which is covered by a dielectric; it is a non-thermal plasma with high selectivity and energy efficiency, useful in numerous plasma-chemical reactions such as the ones mentioned above, and others [16].

Usually, high pressure DBD under ac conditions is a constricted channel (spark-type) discharge that occurs randomly over the dielectric surface, producing a charge transfer at each discharge

site on the electrodes. The intervening gas between the discrete discharges within each ac cycle is not ionized and absorbs part of the energy dissipated in the discharge channel. In 1968 Bartnikas [17-19] reported that ac discharges in helium can also manifest "glow" or pulsed "pseudoglow" regimes, now often termed "atmospheric pressure glow discharges" (APGD), on account of their spatially homogenous appearance. The glow discharges are characterized by a single multi-μs current pulse per half cycle, in contradistinction to the pseudoglow mode that is typified by a train of current pulses of usually diminishing amplitude, with the width of each pulse representing the duration of the glow discharge that extends over the entire surface of the electrodes [17-22]. Since then, APGD has also been reported in other gases and gas mixtures, namely Ar, Ne, Kr, N_2, O_2, air, Xe/Cl_2, and SF_6 [20-33]. A large number of studies on APGD were carried out on He, because it constitutes a convenient inert gas medium on which parametric ionization data are readily available for modeling of the spark-to-glow discharge transition mechanism, and by itself it represents an appropriate test gas free of any chemical reaction and decomposition problems [34-36]. In spite of its relatively high cost, He is used in some technological applications [37].

The phenomena occurring in atmospheric pressure cold plasma are very complex and not yet fully understood. There are numerous parameters that must be well controlled in order to achieve required results in terms of processing and materials properties. One of these parameters, necessary in both theoretical simulation and practical applications, is the translational temperature of neutral species in the discharge. Measurement of the gas temperature in the active glow discharge zone is evidently of practical relevance because, for example, excessively high temperatures may cause damage to thermally-sensitive materials in surface treatment-related applications. But accurate evaluation of the kinetic temperature of neutral particles is not straightforward, since conventional thermocouple-type sensors are not suitable for use in plasmas. Alternative methods, which are amenable for plasma work, are based on optical techniques such as absorption, laser-induced fluorescence (LIF) and optical emission spectroscopy (OES). The first two methods, which generally monitor the ground state of the species, may be employed to measure the real temperature of the neutral gas; however they require equipment that is not usually compatible with industrial applications. On the other hand, OES provides information concerning the excited states, with the consequence that the temperature measured may not necessarily represent the true gas temperature. However, OES

has the decided advantage of being a non-intrusive and non-perturbing procedure. Temperature measurement, deploying OES, is accomplished by the analysis of high-resolution rotational bands in the emission spectra of suitable electronically-excited diatomic molecular species present in the discharge. Among the most frequently utilized bands are those from the Second Positive System (SPS) of N_2 and the First Negative System (FNS) of N_2^+ [38]. The latter has the advantage that the rotational structure can be fully resolved even with a spectrograph of average performance. The gas temperature, which at atmospheric pressure is assumed to be equal to the rotational temperature, T_{rot}, can be determined from a conventional Boltzmann plot.

We have confined the present study to He, either pure or with small deliberate admixtures of N_2 for gas temperature evaluation, and to He, Ne and N_2 in the case of high-speed image analyses, restricting it further to deal only with glow and pseudo-glow discharges. The radial and axial temperature distributions, obtained as a function of gap spacing, amplitude and frequency of applied voltage and partial pressure of N_2 in He in point-plane, cylinder-plane and plane-plane electrode systems are evaluated and compared. The spatial and temporal evolutions of the emission intensity from different radiative species present in discharge and of the total emission light are also presented.

The first part of this work deals with a review of literature about the phenomenology of DBD and APGD, their applications and the diagnostic methods. Much attention is paid to the technique of gas temperature determination from the rotational emission spectra of diatomic molecules by using OES. In the second part, the experimental arrangement, the analytical methods, and the errors of the temperature determination are presented.

The results and their interpretation are presented in the last part of this thesis, along with a comparison with result from the literature. The most important results of this research and the suggestion for future studies are reviewed in the conclusion.

1.2 DBD at atmospheric pressure

The DBD is a strongly nonequilibrium[1] plasma produced in a gas at high pressure (usually atmospheric pressure) between the surfaces of two electrodes, at least one of which is covered by a dielectric (Fig. 1.1). Much of the earlier work has dealt with parallel planar electrodes [17-22, 25, 33], but other geometries have also been examined, e.g. needle-plane [28, 32], brush-plane [39], mesh-plane [40], and cylinder-plane [27, 29, 30]. The presence of a dielectric material between the two metallic electrodes calls for an ac or pulse applied voltage in order to obtain the

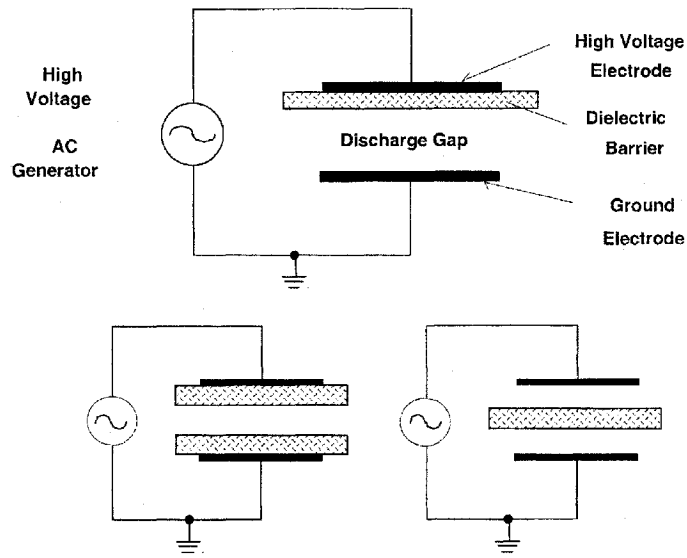

Figure 1.1 A few examples of DBD electrode configurations [23].

discharge. The distance between the electrodes is usually between 0.1 mm and some centimetres, depending upon the application, and the discharge is sustained by using a high a.c. voltage with frequency, f, usually between 50 Hz and 500 kHz [41]. In most gases at atmospheric pressure the DBD is a filamentary discharge characterized by a large number of short-lived (~ 10 ns) and

[1] Plasma that is not at local thermodynamic equilibrium (non-LTE); a system is not in local thermodynamic equilibrium if the local kinetic (Maxwellian) temperature is not equal to the Planckian temperature of the radiation field.

narrow micro-discharges[2] (each micro-discharge comprising an almost cylindrical plasma channel with radius of ~ 100 μm) randomly distributed over the dielectric surface (Fig. 1.2). A typical micro-discharge density is 10^6 $cm^{-2}s^{-1}$ [42], depending upon the power density and UV radiation emission. However, in some gases and certain narrowly defined experimental conditions, DBD can manifest (even at high pressure) an apparently homogeneous nature, usually called APGD because of its similarity with a low-pressure dc glow discharge [20-33].

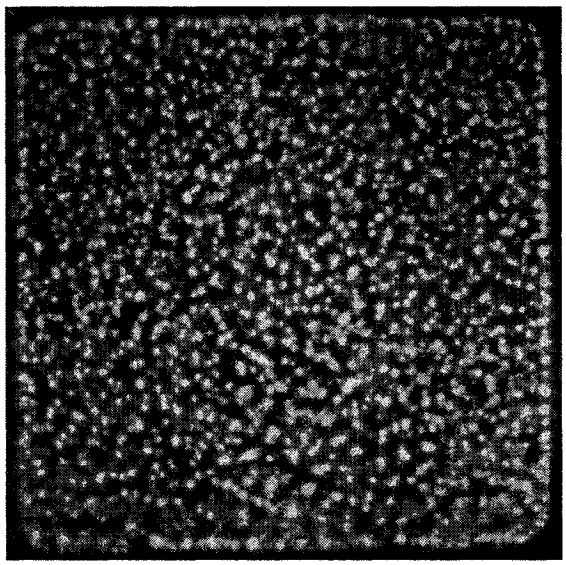

Figure 1.2 The most common appearance of a filamentary DBD at atmospheric pressure (original size: 6 cm x 6 cm, exposure time: 20 ms) [16, 23].

When the ac voltage is applied at the high-voltage electrode of the test cell, the electrical field created determines the acceleration of all the charged species in the gap. The initial electrons and ions can result from cosmic radiation or natural radioactivity, but can also be deliberately created using different techniques, or can be the result of discharges from the previous half-cycle of applied voltage (from direct electron collisions, or indirectly, for instance by Penning

[2] Under the influence of the electrical field, electronic collisions with the gas species produce secondary electrons and develop an avalanche. If the avalanche is large enough, a streamer towards the cathode is usually born near the anode. It traverses the gap in some nanoseconds and forms a conductive channel of weakly ionized plasma. A current flows through this channel until the local electrical field collapses as a result of charge accumulation on the dielectric surface. All the local processes initiated by the avalanche and developed until the electron current ceases is usually called a micro-discharge [41].

ionisation). The energetic electrons collide with the neutral particles in the gap and modify their electronic states by processes such as ionisation, excitation, and emission of radiation. If the electrical field becomes higher than the breakdown field, the growth of electron avalanches develops very rapidly and local breakdown in the gap is initiated [23, 43-47]. The current that flows through their narrow conductive channels which link the two electrodes, rapidly transfers charge to the dielectric surface, which, in turn, reduces the local field, and extinguishes the micro-discharge [16]. When the high-voltage polarity changes, the zone where a discharge occurred in the previous polarity favours the initiation of a new one. This situation determines the formation of a filament[3] in DBD.

A filament can be characterized by a transition glow discharge that develops a cathode fall of only some micrometers (~ 10 μm) in the gas gap [45-47] and a positive column [16]. At atmospheric pressure the instantaneous electron density in the filament channel is about $10^{14} \div 10^{15}$ cm^{-3}, and the current density is between 100 and 1000 A cm^{-2} [43, 44]. The typical quantity of charge that flows through a filament is about 100 pC and it depends on the gap dimension, dielectric properties, and mostly on the ionisation properties of the gas; however, the charge transported through the gap does not depend on the gas pressure [43]. This charge spreads on the dielectric surface well beyond the filament diameter, depending upon the surface coupling capacity of the dielectric, and it will affect the electrical field in that zone. The energy dissipated in one micro-discharge is only a few μJ [43-45] and has a relatively little effect on gas heating.

[3] A filament in a DBD is a group of micro-discharges that occur in the same location each time when the polarity of the applied voltage is changing [41].

1.3 Atmospheric pressure glow discharge

The APGD represents a uniform discharge produced in a DBD configuration that covers the entire electrode surfaces during each current pulse. This spatially homogeneous discharge has been named "glow discharge" because of its similarity to the low-pressure dc glow discharge.

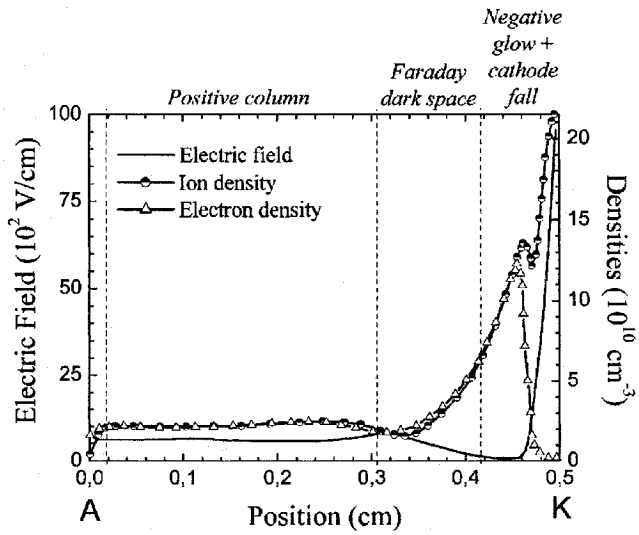

Figure 1.3 Calculated space distribution from the anode to the cathode of the electrical field, the ion and electron densities in a He GDBD when the discharge current intensity is maximum [33].

Indeed, using one-dimensional simulation, Massines *et al* [33] determined the spatial distributions of the electrical field and the densities of electrons and He^+ ions across a 5 mm gap in helium APGD produced in a planar electrode configuration; when the current through the discharge has its maximum value, these strongly resemble a d.c. glow discharge (Fig. 1.3). The electrical field in the gap is uniform before the breakdown, similar to a Townsend discharge; then, with increasing ionisation, an accumulation of ions occurs near the cathode surface and results in the formation of the cathode fall, the width of which diminishes with increasing applied voltage, V_{pp}. However, the presence of the dielectric in the circuit indirectly limits the width of the cathode fall to about 400 nm, much greater than in the case of a low-pressure glow discharge [33]. This suggests that APGD in He is a sub-normal glow discharge [33]. The

discharge presents a region of high luminosity near the instantaneous cathode, and also one of relatively low emission intensity, characteristic to the positive column where the number densities of electrons and ions are equal [25]. In the cathode fall, the electric field reaches about 15 kV/cm, and the maximum ion density reaches 2 x 10^{11} cm^{-3}. The Faraday dark space covers a width of about 1.1 mm, and the positive column of quasi-neutral plasma is about 2.7 mm wide, with a nearly constant electric field of 700 V/cm. The maximum electron density of 10^{11} cm^{-3} is observed in the negative glow, where their mean free path length is a few μm [48]. This kind of discharge has been observed in inert gases such as He and Ne, and in other gases [20-33, 49].

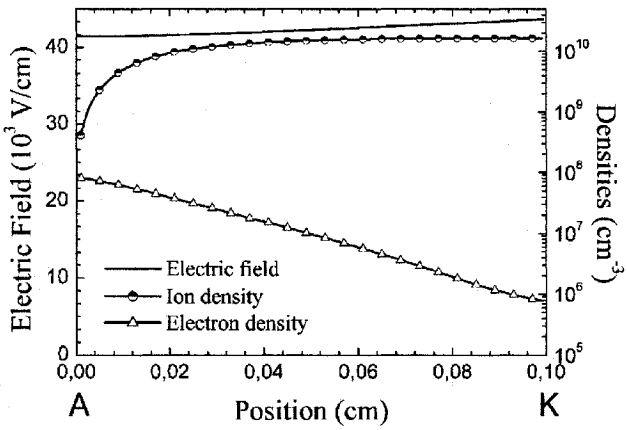

Figure 1.4 Calculated space distribution from the anode to the cathode of the electrical field, the ion and electron densities in a N_2 GDBD when the discharge current intensity is maximum [33].

However, not all homogeneous discharges at atmospheric pressure are like glow discharges. For example, the uniform discharge produced in N_2 in most cases has the structure of a Townsend discharge[4] (Fig. 1.4) [33, 50]. The latter is characterized by the absence of the positive column, i.e. the quasi-neutral region of the discharge, by a low density of charged species, and by a net positive charge. Also, the highest luminous emission intensity occurs in the vicinity of the anode. The level of ionization is much lower than in the previous case, and the ion density of

[4] In a Townsend discharge the electrical field is constant and the electrons have almost the same energy in the entire gap; a small variation in the applied voltage leads to a large variation in the current.

only 10^{10} cm^{-3} is not enough to localize the electrical field. The electron density increases from cathode to anode where it reaches its maximum value of about 10^{8} cm^{-3}. The current through the discharge is low (~ mA) and can have only one peak [51] during a half-cycle. This kind of discharge, that usually develops in a short gap and when the dielectric with a low associated capacity is used [52], has been observed in many gases [24, 53].

The main difference between the two kinds of discharges, glow and Townsend discharges, is the influence of the space charge on the electric field: In a Townsend discharge space charge has insignificant influence on the electric field, except at the instant of maximum current flow, while in the case of glow discharge, the density of charged particles is very high; here, the electric field is highly perturbed, resulting in the formation of the cathode layer and positive column [52].

There are two possible mechanisms for developing a uniform discharge. First, a high pre-ionisation of the gas permits a large number of avalanches to develop at the same time. These interact with one another and form a single, large-diameter discharge channel [54, 55]. This is the "streamer coupling" mechanism of breakdown, which has been propounded to explain the columnar discharge patterns observed across electrode surfaces. The second mechanism, the one that produces a Townsend-type discharge, is governed by secondary electron emission resulting from the impact of ions, metastables, neutrals and photons on the cathode surface [25]. Only this latter mechanism permits glow discharge development in a gas at atmospheric pressure, according to the one dimensional modeling studies of Massines *et al* [33]. This conclusion is substantiated by earlier antecedent results obtained with a two dimensional model, that was employed to examine the spark to glow transition process in short gaps [34, 56, 57]. This model permitted to analyze the discharge channel expansion process and determine the particle density distributions in the radial and axial directions with time as a parameter. Similar results were also obtained by applying the two dimensional model to asymmetrical electrode systems. [25-31].

According to the same authors, the presence of a positive column is necessary to obtain a discharge with a uniform character, since it retains electrons from one discharge pulse to the next and maintains the minimum level of pre-ionisation required for the development of a future uniform discharge [33]. Nersisyan *et al* [58] consider that in order to produce a uniform DBD, rapid amplification of primary electron avalanches must be avoided [58]. Roth proposed another explanation for the APGD, considering the mechanism of ions trapped in the gap, based on the correlation between ion mobility and the frequency of the applied voltage [26, 59].

Theoretical and experimental studies have yielded many characteristic parameters of filamentary and uniform DBDs, such as current-voltage characteristics, the plasma dynamics, the ranges of charged particle densities and certain aspects of plasma chemistry. Despite these, deep understanding of the fundamental underlying processes and of the mode of operation in the steady-state regime at atmospheric pressure is still far from being complete.

1.4 Characteristics of APGD in He and N_2

1.4.1 Electrical characteristics

In both He and N_2, by adjusting the discharge parameters, APGD can be characterized by a single current peak per half-cycle. For instance in a planar electrode configuration, the current through the APGD in He has an abrupt rise and has 5 times higher amplitude and 10 times shorter duration than in N_2 (Fig. 1.5) [33, 52, 60]. This results from the augmentation of the electric field near the cathode (cathode layer) that increases with rising current value (or decrease of the cathode layer thickness). The voltage across the gap in He begins to decrease immediately after the breakdown, and becomes almost zero at the end of the discharge peak (Fig. 1.6), while in N_2 the voltage across the gap still increases about 20% after the gas breakdown, after which it remains constant up to the end of the current peak (Fig.1.7) [33]. A 2D simulation of APGD produced in He between a cylindrical metallic high-voltage electrode and a planar dielectric surface (Al_2O_3) separated by a 3 mm gap showed that the ionic and electronic components of discharge current are near-equal during the peak of the negative half-cycle, but that the electronic component is four times higher than the ionic one in the positive half-cycle (Fig. 1.8) [30].

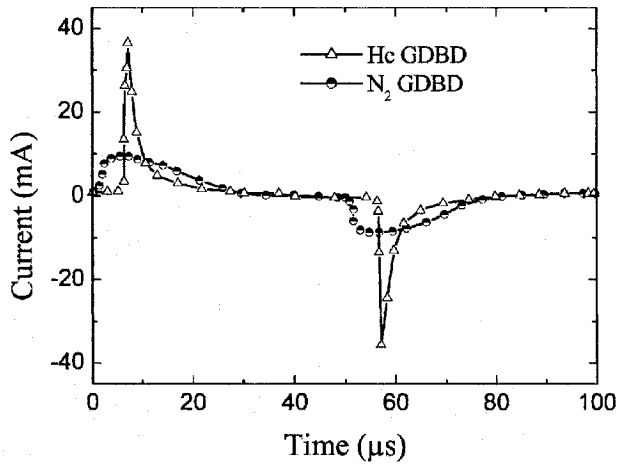

Figure 1.5 Current pulses across the gap in N_2 and He APGDs [33]

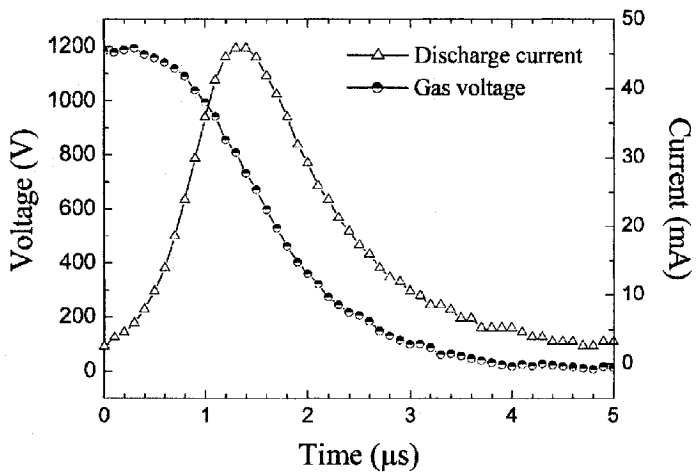

Figure 1.6 Time evolutions of the voltage across the gap and the current through He APGD in a planar electrode configuration [33].

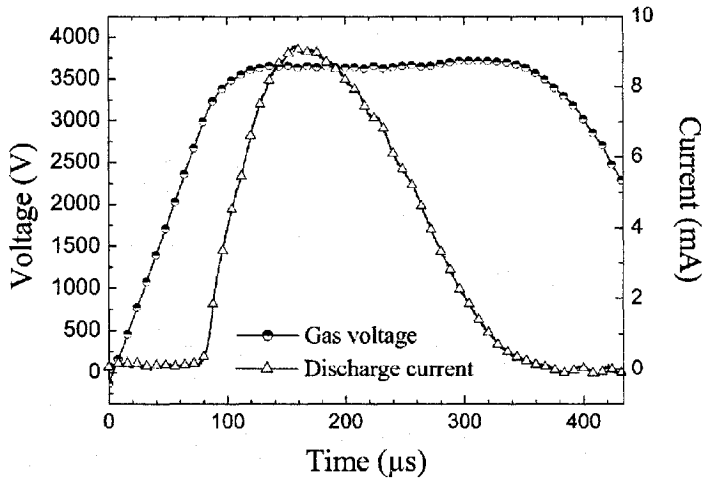

Figure 1.7 Time evolutions of the voltage and current across the gap for N_2 APGD in a planar electrode configuration [33].

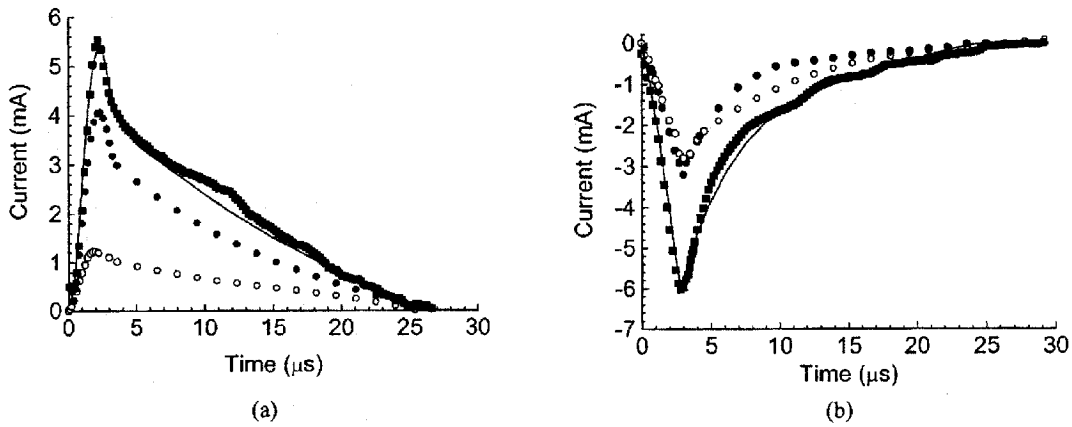

Figure 1.8 Pulse forms of the experimentally (■) and theoretically (–) determined electrical discharge current, and of its calculated electronic (●) and ionic (○) charge carrier components in the cylinder-plane geometry, for positive (a) and negative (b) polarity pulses of a glow discharge in helium under atmospheric pressure, with d = 3.0 mm and f = 10 kHz [30, 31].

1.4.2 Spatial and temporal evolutions

In the last few years, the use of high-speed cameras made it possible to study the temporal and spatial light distributions in the discharge gaps and to better understand the physics of APGD. For instance, a 10 ns exposure image recorded during the maximum value of current through a He APGD obtained in a 5 mm wide gap shows three distinct zones (Fig. 1.9): a wide luminous zone near the anode, followed by a dark zone, and near the cathode a thin layer of much higher luminous intensity [33]. Such structure is similar to that of a low-pressure glow discharge, as remarked earlier, the three zones being the positive column, the Faraday dark space and the cathode layer, together with the negative glow. A uniform discharge produced in Ar/NH_3 mixture (100 ppm NH_3, Fig. 1.10) shows a similar structure as that obtained in pure He [61]. Nozaki *et al* [62] have reported similar results from APGD in He/CH_4 mixture (98% He and 2% CH_4) between 1 mm-spaced planar electrodes, one metallic, the other one covered with a dielectric material (0.5 mm thick Pyrex glass). The images with 1 μs exposure time recorded during the positive and negative period of a discharged in He produce between metallic and dielectric planar surfaces, also show structure similar to a low-pressure glow discharge (Fig. 1.11). In both cases, a luminous zone is observed in the vicinity of instantaneous cathode.

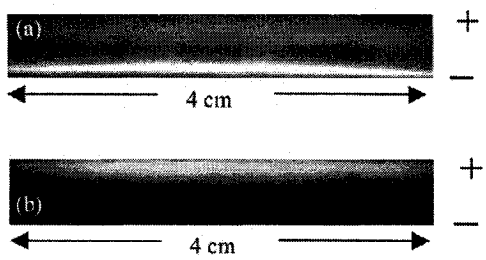

Figure 1.9 10 ns images of the gap during APGD in He (a) and N_2 (b) at the instant of maximum current through the discharge [33].

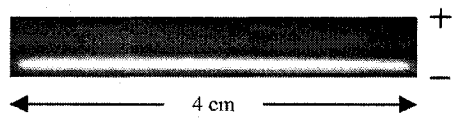

Figure 1.10 1 μs exposure image of APGD in He/NH_3 mixture [61].

However, during the positive half-cycle the thickness of the luminous layer (negative glow) is about 350 μm compared with only 50 μm in the negative half-cycle. In addition, the emission intensity from this layer is higher in the latter case, the direct result of charge accumulation on

the dielectric surface and of differences in the secondary electron emission coefficients, higher for the metallic surface than for dielectric one [62].

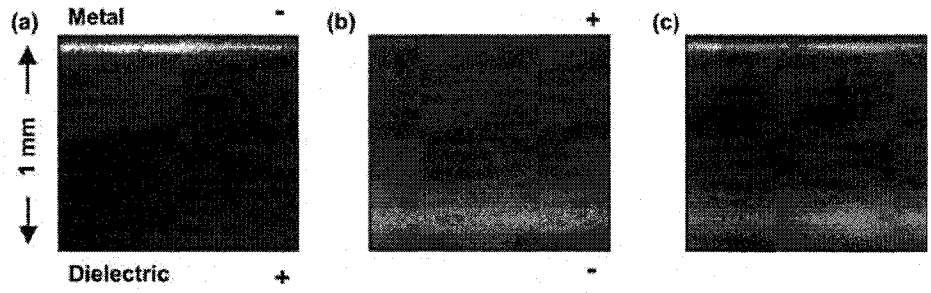

Figure 1.11 1 μs exposure images of positive and negative half-cycles of APGD in He between metal-dielectric planar surfaces [62].

However, in the case of N_2 APGD, the recorded images show quite a different spatial distribution of the light emission in the gap: short time exposure images (10 ns) taken between two planar electrodes separated by a 1 mm wide gap and both coated with ceramic (Al_2O_3), show emission only from the anode vicinity (Fig 1.9 (b)). From this image and from the discharge simulation, Massines *et al* concluded that N_2 APGD is a Townsend discharge [33].

One of the most complete analyses of APGD in a parallel electrode geometry and in different gases (air, N_2, He, Ne, Ar. Kr,) was reported by Radu *et al* [21], using images of the discharges recorded through a grounded, transparent electrode. The influence of gap width (He, Ne, Ar, Kr), and frequency of applied voltage (Ar, Kr) on the radial emission distributions from the discharges were described, including so-called "columnar structures" also reported by others [63]. The short time exposure images (10 ns) also recorded though the lower transparent electrode at different phases of the discharge peak showed previously unknown differences in luminosities among the various regions.

1.5 The influence of discharge parameters on the APGD in He and N_2

The most important discharge parameters that strongly influence the plasma characteristics are:

- Amplitude and frequency of the applied a.c. voltage;
- Dielectric (composition, thickness, permittivity, coefficient of secondary electron emission);
- Gap length;
- Gas composition (purity);

1.5.1 Voltage, V_{pp} and frequency, f

Radu *et al* reported a very extensive analysis of the influence of applied voltage frequency, f, and amplitude, V_{pp}, on discharges in helium at atmospheric pressure in a plane-plane electrode configuration [22, 31]. In a short planar gap (0.5 mm) at low voltage and low frequency, f = 2 kHz, they obtained an APGD in pure He characterized by the usual single discharge pulses per half-cycle. When V_{pp} was increased and f kept constant, or when f was decreased while maintaining constant V_{pp}, the photomultiplier (PM) and current signals showed several discharges pulses per half-cycle. The number of peaks was determined by the applied voltage, or by the lower limit of f required to maintain the discharge (Fig. 1.12). These so-called "pseudo-glow" discharges were composed of multiple discharge pulses per half-cycle, each peak corresponding to a uniform discharge that covered the entire electrode surfaces. The term "pseudo-glow" was coined by Bartnikas, first to observe this regime [17-19]. The amplitudes of PM and current signals are seen to decrease systematically with successive discharge in each half cycle while their respective widths, separation and rise times exhibit an increase in Fig. 1.12.

Using a one-dimensional fluid model, Golubovskii *et al* found that in a Townsend discharge the number of breakdowns per half-cycle increases with rising of V_{pp}, and that the duration between successive peaks becomes smaller [52]. The decrease in the separation times between the successive pulses infers a more rapid decrease in their breakdown voltages than is the case in Fig.1.12, where the pulse separation times are found to increase.

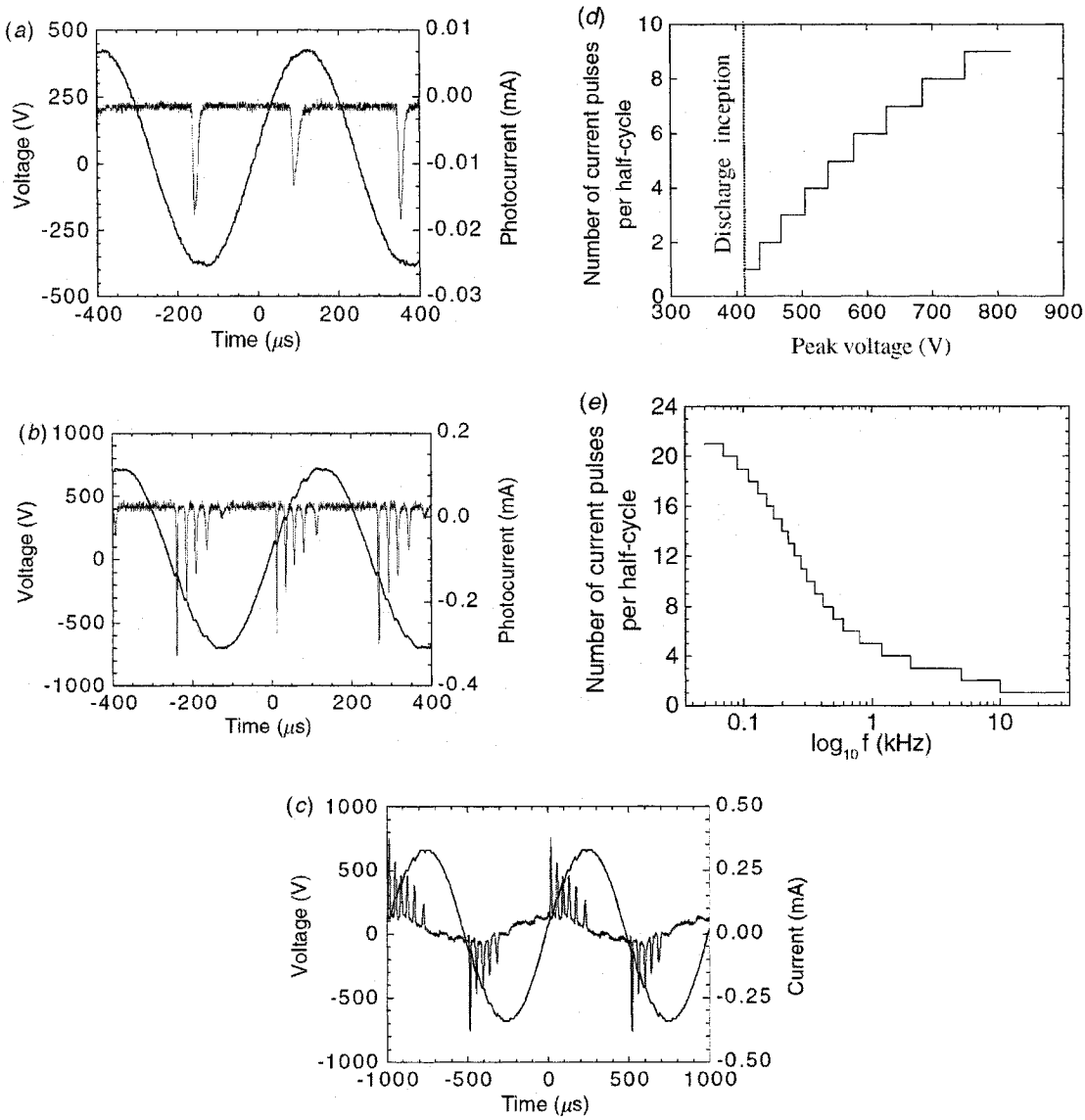

Figure 1.12 Pseudoglow regime from an APGD in He as a function of the frequency, f, and amplitude, V, of the applied voltage (a) f = 2 kHz, V = 420 V, (b) f = 2 kHz, V = 650 V, (c) f = 1 kHz, V = 650 V; the number of pulses as a function of V (d) and f (e) [22, 31].

1.5.2 Dielectric and gap width

The electrical circuit equivalent of the discharge cell before breakdown can be represented by two capacitors in series, one determined by the dielectric, the other by the gas gap between the electrode surfaces (Fig. 1.13). Then, a displacement current depends on the value of the two capacitors and the time derivative of applied voltage. When the electrical field in the gap is high enough to initiate a breakdown, a resistive current flows through the gap, its density being limited by the dielectric. The dielectric inhibits the transition to an arc-type discharge [16, 64]. An augmentation of dielectric thickness reduces the current density in the discharge by increasing the resistance and decreasing its associated capacitance, inversely proportional to the dielectric's impedance [65].

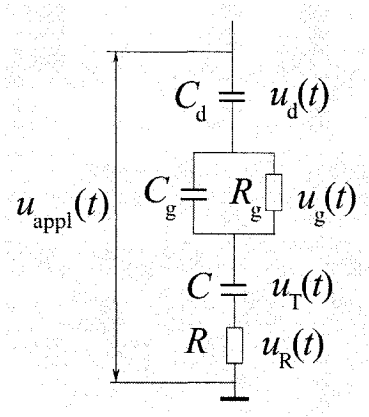

Figure 1.13 The equivalent electrical circuit for a discharge system [132].

The gap width and the dielectric thickness are therefore very important parameters that determine the type of uniform discharge, that is, glow or Townsend. For a given dielectric, the Paschen curve displays a minimum voltage necessary for breakdown of the gas, given a specific gap length (Fig. 1.14). When the gap is longer, the voltage must be raised and the discharge operates in the glow mode; if the gap is shorter, the voltage must also be increased, and the discharge operates in the Townsend mode. In order to obtain a Townsend-to-glow transition in a short gap, the dielectric thickness must be reduced, that is, its capacitance must be increased [52]. The type of discharge can also be influenced by the nature of the dielectric, for instance if it

is an electret[5]: using a special experimental configuration and an electret (polyethylene terephthalate, i.e. PET or 'Mylar') as the dielectric, Okazaki and Golubovskii reported a glow discharge in N_2 at power frequency, f = 50 Hz, [24, 66].

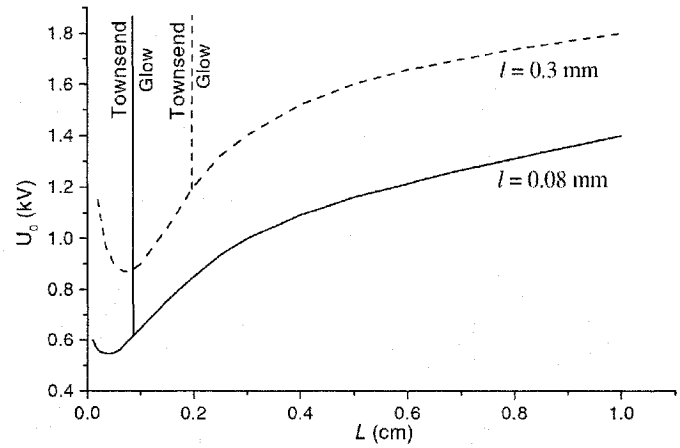

Figure 1.14 The dependence of the applied voltage necessary to produce a breakdown as a function of gap length, L, and thickness of dielectric, l, as discharge parameters (l = 0.3 mm and l = 0.08 mm) [52].

The values of the dielectric and gap-associated capacitances also affect the power dissipated in the discharge, increasing the latter when the dielectric-to-gap capacitance ratio decreases. [67].

Mangolini [65] studied the influence of the dielectric thickness on the APGD structure using high-speed ICCD imaging: The 20 ns images of He APGD in a planar electrode configuration with dielectrics of different thicknesses are shown in Fig. 1.15. For a dielectric of 1 mm thickness, the discharge displays a cathode layer, Faraday dark space and positive column. By gradually increasing the dielectric thickness, the images show a reduction of emission intensity from the positive column, and its total disappearance for 4 mm thickness, at which point the authors state that the discharge operates in a Townsend-like mode [65].

[5] A material with a quasi-permanent electrical polarisation in the absence of an external electric field.

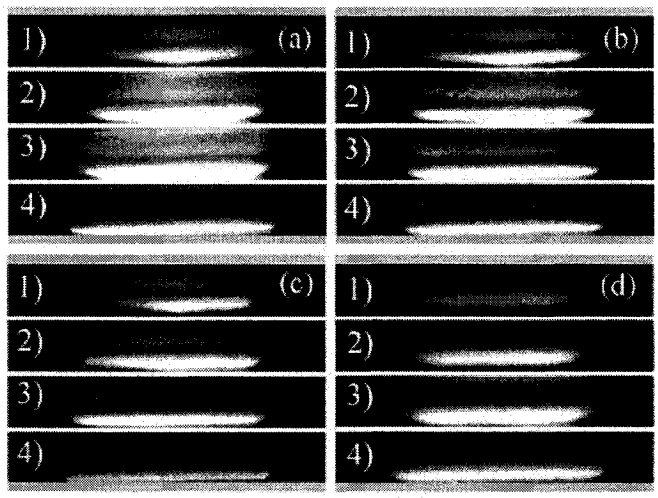

Figure 1.15 The influence of dielectric thickness on APGD in He: (a) 1mm, (b) 1.5 mm, (c) 2.5 mm and (d) 4 mm. The images have been recorded with a 20 ns exposure time and at different discharge times; frame #3 corresponds to the maximum value of the discharge current [65].

1.5.3 Impurities

The presence of impurities in He significantly influences the discharge characteristics: Radu et al [32] showed that controlled introduction of different kinds of impurities (Ar, N_2, H_2, O_2) could affect the number of discharge current peaks per half-cycle. For instance, in a pseudoglow discharge operated at 6 kHz in pure He with two peaks per half-cycles; their number increased up to five by introducing up to 0.5 vol% Ar or N_2, or 0.35 vol% H_2 (Fig. 1.16). If the impurity concentrations were increased beyond these values, the discharges became filamentary ("spark-like"). On the other hand, Massines *et al* [68] reported uniform discharge behaviour in He containing up to 1.6% N_2, probably on account of very different parameters of their experiment. However, each type of impurity has a different effect on the discharge; for instance, by introducing up to 0.2 vol% of O_2, an electronegative gas, into He APGD, the number of current peaks per half-cycle remained unchanged, following which "spark-like" behaviour occurred. In

the case of N_2 APGD, the glow-to-filamentary discharge transition occurs in excess of 500 ppm of O_2 or 2500 ppm of H_2 [27].

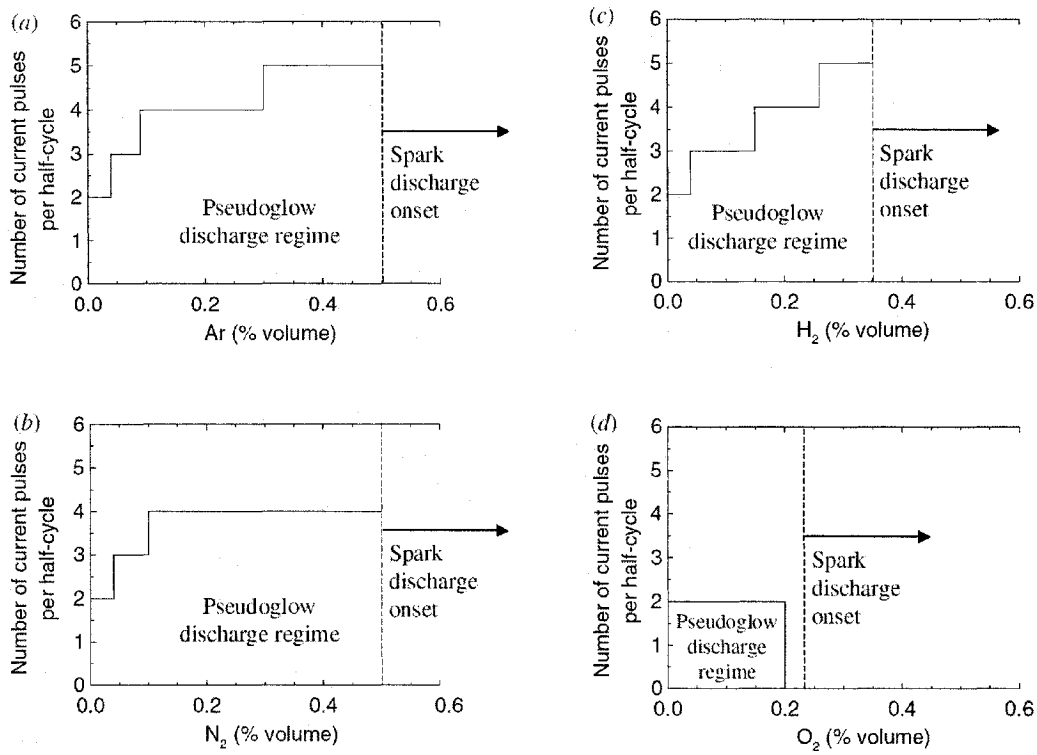

Figure 1.16 Pseudoglow regime as a function of impurity concentrations in He APGD; (a) argon, (b) nitrogen, (c) hydrogen, and (d) oxygen [22, 31].

Molecular impurities have a strong influence on the power dissipated in noble gas discharges. In pure He, the electron energy is used to ionize and excite the He atoms, but if molecular impurities such as N_2 are present in the discharge, a fraction of the electrons' energy can excite internal degrees of freedom (vibrational, rotational quantum states) of the molecules. As a result, with increasing N_2 concentration, the fraction of electrons available to ionize the neutral species decreases, and with it the current density in the gap and the power dissipated in the discharge.

1.5.4 Secondary electron emission

In the process of obtaining and maintaining a glow discharge at atmospheric pressure, the phenomenon of secondary electron emission[6] (SEE) is known to play an important role [33, 69, 70]. These electrons are the result of collisions between the discharge species (neutrals, metastables and ions) and the electrode surfaces (dielectric or metallic). The interaction between radiation originating from the discharge and the electrode surfaces can also release electrons (photoelectrons). The coefficient of secondary electron emission[7], usually symbolized by γ, strongly depends on electrode surface, the nature of incident particles and their energy (both potential and kinetic energy). For instance, γ due to interaction between metastables and a metallic cathode can be in the range $0.1 \div 1$ in the case of glow discharges [71]. The determination of γ for a dielectric surface is more difficult because of charging effects; when the dielectric surface is uncharged, γ can be theoretically estimated to have a maximum value of 0.5 [72] by using the Hugstrum theory [37]. On the other hand, the effect on γ of charge accumulation on the dielectric surface is not well known.

In a detailed review of plasma displays, Boeuf [73] presented SEE data resulting from the interaction of (Ne/Xe) APGD species and different dielectric materials; SEE also appears to be very sensitive to the nature of the surfaces such as crystal orientation, amorphous-to-polycrystalline content, etc, and it attains a constant value only after the surface has been exposed to the plasma for a sufficiently long time (named "burning time")(Fig. 1.17) [74].

Another problem linked to dielectric surface is the following: During the discharge, electrode surfaces (dielectric or metallic) are bombarded by electrically charged particles, electrons and

---

[6] SEE is defined as the process of interaction between a flux of incident particles and a material surface, which determine the emission of electrons from that surface. The incident particles can be atoms or molecules in fundamental or excited states, ions, as well as photons emitted by the plasma, and the surface is usually a metal or a dielectric.

[7] In the physics of electrical discharges in gases, the secondary electron emission from a surface is characterized by Townsend's second ionization coefficient, γ, that represents the number of electrons emitted from the given surface per incident particle, other conditions (e.g. particle energy) being specified.

ions. After a lengthy (~ minutes) exposure, a dielectric surface can become positively charged (Fig. 1.18) for sufficiently long durations (some hundreds of seconds) to be measured outside of the discharge [28, 29]. In other words, the dielectric behaves like an electret. Ionic bombardment appears to have a much greater impact on the dielectric than electron bombardment, due to the greater ionic mass.

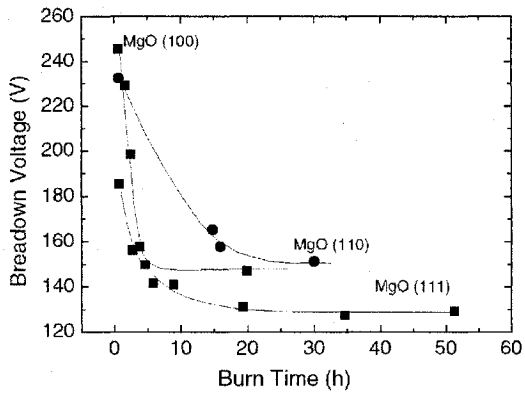

Figure 1.17 The evolution of breakdown voltage and, indirectly, of the secondary electron emission coefficient from a MgO dielectric substrate, as a function of the burning time, i.e. the duration of exposure of the dielectric substrate to plasma [74].

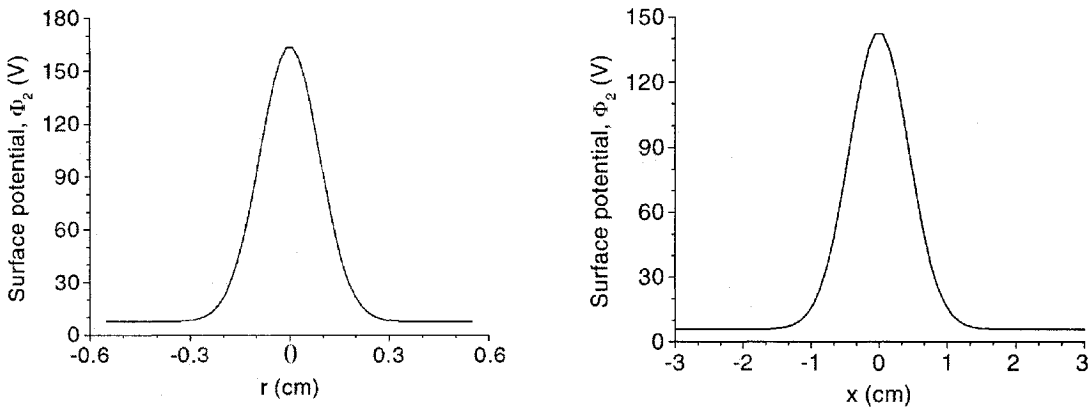

(a) (b)

Figure 1.18 The electrostatic potential measured on the dielectric surface after exposure to He APGD in a needle-plane (a), and cylinder-plane electrode configuration (b), respectively [28, 29].

1.6 Methods of APGD diagnostics

Diagnostic methods used by various authors include electrical and optical measurements, such as discontinuities in the ac waveforms across the discharging gas and the resulting electrical current pulse shapes [17-22, 28-33], and Q-V measurements or Lissajous figures [24], high speed imaging [21, 22, 25, 28, 29-33] and emission spectroscopy [25, 33, 38, 65, 75, 76], including temporal and spatial resolution [65, 75, 76].

Lissajous figures represent the observation of charge-voltage characteristics of a discharge [77], but the method cannot be applied over time [78]. These figures can have different forms ("ideal" parallelogram, ellipse) depending upon the discharge parameters (Fig. 1.19) [16], and from them it is possible to determine the power dissipated in the discharge [79], the breakdown voltage and the total charge transferred [80]. The latter can also be measured experimentally by introducing a series capacitance in the discharge circuit, between the lower electrode and ground, the voltage across this capacitor being proportional to the charge transferred [81]. For more information, see Appendix A.

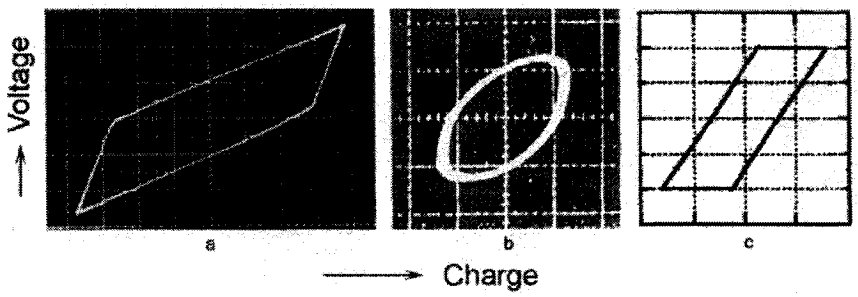

Figure 1.19 Examples of Lissajous figures obtained in different DBD (a) O_2, (b) CO_2 and (c) plasma display (Ne/Xe mixture) [16].

In order to discern APGD from a filamentary DBD, various combinations of the above-enumerated methods can be used. For instance, Hudon *et al* [82] combined synchronous diagnostics of the discharge by electrical and optical means, both capable of detecting short pulses, while Okazaki *et al* [24] used Lissajous figures.

1.7 Optical emission spectroscopy

1.7.1 General considerations

The study of plasma physics and chemistry necessitates detailed knowledge of the plasma parameters that can be obtained by using appropriate diagnostic techniques. Non-invasive, non-perturbing methods are obviously preferred, for example optical emission spectroscopy (OES). Since light emission is a natural property of the plasma state, it is a non-invasive source of information that can be used to evaluate some of the plasma's parameters such as atom, molecule and ion densities in ground and excited states, as well as gas-, rotational and vibrational temperatures. Spatial and temporal mapping of different radiative species present in discharge can also be accomplished.

The concept of temperature is, strictly speaking, only valid in a system that is in local thermodynamic equilibrium (a Maxwell-Boltzmann situation), not the case in a DBD or APGD. In this case different effective temperatures exist, i.e. gas (also named translational or kinetic), rotational, or vibrational temperature.

The estimation of gas temperature, T, from a plasma is very important because many applications such as material processing, surface modification, and elimination of hazardous gases, strongly depend on this characteristic [83, 84], since the rate coefficients of chemical reactions usually have an exponential (Arrhenius-law) dependence of T. The gas temperature in a plasma can be determined using different spectroscopy-based methods, for example diode-laser absorption spectroscopy (DLAS) [85-88], laser-induced fluorescence (LIF) [89], or OES [38, 62]. In the DLAS case, T is precisely and directly determined from Doppler broadening of an absorbed line [90]. Doppler broadening is a well-known and widely-used method of T determination in plasma but, for instance at 3000 K, Doppler broadening of hydrogen atom emissions is only 0.018 nm, so that spectrometers with very high resolution must be used. Application of the DLAS technique in a DBD at atmospheric pressure is very difficult because of the relatively high gas pressure (which results in pressure-induced line broadening) and low gas temperature (near-ambient temperature) [90]. The most frequently used method of temperature measurement in APGDs is based on OES, where the rotational temperature, T_{rot}, is

evaluated from the rotational emission spectrum of a diatomic molecule, usually by using the Boltzmann plot method (when this is applicable), or using a theoretical simulation of a rotational emission spectrum [91-94]; T_{rot} is then assumed to be equal to the gas temperature, T [95-101]. T_{rot} (or T) in a given discharge can be evaluated from a particular molecular species [91-94, 97], or from two or more molecular species present in the same discharge [98].

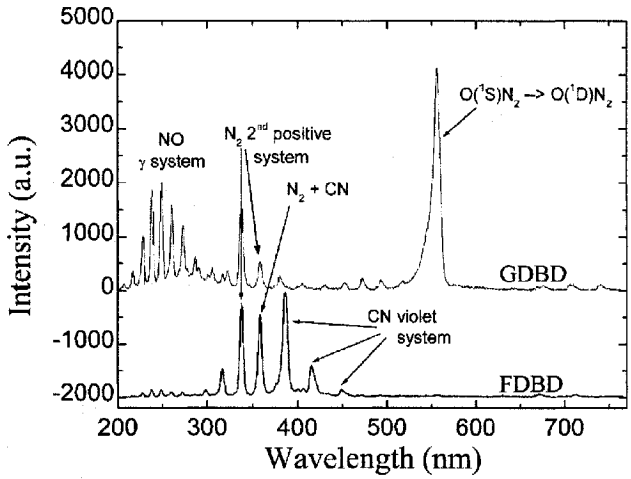

Figure 1.20 The optical emission spectra from a uniform (GDBD) and filamentary (FDBD) discharges in N_2.The spectra are normalized to the N_2 (337 nm) band [33].

The evaluation of T_{rot} from rotational emission spectra has been reported in the literature for a large variety of species such as OH [91, 94, 102, 103], N_2^+ [104-108], C_2 [101, 109-111], CH [112-114], CN [102, 111, 114-116], NO [103], O_2 [104, 105], NH [114], SiH [117], N_2 [106, 118-120], H_2 [121, 122]. In atmospheric pressure DBDs obtained in many gases, the presence of the Second Positive System (SPS) of N_2 and the First Negative System (FNS) of N_2^+ can be easily identified through their well-known emission spectra [38]. However the very complex N_2 SPS rotational spectrum cannot be resolved with moderate-resolution spectrometers, and T is usually determined by contour fitting [123]. However, the rotational structure of N_2^+ FNS can be fully resolved even with a spectrograph of average performance, and T_{rot} can be easily determined. However, the emission from N_2^+ is not present in all atmospheric pressure discharges, for instance in N_2 DBD (or its emission intensity is insufficient for temperature evaluation) (Fig. 1.20). In this case, the emission spectrum from another diatomic molecule must be used to measure T.

The optical emission spectrum of APGD in high purity helium contains the emission lines from SPS $N_2(C^3\Pi_u - B^3\Pi_g)$ and FNS $N_2^+(B^2\Sigma_u^+ - X^2\Sigma_g^+)$ bands, the bandhead of the P branch from the $N_2^+(B^2\Sigma_u^+, v'=0 \rightarrow X^2\Sigma_g^+, v''=0)$ transition at 391.44 nm being the most intense emission line (Fig. 1.21) [33]. Hence, in APGD in helium, the gas temperature can, in principle, be easily determined from N_2^+ FNS emissions.

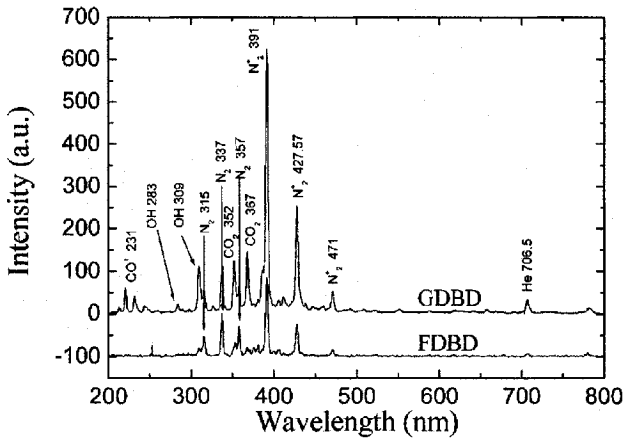

Figure 1.21 The optical emission spectra from uniform (GDBD) and filamentary (FDBD) discharges in He [33].

1.7.2 The evaluation of gas temperature from rotational temperature

From both theoretical [34, 35, 36, 124] and experimental [22, 25, 33, 125] results, it is known that energy transfer by Penning collisions is an extremely efficient process in He discharges, on account of the very high excitation energies and cross sections of He (2^3S) metastables (~ 20 eV) and He_2 dimers (~ 16 eV). Therefore, even trace amounts of impurities are readily ionized, for example nitrogen, as evidenced by FNS N_2^+ emission lines [25, 33]. OES measurements have shown that rotational band intensity distributions can obey Boltzmann statistics, even though this should strictly apply only in the case of thermal excitation. The reason for this behaviour is that molecular excitation by "hot" electron impact in discharges gives rise to little change in angular

momentum, on account of the very small mass of the electron. Therefore, the upper (electronically excited, photon-emitting) excited states possess essentially the same Boltzmann-like energy distribution as ground-state molecules. Owing to the high collision frequency at atmospheric pressure, this distribution is near thermal equilibrium at a certain effective temperature. However, other processes may also populate the excited states, particularly by Penning collisions in He; this may conceivably cause deviation from a normal thermal distribution [126], so that the measured rotational temperature might not be the same as the translational temperature of neutral molecules.

Emission spectra of DBDs in "pure" He or in He/N_2 mixtures are characterized by a very strong signal from the N_2^+ FNS (0,0) rotational-vibrational band

$$N_2^+\left(B^2\Sigma_u^+\right) \rightarrow N_2^+\left(X^2\Sigma_g^+\right) + h\nu \tag{1.1}$$

The principal excitation mechanisms of $N_2^+(B^2\Sigma_u^+)$ states are by direct electron impact from the ground state of the neutral N_2 molecules $N_2(X^1\Sigma_g^+)$ [127, 128]

$$N_2(X) + e^- \rightarrow N_2^+(B) + 2e^- \tag{1.2}$$

by charge transfer [129]

$$He_2^+ + N_2 \rightarrow N_2^+(B) + 2He \tag{1.3}$$

and by Penning ionization [125, 129]

$$He^* + N_2 \rightarrow N_2^+(B) + He + e \tag{1.4}$$

If we assume that (1.1) is applicable for purposes of thermometry, relaxation of the rotational population of the $N_2^+(B^2\Sigma_u^+)$ state to thermal equilibrium must be faster than the radiative lifetime of this excited state, which is approximately equal to 66 ns [38]. However, this state is rapidly quenched by molecular nitrogen

$$N_2^+\left(B^2\Sigma_u^+\right) + N_2 \rightarrow products + N_2 \tag{1.5}$$

For instance, when the partial pressures of N_2 in atmospheric pressure He are 2 kPa or 6.5 kPa, the effective lifetimes drop from 66 to 5 ns and 2 ns, respectively [38]. Thus, with increasing the nitrogen partial pressure, the rotational population may not fully relax, and the rotational and translational temperatures may differ. Now, each of the mechanisms (1.2) to (1.4) contributes to the overall $N_2^+(B^2\Sigma_u^+)$ population, but (1.2) and (1.4) dominate, especially (1.2), due to Penning

ionisation [125]. Notwithstanding that quenching by N_2 tends to impede relaxation of the rotational population (see above) and the fact that Penning ionisation raises the temperature by only a few tens of K above that of the $N_2^+(X^1\Sigma_g^+)$ ground state, led Bibinov *et al* [38] to conclude that the rotational temperatures determined from $N_2^+(B^2\Sigma_u^+)$ spectra are identical to the gas temperature.

1.7.3 Boltzmann plot

The intensity of a spectral line in emission is defined as the energy emitted by the source per second. If there are $N_{J'}$ atoms in the initial state and if $A_{J'J''}$ is the fraction of atoms in the initial state undergoing the transition to J'' per second, then

$$I_{J'J''} = N_{J'} hc\nu_{J'J''} A_{J'J''} \tag{1.6}$$

where $hc\nu_{J'J''}$ is the energy of each light quantum of wavenumber $\nu_{J'J''}$ emitted, J' and J'' the quantum numbers of the upper and lower states, respectively. $A_{J'J''}$ is the spontaneous transition frequency for emission that is related to the matrix element of transition, as follows

$$A_{J'J''} = \frac{64\pi^4 \nu_{J'J''}^3}{3h} \left| R^{J'J''} \right|^2 \tag{1.7}$$

where $R^{J'J''}$ is the matrix element of the electrical dipole moment of the J', J'' transition.

The number of molecules $N_{J'}$ in the rotational states at temperature T is given by

$$N_{J'} = \frac{N}{Q_r}(2J'+1)\exp\left(-\frac{F(J')hc}{kT}\right) \tag{1.8}$$

where $F(J')$ is the rotational term (units cm^{-1}), N is the total number of molecules, $2J'+1$ is the statistical weight in the Born–Oppenheimer approximation, and Q_r is the rotational state sum (or partition function), defined by

$$Q_r = \sum_{J=0}^{\infty}(2J+1)\exp\left(-\frac{F(J)hc}{kT}\right). \tag{1.9}$$

One obtains in this way the intensity of the lines of rotational or rotational-vibrational bands in emission originating from the same electronic and vibrational level, $I_{J'J''}$, given by

$$I_{J'J''} = \frac{64\pi^4 \nu_{J'J''}^4 cN}{3Q_r}\left(\sum\left|R^{n_i m_k}\right|^2\right)\exp\left(-\frac{F(J')hc}{kT}\right) = \\ = \frac{2C\nu_{J'J''}^4}{Q_r} S_{J'} \exp\left(-\frac{F(J')hc}{kT}\right) \tag{1.10}$$

when the excited level populations are assumed in thermal equilibrium. Here, J' and J" are the rotational quantum numbers of the upper and lower rotational states; $S_{J'}$ is the line strength corresponding to J', and C is a constant that depends on the change and magnitude of the dipole moment, and on the total number of molecules in the initial vibrational level. For a given T_{rot}, Q_r remains constant for all lines in a same vibrational band; $F(J')$ is the rotational term (in units of cm^{-1}); h, c and k are Planck's constant, the velocity of light, and Boltzmann's constant, respectively. From relation (1.10) one then immediately obtains

$$\ln\left(\frac{I_{J'J''}}{\nu_{J'J''}^4 S_{J'}}\right) = A - \frac{F(J')hc}{kT} \tag{1.11}$$

where $A = ln(2C/Q_r)$ is a constant for all lines in the same band (v', v'') for a given value of T_{rot}, v' and v'' being the vibrational quantum numbers of the upper and lower vibrational states. Therefore, a plot of $ln(I_{J'J''}/\nu^4_{J'J''} S_{J'})$ versus $F(J')$ is a straight line of slope hc/kT_{rot} [126]; knowing the line intensities and the rotational constants, one can readily determine T_{rot}.

The FNS of N_2^+ represent a $^2\Sigma$ - $^2\Sigma$ transition, with both upper and lower $^2\Sigma$ states always belonging strictly to Hund's case (b), so that the selection rule $\Delta K = \pm 1$ holds, $\Delta K = 0$ being forbidden. The total angular momentum apart from spin, K, (a quantum number) can have integral values Λ, $\Lambda+1$, $\Lambda+2$, ..., where Λ are the angular momenta. In the case of a Σ state, $\Lambda = 0$. The possible values of J, which is the resultant of angular momentum K and spin S, for a given K, are $K+S$, $K+S-1$, ..., $|K-S|$. Thus, in general (except when $K < S$), each level with a given K consists of $2S+1$ components (the multiplicity). For the $^2\Sigma$ state, the spin is $S = ½$, and each level is divided into two sublevels with $J = K + ½$ and $J = K - ½$. In other words, there is a doublet P and a doublet R branch [126]. In view of the limited resolution of our spectrometer, the observed rotational spectrum has only one apparent R branch, the doublet not being resolved, and the lines are now numbered by K instead of J.

If K' is the quantum number of the upper state and K'' is that of the lower state, and if we denote $K'' \equiv K$, then $K' = K + 1$ for the R-branch ($\Delta K = 1$). In our case, the line strength for R-branch (which is a superposition of two R-branches) is $S_{K'} = K + 1$, and the rotational term value, $F(K')$ is given by

$$F(K') = B_{v'}(K+1)(K+2) - D_{v'}(K+1)^2(K+2)^2 \qquad (1.12)$$

where $B_{v'}$ and $D_{v'}$ are the rotational constants for the upper state. Their values were taken from references [126] and [130], while the wavelengths for the FNS of $N_2^+(B^2\Sigma_u^+ - X^2\Sigma_g^+)$ (0-0) band were obtained from ref. [131].

Chapter 2 EXPERIMENTAL METHODOLOGY

In this chapter, we present the experimental set-up, the instrumentation for diagnostics and the methods used for analysis of data. The experimental set-up has been developed to investigate the influence of different parameters on the physics and chemistry of DBDs: in this work discharges in different gases with various electrode geometries have been studied mainly by high-speed imaging and by optical emission spectroscopy (OES).

2.1 Experimental set-up

The experimental arrangement shown in Fig. 2.1 is made up of four main parts: the discharge reactor vessel, the high-voltage power supply, the gas supply and control, and the diagnostic systems. The first three parts are the same in all experiments, but the last is different in imaging experiments and those involving spectroscopy. A detailed description of the set-up used for ultra-high speed imaging (UHSI) is presented elsewhere [21, 22, 28-32], and will therefore not be repeated here: the main emphasis of our program has been on OES.

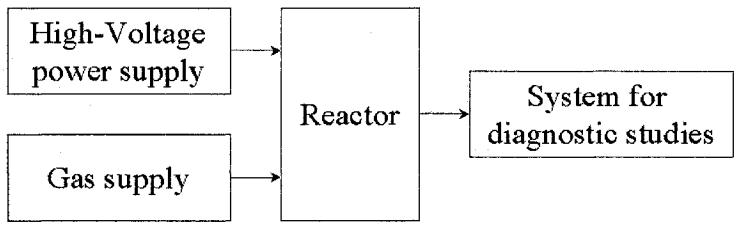

Figure 2.1 Block diagram of the present experimental set-up.

2.1.1 The reactor

The chamber is a hermetic Pyrex glass cylinder with an exterior diameter of 30 cm, and a 2 mm thick wall, closed at both ends with two metallic end plates (Fig. 2.2). The reactor is connected to a vacuum pump that permits one to achieve a preliminary vacuum of 10^{-2} Torr before introducing the flow of working gas. A gas supply system feeds the reactor and maintains a constant flow rate of the feed gas during the entire duration of the experiment, at a pressure slightly above one bar, so as minimize the danger of contamination from the atmosphere.

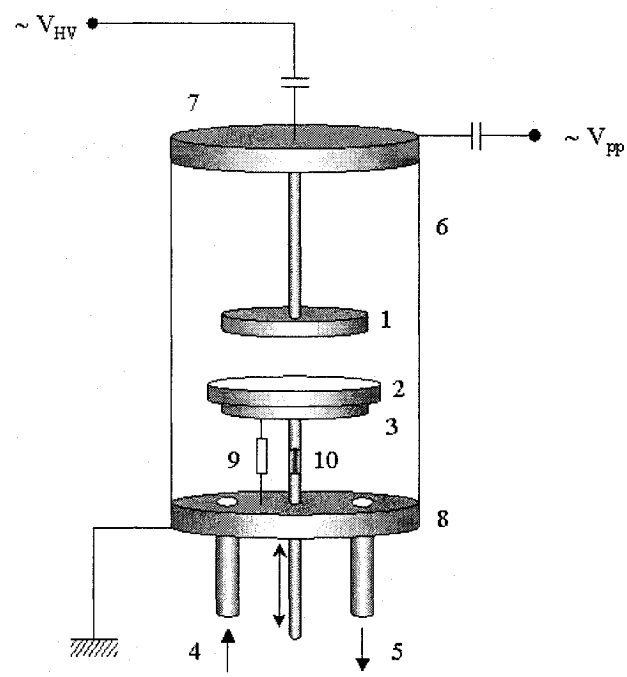

Figure 2.2 Schematic representation of the reactor used for the present DBD research: (1) upper electrode, (2) dielectric, (3) lower electrode, (4) input gas tube, (5) output gas tube, (6) reactor chamber, (7) upper metallic end plate, (8) lower metallic end plate, (9) resistor (50 Ω), (10) insulating support.

One electrode is fixed to the upper metal plate and connected to the high voltage (HV) power supply. The other (bottom) electrode is mounted via a micrometer screw to the lower plate and is

connected to ground through a 50-Ω resistor. The lower plate is grounded and isolated from the bottom electrode. The gap spacing, d, between the upper HV electrode and the low-potential electrode is precisely adjusted with the micrometer screw; four different types of HV electrodes have been used, namely

(A) a stainless steel needle electrode with a tip of precisely machined radius, 20 μm in same cases, and 40 μm in others (Ogura Jewel Co. Japan);

(B) a cylindrical steel electrode with a radius of 3.15 mm and a length of 26.3 mm;

(C) a spherical steel electrode with a radius of 6 mm; and

(D) a planar polished stainless steel electrode with rounded edges, 2.54 cm in diameter.

The low-potential, planar, dielectric-covered electrode at the bottom consisted of either

(E) a 1 mm thick glass plate with a transparent (indium tin oxide, ITO) conductive coating on its bottom surface, to permit observation and imaging of the entire discharge zone;

(F) a 1.6 mm thick Al_2O_3 ceramic plate (25 x 25 mm), metallized on the bottom;

(G) a 1.6 mm thick ZrO_2 ceramic plate (44 x 30 mm), metallized on the bottom; or

(H) a 1.5 mm thick MgO ceramic plate (44 x 33 mm), metallized on the bottom;

The dielectrics that comprise the bottom, low-potential electrode play a very important role in determining the discharge behaviour. Not only does the material itself influence the discharge through γ, its coefficient of secondary electron emission, but the thickness and the relative permittivity also have a very important impact in determining the associated capacitance. The four types of dielectric materials enumerated above had been used in an earlier study of DBD using ultra-high speed imaging (UHSI). However, in all of the OES studies only two dielectrics, namely Al_2O_3 (for axial discharge studies) and glass (in the case of radial analyses of discharges, being a transparent electrode material) have been utilised.

To repeat, four types of HV electrodes have been used, giving rise to four different electrode geometries (Fig. 2.3), namely

a. needle-plane;

b. cylinder-plane;

c. plane-plane; and

d. sphere-plane.

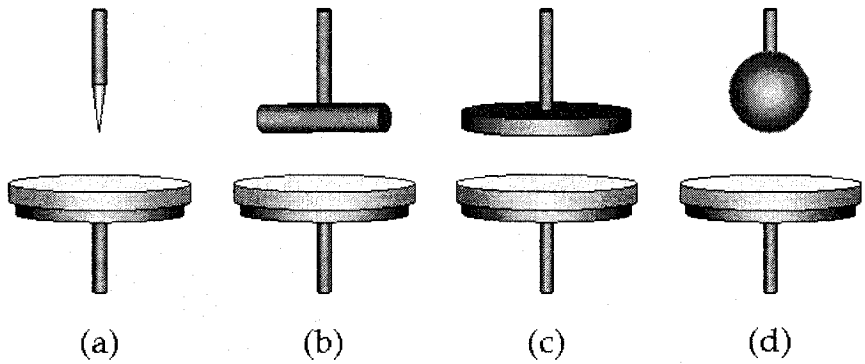

Figure 2.3 The four electrode geometry configuration investigated: (a) needle-plane, (b) cylinder-plane, (c) plane-plane and (d) sphere-plane.

In case (c), a quasi-uniform electric field is obtained in the inter-electrode gap, while in the other three cases divergent fields are produced.

In most of the experiments, carried out with pure helium, pure nitrogen, or He/N_2 mixtures, a total gas flow rate of 5.7 standard litres per minute (slm) was used. However, in some cases (with He/N_2 mixtures) the flow rate of helium was reduced to 2.0 slm, in order to increase the upper limit of N_2 partial pressure in the He (dictated by the characteristics of the available electronic mass flow controllers, MFC).

2.1.2 High-Voltage (HV) power supply

The high voltage (HV) power supply is made up of a variable frequency generator, a power amplifier, an impedance matching unit and a HV transformer (Fig. 2.4). The generator produces a sinusoidal signal with a frequency in the range 1 Hz to 30 kHz. The signal from the generator is introduced into one of the two inputs of a RAX 1450 audio high power stereo amplifier. In

"bridge" mode, this amplifier can produce high output power (up to 1400 W) for an input signal between 20 Hz and 20 kHz, so that the output signal is more then 40 times higher after amplification. The impedance matching unit is a high power, low-value resistor (a few ohms), which permits one to optimize signal transfer between the amplifier and the HV transformer; the latter steps up the electric signal to HV as high as 25 kV, but this depends on the value of current drawn by the electrical circuit. When the current increases, the maximum voltage value decreases; in other words, the power supply cannot provide voltage with constant amplitude over a wide range of current values, and this can influence the discharge stability [67]. Finally, the HV signal is applied to the upper electrode through a low-value, corona-free vacuum capacitor, part of a capacitive voltage divider (see section 2.2.3).

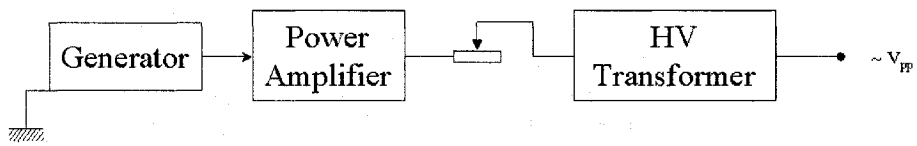

Figure 2.4 High-Voltage (HV) power supply.

2.1.3 The gas supply system

The system for gas supply permits mixing two gases in different ratios and control of the mass-flow rate of feed gas into the reactor (Fig. 2.5). We use two mass-flow controllers and a four-channel meter/controller that provides a readout of gas flow (MKS 274[8]), a potentiometer for correction, and input/output signals for remote readout, recording, and controlling purposes. The flow rate set-point can be adjusted either through controls on the front panel or remotely through an analog interface on the rear panel. The mass-flow controllers have ranges between 0 and 10

[8] The MKS 247 Power Supply and Readout is suitable for signals from any electronic flow transducer.

slm[9], and between 0 and 100 standard cubic centimetres per minute (sccm), deliberately chosen for the needs of this project; for example, a typical mixture may comprise 6 slm of He and 60 sccm of N_2 (helium "doped" with 1% of nitrogen).

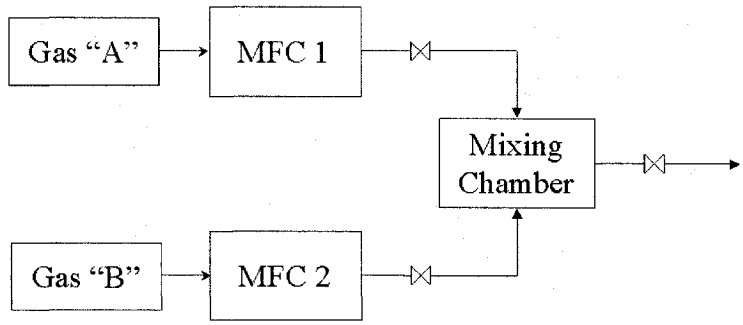

Figure 2.5 Feed gas supply system.

2.1.4 System for diagnostics of discharges

The discharge behaviour has been examined using the following optical and electrical diagnostic methods [21, 22, 28-32]:

1. ultra-high speed imaging (UHSI), with an intensified charge coupled device (ICCD) digital camera (Roper Scientific PI-MAX 512RB) positioned either parallel or normal to the axis of the discharge;
2. total light emission from the gap, detected using a photomultiplier (PM, Philips 3460);

[9] The mass-flow controllers are calibrated for nitrogen by the manufacturer. When another gas is used, a correction factor must be applied. For instance, in the case of helium (He), the correction factor is 1.43. For more details see Appendix B.

3. the photomultiplier signal, the (applied) ac voltage across the discharge cell and current pulses from the discharges were all synchronously displayed using a digital storage oscilloscope (Tektronix TDS 220, 100 MHz); and finally,
4. OES, using a 0.5 m focal length spectrograph (Acton Research SpectraPro 500i), coupled to the ICCD array detector mentioned above.

The ac HV signal across the test cell (gap in series with the dielectric barrier) was monitored by means of either a resistive divider (Tektronix P6015A) or a capacitive voltage divider comprising two corona-free vacuum capacitors. The discharge current pulse magnitude and shape was evaluated from the ac voltage across the 50-Ω resistor between the lower electrode and ground. The photomultiplier was mounted in a grounded metal enclosure to reduce external noise and ambient light, and it was maintained at 600 V with a suitable HV supply. All of the above-mentioned signals where displayed on the digital oscilloscope (any two at the same time) and recorded on a PC.

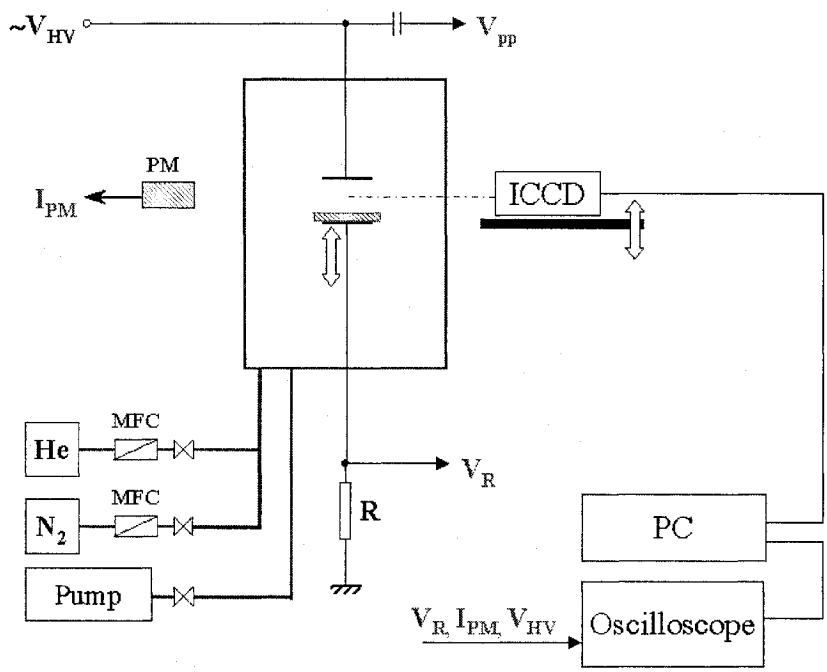

Figure 2.6 Experimental set-up for plasma-diagnostic experiments using the ICCD detection system (see text)

The ICCD (Intensified Charge-Coupled Device) is a very powerful optoelectronic array that can detect and record spatio-temporal light signals with exposure times as short as 2.5 ns. In fact, the exposure time is that in which the charge accumulating on the CCD is compiled into the report data. The Intensifier amplifies the incident light and applies it to the CCD. Basically, the intensifier controls what the chip records during the time of exposure. This intensifier/controller therefore allows one to record very rapid, periodic events with very short exposure times even if the emitted light is faint, for example, in the case of APGD. This is possible by accumulating a large number of signals, provided that they are precisely periodic in time. The ICCD camera has been used to record the polychromatic images of the discharge in the UHSI experiments; coupled to the spectrograph, the ICCD detector has been used to record the emission spectra of discharges over a wavelength range between 350 and 900 nm in the OES mode. The remarkable characteristics of this device have therefore permitted us to record very short time exposure image sequences or emission spectra of discharge events under a wide variety of experimental conditions.

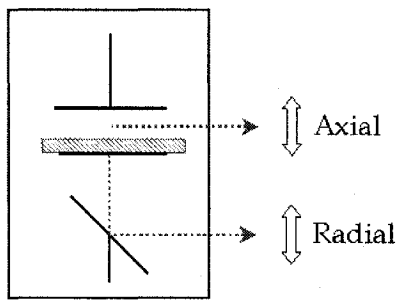

Figure 2.7 Experimental arrangements used to study axial and radial discharge characteristics.

The ICCD detector was fixed on a mobile support that permits one to adjust its position with respect to any part of the discharge (Fig. 2.6). The axial and radial distributions of light emitted by the discharges were both studied (Fig. 2.7); in the latter case, radial distribution measurements, light passing through the transparent lower electrode was reflected by a mirror towards the ICCD detector. The ICCD array was cooled by a Peltier element, allowing substantial reduction in the noise level. A gate signal from the power supply is used to synchronize the short-duration exposure image or spectrum with the ICCD detector. All signals,

including the PI-MAX images, could thereby be precisely synchronized and processed on the computer.

The spectrograph has a resolution of 0.05 nm at 435.8 nm when used in conjunction with an 1800 grooves/mm grating and a 10-μm entrance slit: Light from the discharge was directed to the entrance slit via the mobile optical system, similar to one described by Kozlov *et al.* [134], which was capable of providing a (one-dimensional) spatial resolution as fine as 100 μm. However, to achieve an acceptable signal-to-noise ratio, most of the experiments were carried out with a coarser resolution of 250 μm. As depicted schematically in Fig. 2.8, the discharge image was transposed onto the slit by a convex lens placed at twice its focal length from the slit and from the discharge centre. The slit, together with another convex lens and the optical fibre, were fixed on an optical track that could be displaced vertically with a micrometer-adjusted positioning system. Most spectra were recorded using an entrance slit width of 10 μm, an 1800 grooves/mm grating blazed at 500 nm, and using a cumulative exposure time of about 200 ms.

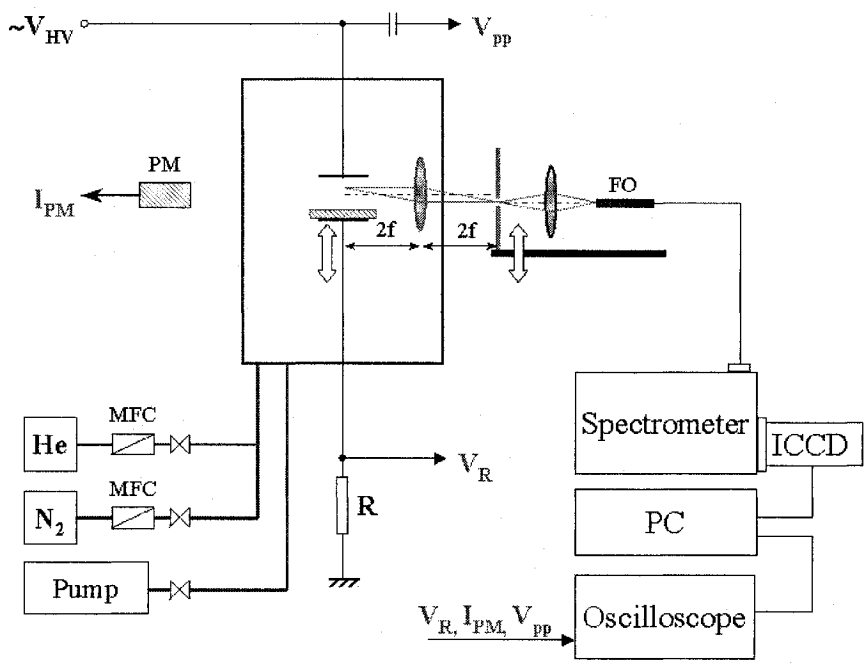

Figure 2.8 The experimental set-up used for spatio-temporally resolved optical emission spectroscopy (OES).

2.2 Diagnostic methodology

The spatial and temporal evolutions of DBDs for different electrode geometries and feed gas compositions were investigated using UHSI and OES. In addition, other parameters for each case, namely the applied peak-to-peak voltage, V_{pp}, across the discharge cell, the current across the gap, I, and the total light emission intensity as measured by the PM current, I_{PM}, were also recorded. As will be shown in later chapters, all those data, taken together, characterize particular experiments, but the first two diagnostic techniques (UHSI and OES) are both the most complex and the richest in terms of information-content.

2.2.1 Ultra-high speed imaging (UHSI)

The digital camera provides suites of digital images of a particular discharge event, taken at precise time intervals (for example, 0.1 μs). Each image is an array of points (pixels) representing different light intensities (Fig. 2.9). The space-time evolutions of propagating discharges were obtained from the recorded digital "film" sequences, as follows:

- first, the precise positions of the two electrodes on the digital images were determined (see, for example, Fig. 2.10);
- this permitted the digital images to be calibrated in millimetres (correlation between the pixels and true spatial dimensions);
- in each image, the radial and axial positions of points (pixels) representing the same light intensity (iso-points), I_0, were determined;
- each image was recorded at a constant time interval with respect to the previous one for example at 100 ns separation; this permitted spatio-temporally resolved reconstruction of image sequences.

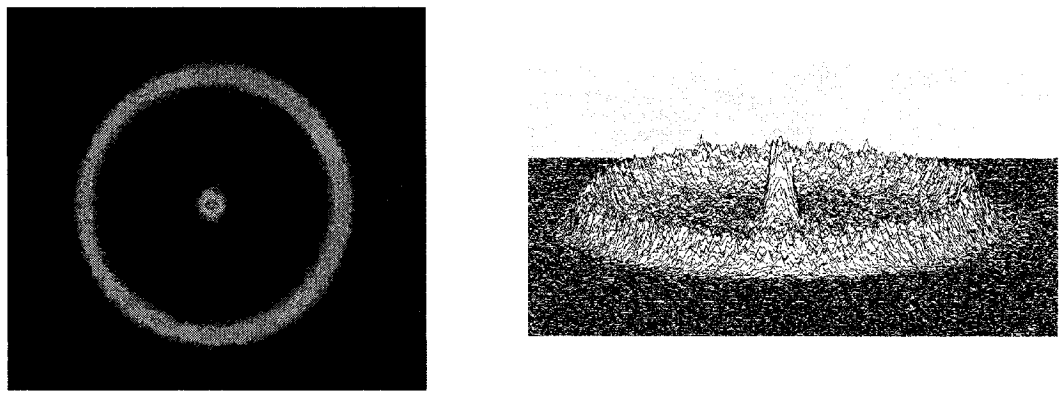

Figure 2.9 An example of data from a UHSI experiment (a) a 10 ns exposure time image (composed of 1000 "identical" accumulations) from He APGD in a 3 mm needle-plane gap, recorded through the lower transparent electrode; (b) the same data, but in a 3D representation, where the "z" coordinate represents relative light intensity (see Chapter 3).

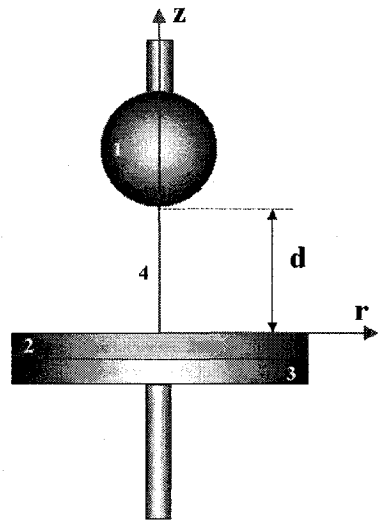

Figure 2.10 Geometrical characteristics of a sphere-plane discharge configuration: (1) upper electrode (sphere in this case), (2) dielectric, (3) lower electrode and (4) gas gap. The same symbols are used when the HV electrode is replaced by a needle, cylinder, or plane.

Finally, we obtained the complete spatial (radial and axial) and temporal evolutions of discharges under particular, selected sets of conditions.

Another method to obtain spatio-temporal information is to make a cross section (axial or radial) through a particular position (for instance, in the axial case, at the position r = 0 mm). The 3D intensity-time reconstructions of such sections also yield the spatial and temporal discharge evolution.

The total light intensity from each image was integrated and represented as a function of time; this could be compared with the corresponding PM output signal, and in all the cases studied perfect correlation could be noted between these two signals. This allowed us to precisely determine the position in time of each image with respect to the phase of the applied sinusoidal voltage.

2.2.2 Optical emission spectroscopy (OES)

The spectrally-resolved emission intensities of discharges were recorded as functions of spatial and/or temporal dependencies. For example, to determine the rotational temperature, T_{rot}, the emission of the N_2^+(0-0) R branch manifold near 391.4nm was studied in detail, as described in Chapter 3; this, of course, involved resolving each contributing line features with the spectrograph and measuring their relative intensities.

As mentioned above, the methodologies and results obtained under a wide variety of discharge conditions using both UHSI (section 2.2.1) and OES (section 2.2.2) will be described in the following chapters.

Chapter 3 RESULTS AND DISCUSSION

The main objective of this research was to study the behaviour of He APGD as functions of different discharge parameters (gas composition, gap length, electrode geometry configurations, types of dielectrics, etc.) by ultra-high speed imagery (UHSI) and optical emission spectroscopy (OES). However, other gases and gas mixtures have also been investigated, such as Ne and N_2. The results obtained from the UHSI and OES experiments are presented in the first and the second parts of each subsection respectively, different subsections corresponding to the different electrode geometries.

3.1 Spatio-temporal studies of (needle-plane) discharges

Most of the experiments were carried out on He, because He constitutes a convenient inert gas medium, it represents an appropriate test gas free of any chemical reactions and decomposition problems [34, 35, 36], and also because it is relatively less expensive compared with other noble gases, such as Ne, Kr or Xe. We studied He APGD in the needle-plane electrode geometry, for example, using needles with different tip radii, different dielectrics and applied voltages across the discharge cell. Two examples of long-time exposure images recorded from APGDs produced in a 3.0 mm gap and using two different dielectrics (Al_2O_3 and MgO) between the metallic electrodes are shown in Fig. 3.1. Around the tip of the (high-voltage) upper electrode, the light emission presents a higher intensity as a result of the electrode geometry, for reasons explained later. A second region of high emission intensity, but much lower than at the needle, is observed in the vicinity of the dielectric surface. The discharge activity in mid-gap appears to be very much reduced in comparison with the former two. We note that each image is the result of light accumulation from many discharge events, in both positive and negative half cycles, during the total ~ 0.5s exposure time. By using our ultra-high-speed camera it is possible to record almost "instantaneous" pictures (a few ns) from each phase of the discharge, and these can help to better

understand the complex events that take place in APGDs. For instance, in Figure 3.2 we show a "film[10]" of an APGD in the 3.0 mm needle-plane gap during the positive half-cycle of applied

(a) (b)

Figure 3.1 Example of "long-duration" exposure images from He APGD produced in a 3.0 mm needle-plane electrode geometry gap for the case of (a) MgO and (b) Al_2O_3 dielectric surfaces.

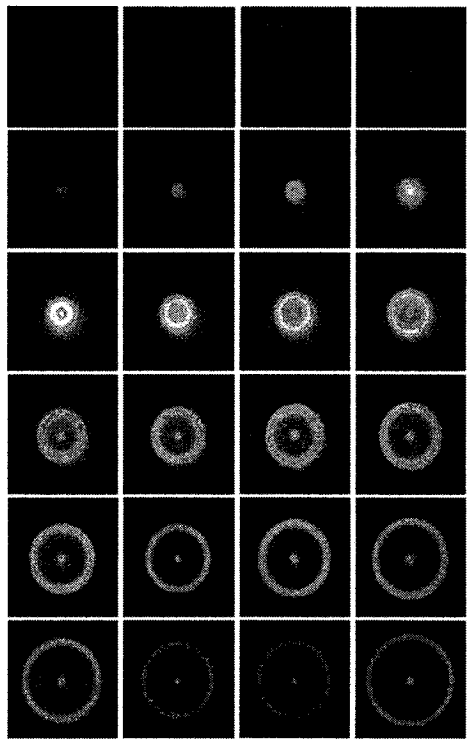

Figure 3.2 An example of a "film" of a He APGD in a 3.0 mm needle-plane gap, recorded through the lower transparent (glass/ITO) electrode during the positive half-cycle of the applied voltage. Each image corresponded to an exposure time of 10 ns, the time between two consecutive images having been 0.5 μs. The radius of the needle electrode was 40 μm.

[10] In this figure we show only images of the discharge at 0.5 μs intervals. However, usually (like in this film) we recorded images at 0.1 μs intervals, during the entire discharge duration.

voltage, recorded through the transparent (glass/indium tin oxide (ITO)) lower electrode with a 10 ns exposure time for each image[11]. Figure 3.2 reflects only the radial aspect of APGD, while a "film" sequence of side-views of the discharge is presented in Fig. 3.3; together with Fig. 3.2, it helps to construct a virtual three-dimensional "film" of this particular discharge. Elsewhere [28, 32] Radu *et al.* also presented sequences of 2.5 ns UHSI exposures illustrating the discharge propagation from the needle tip to the dielectric surface, a total duration of about 2 μs.

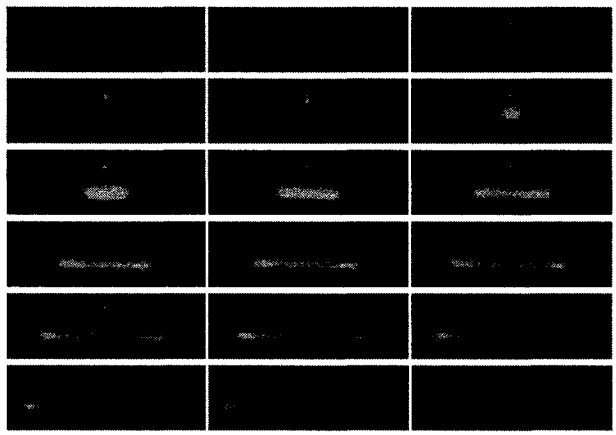

Figure 3.3 An example of a transverse-view "film" representing a He APGD event in a 3.0 mm needle-plane gap during the positive half-cycle. Each image had a 10 ns exposure time, and the time between two consecutive images was 1.0 μs.

Taking a cross section through each image of the discharge "film", a representation in time of the emission intensity along this cross section (or another one) can be obtained, with time on "x", space on "y" and the emission intensity on "z", x, y, z being the axial directions of a Cartesian reference. An example of I-t (total emission intensity, I, versus time, t) radial maps during the negative and positive half-periods, respectively, is shown in Fig. 3.4 (a) and (b). This representation corresponds to Fig. 3.2, where the discharge is observed through the glass electrode. I-t maps along the needle-plane axis are shown in Fig. 3.5 (a) and (b), but this time for a different dielectric, namely Al_2O_3. Luminous emission near the needle tip is seen to precede the propagation event, which takes place roughly between –2 and 0 μs on the indicated time scale (Fig. 3.5 (a)), by many μs and persists for at least 6 μs thereafter. Similarly, the luminous

[11] Each image is the result of 1000 accumulations of 10 ns each, so that it is in fact a 10 μs cumulative exposure time.

region at z ≈ 0.7 mm above the dielectric surface is also seen to persist for more than 6 μs. Referring to Fig. 3.5 (b) that corresponds to the negative polarity, we note that luminosity near z = 0 at t = 0 is weak and brief (< 2 μs), but that near the needle tip it persists for the entire duration of the photomultiplier (PM) pulse signal, roughly 35 μs. In this latter case the luminosity practically exists only around the upper (needle) electrode.

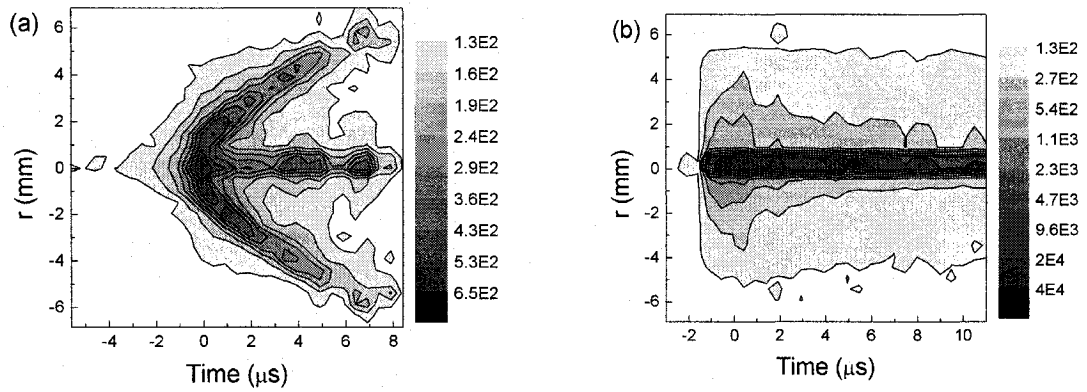

Figure 3.4 Radial spatio-temporal I-t maps recorded through the glass/ITO electrode, for He APGD in a 3.0 mm needle-plane gap: (a) positive half-cycle; (b) negative half-cycle; t = 0 corresponds to the maximum of the PM pulse signal (see Fig. 3.6 (a)).

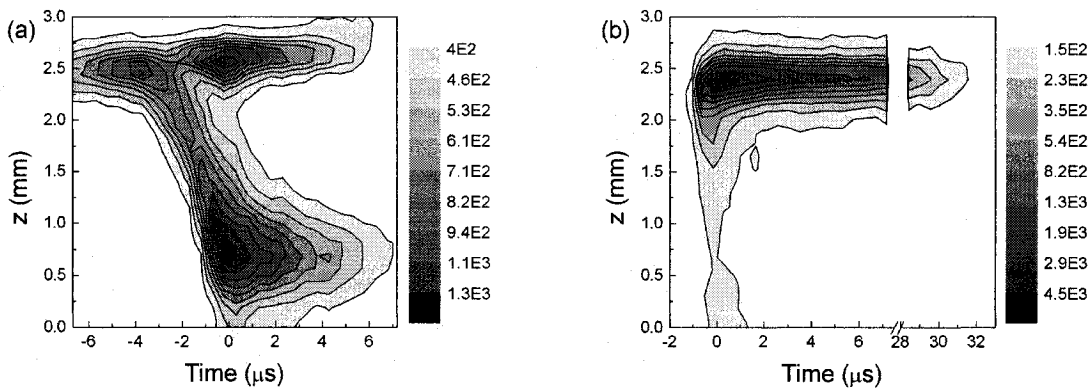

Figure 3.5 Spatio-temporal distributions of total light emission intensity, I, from APGD in "pure" He in a needle-plane gap of 2.5 mm: (a) positive half-cycle and (b) negative half-cycle of the ac voltage across the test cell. Dielectric (Al_2O_3) surface at z = 0; t = 0 corresponds to the maximum of the PM pulse signal (see Fig. 3.6 (a)).

Figure 3.6 (a) shows the corresponding PM and current signals of the discharge, for the case V_{pp} = 1.6 kV. The broad peak during the positive half-cycle was about ~ 15 μs in total duration, while the lower-intensity peak during the negative half-cycle was of much longer duration (~ 35 μs). In Figure 3.6 (b) we show a correlation between the photomultiplier signal and that obtained from the recorded "film" of the discharge using the ICCD camera: the latter represents the total

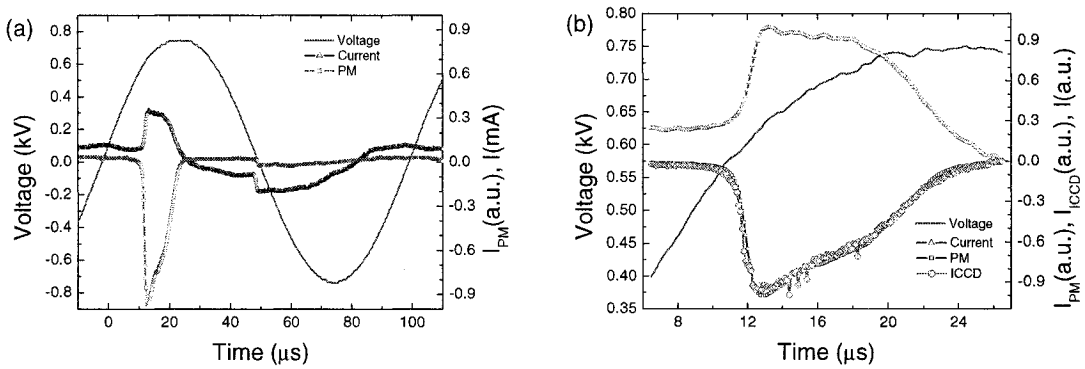

Figure 3.6 (a) The photomultiplier signal (I_{PM}), discharge current (I) and voltage across the test cell (V_{pp}) corresponding to APGD in "pure" He in the 3.0 mm needle-plane gap; (b) the same signals during the positive half-cycle, together with the representation of total light from images of the discharge "film" (I_{ICCD}) (1.5 kV, 10 kHz).

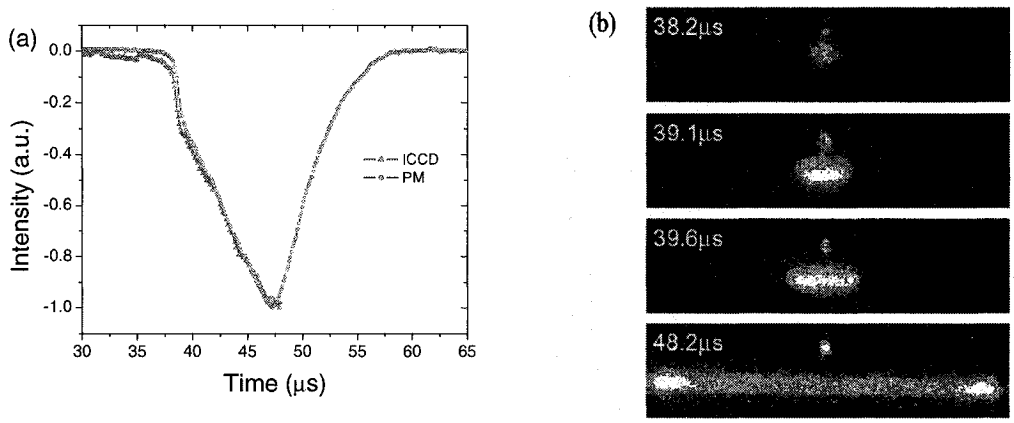

Figure 3.7 (a) The PM signal and that corresponding to the total light emission from ICCD images overlap. (b) The four images show the discharge at different times; we observe that the discharge contacts the dielectric surface at about 39 μs, when a point of inflexion is observed on the two signals in 3.7 (a).

emission intensity from each successive image as a function of time. Clearly, the two signals are almost identical after the normalization (Fig. 3.6 (b) and 3.7(b)). This representation can help us determine with higher precision the shape of discharge (its radial and axial spread) that corresponds to a given time position of the PM signal. For example, we observed that in most of the cases studied, the time corresponding to the maximum emission intensity during the positive half-cycle (positive voltage on the upper electrode) did not coincide with that when the discharge front first contacted the dielectric surface (see Fig. 3.7). A discontinuity can be noted in the shape of PM signal, when the discharge front reaches the dielectric surface and begins to propagate radially.

In Fig. 3.8 (a) and (b) we show the I-t maps along the needle-plane axis during positive half-periods from discharges, where (a) the upper electrode was a needle with 200 μm radius, and the dielectric was Al_2O_3; and (b) the upper electrode was a needle with 20 μm radius and the dielectric was MgO. These axial cross-sections correspond to the needle axis (r = 0) and therefore provide no information about radial propagation of the discharge. Using the same images from a discharge "film", corresponding to each axial position in the gap, a radial cross-section can be deduced, hence information about radial extent at any given z position. Since images (a) and (b) appear rather similar, we conclude that the needle radius and nature of the dielectric do not seem to qualitatively influence the main features of these discharge events.

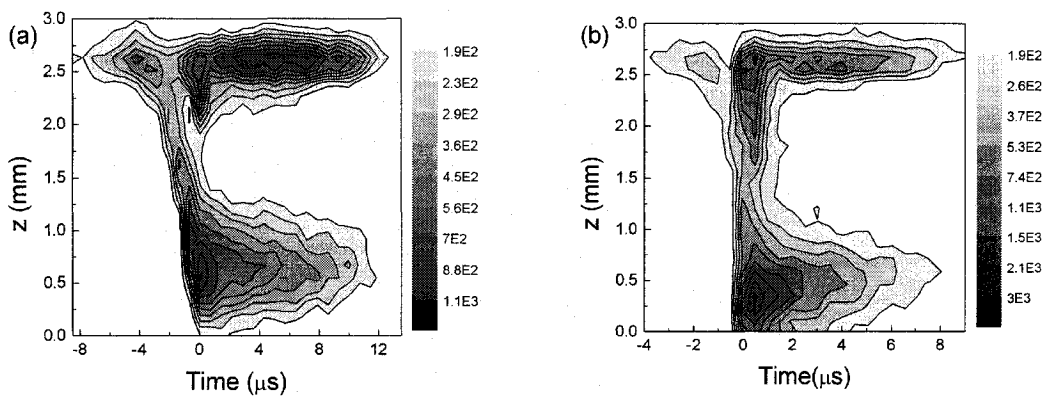

Figure 3.8 Spatio-temporal distributions of total light emission intensity, from APGD in "pure" He in a needle-plane gap of 3.0 mm: (a) 200 μm needle radius and Al_2O_3; and (b) 20 μm needle radius and MgO. Dielectric surface at z = 0.

3.2 Optical emission spectroscopy (OES): general remarks

The optical emission spectrum (Fig. 3.9) between 350 nm and 860 nm of an APGD in high purity helium is very similar to that reported by others [33]. This spectrum was obtained in a 3.0 mm needle-plane discharge, but it differed little from those obtained in cylinder-plane or plane-plane configurations. The only differences between these, or between two different axial positions in the same geometry, were the relative intensities of the various emission lines. The frequency and amplitude of the sinusoidal voltage across the test cell and the gap length were also found to influence these relative intensities. However, in all discharges emission lines from SPS $N_2(C^3\Pi_u - B^3\Pi_g)$ and FNS $N_2^+(B^2\Sigma_u^+ - X^2\Sigma_g^+)$ bands, triplet oxygen at 777 nm ($3^5P \rightarrow 3^5S$), and the $3^3S \rightarrow 2^3P$ transition at 706.5 nm from He I could be clearly identified.

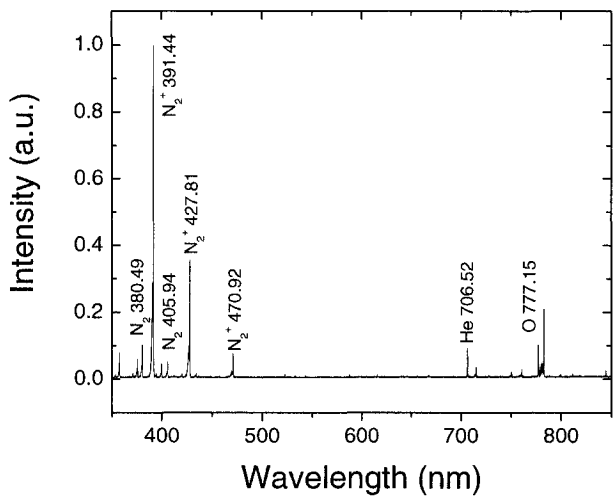

Figure 3.9 A typical emission spectrum from APGD in "pure" He.

The most intense emission was always the bandhead of the P branch from the $N_2^+(B^2\Sigma_u^+, v'=0 \rightarrow X^2\Sigma_g^+, v''=0)$ transition at 391.44 nm, while fainter helium lines were observed at 667.8 nm ($3^1D \rightarrow 2^1P$), 587.6 nm ($3^3D \rightarrow 2^3P$), or 388.8 nm ($3^3P \rightarrow 2^3S$). The latter is positioned between the R(K=19) and R(20) lines of the rotational emission spectrum from FNS of N_2^+ (0,0). Clearly, even in a flow of nominally very pure He, slightly above atmospheric pressure, N_2 impurity at the ppm level was sufficient to yield high enough spectral intensity for accurate T_{rot}

measurements (Fig. 3.10). The presence of such N_2 impurities in the discharge-cell were presumably due to some residual air, even after evacuation down to 10^{-2} Torr, to some possible N_2 impurities in the He feed gas, and to possible small leaks in the system and back streaming. Values of T_{rot} were determined from the R branch of $N_2^+(B^2\Sigma_u^+, v'=0 \rightarrow X^2\Sigma_g^+, v''=0)$ using the Boltzmann plot method (Section 1.7 and Fig. 3.11).

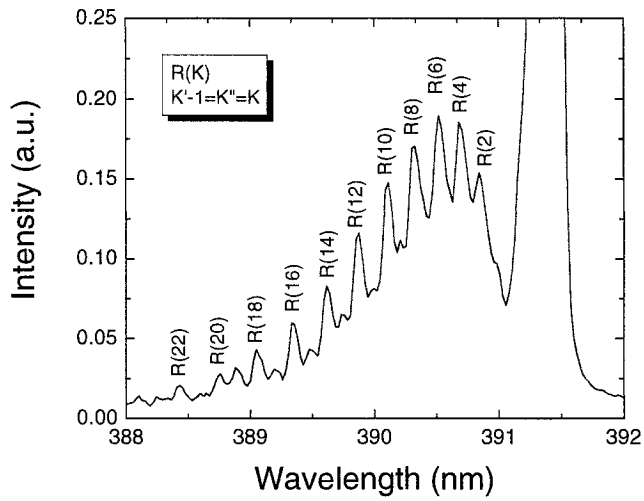

Figure 3.10 A typical $N_2^+(B^2\Sigma_u^+, v'=0 \rightarrow X^2\Sigma_g^+, v''=0)$ spectrum from APGD in "pure" He.

However, some precautions must be taken to minimize possible errors. Each line of the R branch, R(K), overlaps with a rotational line of the folded-back portion of the P branch, P(K+27) [119]. For example, P(29) and P(31) are superimposed on R(2) and R(4), respectively. As a result, at higher gas temperatures the P branch lines can contribute appreciably to the measured intensity of low-K R branch lines, resulting in a lower apparent value of T_{rot} [136]. Also, the bandhead of the (3,6) vibrational transition from SPS of N_2 at 389.4 nm can affect the measured intensity of R(16) (see Fig. 3.12). Considering these complications, values of T_{rot} were determined only on the basis of lines between R(6) and R(14), inclusive. Each value of T_{rot} was determined by plotting the average intensities obtained from 25 spectra. The standard deviation of R branch line intensities was usually between 2 and 5%; we found that a 5% value results in an uncertainty of less than 5% in T_{rot}.

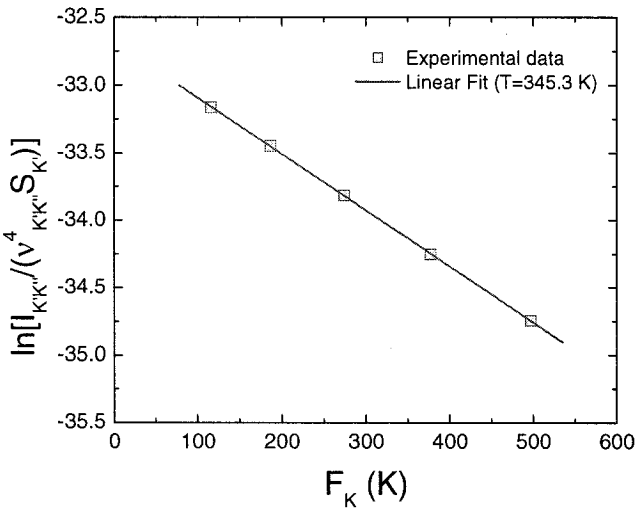

Figure 3.11 A typical Boltzmann plot of R(6)-R(14) line intensities from the R-branch of $N_2^+(B^2\Sigma_u^+, v'=0 \rightarrow X^2\Sigma_g^+, v''=0)$ versus the energy of the upper rotational levels.

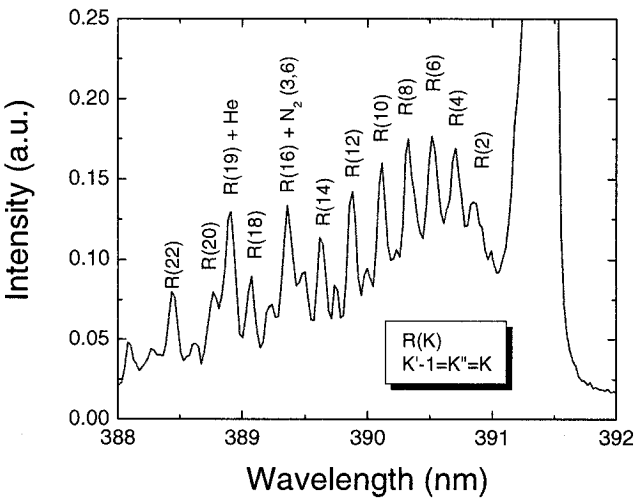

Figure 3.12 The $N_2^+(B^2\Sigma_u^+, v'=0) \rightarrow N_2^+(B^2\Sigma_u^+, v''=0)$ spectrum with overlapping contributions from the $3^3P \rightarrow 2^3S$ He line (388.9 nm) and the (3,6) vibrational transition from the SPS of N_2 (389.4 nm), taken in the vicinity of the needle electrode of APGD in "pure" He.

3.3 Spatial distribution of T_{rot}

3.3.1 Needle-plane geometry

Figure 3.13 portrays the axial distributions of measured values of T_{rot} and of relative emission intensity at 391.4 nm, I(391), in the 3.0 mm needle-plane gap with a 2.0 slm flow of pure He; z = 0 corresponds to the dielectric surface, z = 3.0 mm to the needle tip. T_{rot}, equal to about 360 K near z = 0, is seen to rise to about 450 K at z = 3.0, while I(391) appears to have opposite behaviour; intuitively, one would tend to associate a high value of T_{rot} with the intensity maximum just above the dielectric surface. A likely explanation can be found in Fig. 3.5 (a) and (b): The cumulative life of the plasma near the needle tip (about 50 μs, half of the voltage period, see Fig. 3.5 (b)) therefore presumably accounts for the significantly higher T_{rot} value observed near z = 3.0 mm (see Fig. 3.13). This is discussed in more detail later.

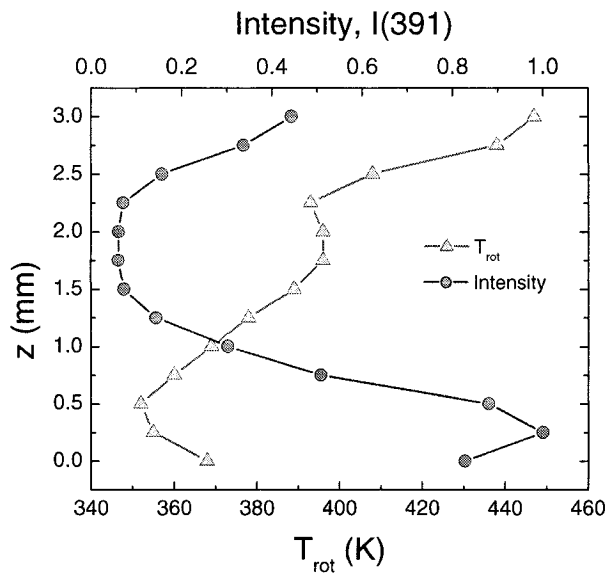

Figure 3.13 Typical axial distributions of T_{rot} and P-branch bandhead intensity, I(391), in "pure" He APGD in the 3.0 mm needle-plane gap (He flow = 2 slm, f = 10 kHz, V_{pp} = 2.9 kV). Dielectric surface at z = 0.

Figure 3.14 shows spatially and temporally-resolved intensity maps, similar to Fig. 3.5 (a), but these now correspond to three important OES wavelengths, 380.5 (N_2), 391.4 (N_2^+), and 706.5 nm (He I). While all of these maps clearly display similar main features as the global intensity, Fig. 3.5 (a), since they jointly comprise the latter, each of them possesses its own distinct characteristics, symptomatic of complex phenomena that are active within the discharge. More will be said about this, too, in the General Discussion (Chapter 4).

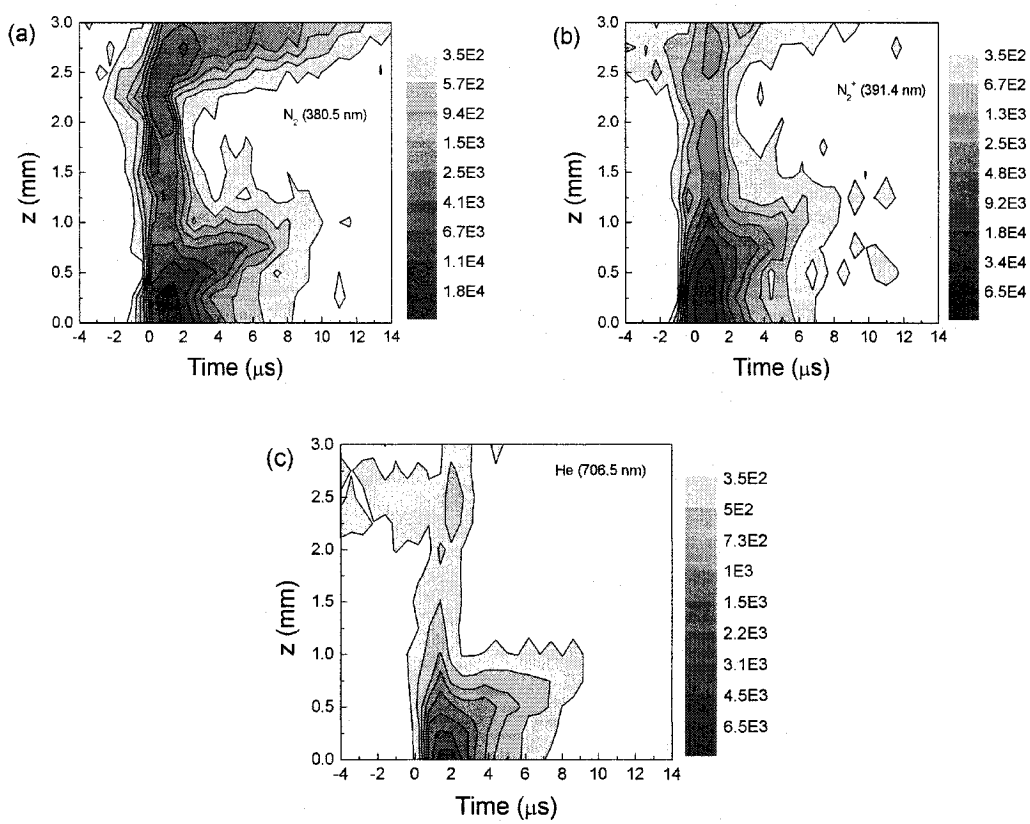

Figure 3.14 Spatio-temporal intensity distributions of spectral features at (a) 380.5 nm (N_2); (b) 391.4 nm (N_2^+); and (c) 706.5 nm (He I) during the positive half-cycle of APGD in "pure" He in a 3.0 mm needle-plane gap. Dielectric surface at z = 0.

Further illustration of radial spreading of the luminous zone near the dielectric surface (z = 0), already noted in Figs. 3.1 to 3.3, can be found in Figs. 3.4 (a) and 3.15. The symmetrical pattern of the former (upper and lower branches in Figs. 3.4 (a)) represents radial outward expansion of the annulus shown in Fig. 3.2 as observed through the transparent (glass/ITO) electrode, while the long-lived luminosity observed at r ≈ 0 of course corresponds to that near the needle tip (see

Figs. 3.1, 3.4 and 3.5). Figure 3.15 shows that the relative intensity of each spectral component of the overall luminosity, I, in Fig. 3.4 (a) decays at a comparable rate with increasing r. Each of these plots is seen to display a distinct oscillatory component, superimposed on the (parallel) linear intensity decays, but we do not assign much significance to this since Fig. 3.15 is the result of a single data acquisition, not multiple acquisitions.

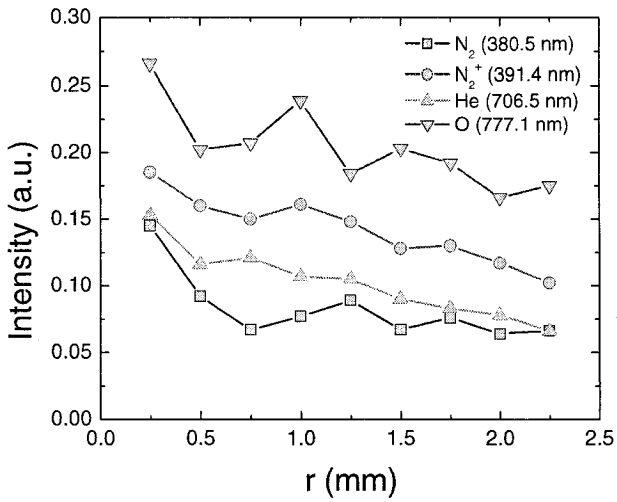

Figure 3.15 Radial intensity profiles of four different spectral features in the optical emission from APGD in "pure" He in a 3.0 mm needle-plane gap, measured through the transparent planar electrode. The position r = 0 corresponds to the needle axis, r > 0 to the radially-expanding luminous zone seen in Fig. 3.2 (He flow = 5.7 slm, f = 10 kHz, V_{pp} = 1.5kV).

The relatively low time-averaged value of T_{rot}, ~ 360 K (or ~ 90°C), reported near z = 0 in Fig. 3.13 can presumably be explained by the fact that the plasma here was quite short-lived (<10 μs, see Fig. 3.4 (a) and 3.5) and that the high heat capacity of the neighbouring solid surface favoured cooling of the gas. However, we also conducted time-resolved radial measurements of T_{rot}, shown in Fig. 3.16. As already mentioned in connection with Fig. 3.15, I(391) is seen to decay near-linearly with increasing r, but T_{rot} is found to rise sharply from its near-constant value, ~ 390 K for $0 \leq r \leq 2$ mm, to ~ 480 K near r = 3.5 mm. The reason for this surprising behaviour is not known at this moment, but possible explanations will be provided in Chapter 4.

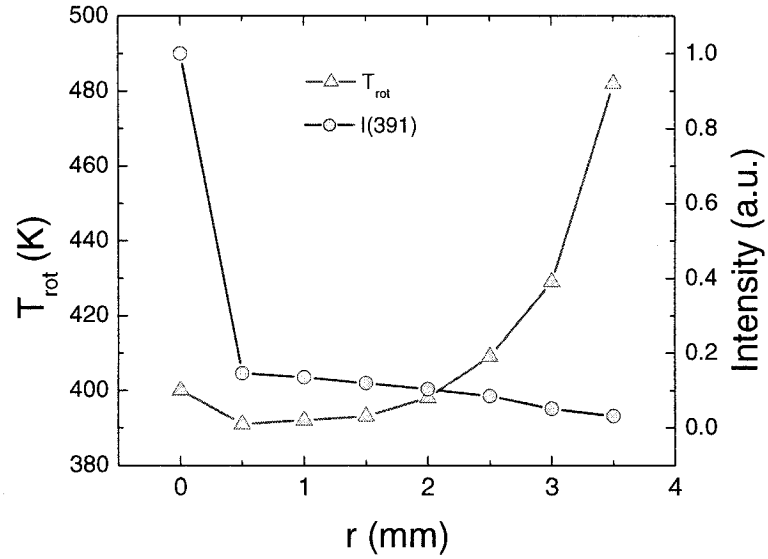

Figure 3.16 Radial distributions of T_{rot} and I(391) measured through the transparent planar electrode under the conditions described in the caption of Fig. 3.15.

3.3.2 Cylinder-plane geometry

Figure 3.17, like its earlier counterpart, Fig. 3.13, shows the axial distribution of T_{rot} and of I(391), this time in the 3.0 mm cylinder-plane gap with a 5.7 slm flow of pure He. Here again, z = 0 corresponded to the dielectric surface and z = 3.0 to the perimeter of the steel cylinder of 3.15 mm radius. This geometry, too, has been the object of earlier reports by Radu *et al* [29, 30] in which they presented UHSI of the time- and space-resolved discharge propagation, among other experimental and theoretical modeling data. We note that in this geometry the steady-state value of T_{rot} at the two electrode surfaces was close to 380 K (near 100°C) and about 330 K in mid-gap, while I(391) again displays a clear maximum in the vicinity of the dielectric surface, as observed by UHSI [29, 30]. Although the discharge current for the cylinder-plane case [29, 30] exceeded that of the needle-plane gap [28] by more than an order of magnitude due to the much larger electrode surface area, the optical intensity was found to be only slightly higher for the

former. In any event, intensity values are normalized in each case since absolute emission intensity comparisons do not contribute much to our physical understanding.

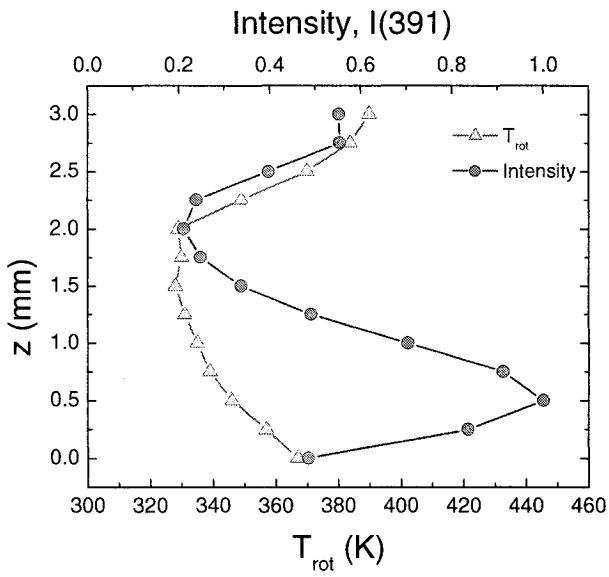

Figure 3.17 Typical distributions of T_{rot} and I(391) in "pure" He APGD in the 3.0 mm cylinder-plane gap (He flow = 5.7 slm, f = 10 kHz, V_{pp} = 2.0 kV). Dielectric surface at z = 0.

3.3.3 Plane-plane geometry

Figure 3.18 shows a typical PM trace corresponding to an APGD produced in a 3.0 mm plane-plane gap in "pure" He, for a 10 kHz sinusoidal applied voltage of $V_{pp} \approx 2$kV. The emission intensity was higher in the positive half-cycle, but the durations of both current pulses were equal, about 5 μs. The slight asymmetry between the two pulses presumably resulted from that of the electrodes, one metallic the other dielectric. Increasing V_{pp} resulted in a PM signal of higher amplitude and longer duration, that reflected higher discharge power; also, breakdown initiated at an earlier phase in both half-cycles, as a result of higher charge accumulation on the dielectric surface.

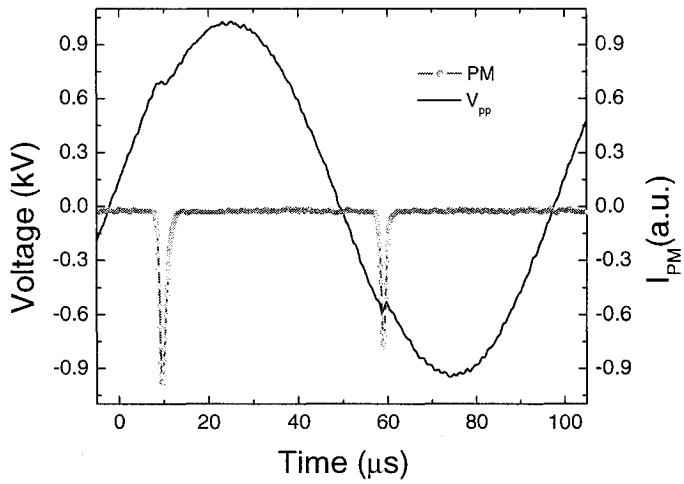

Figure 3.18 Photomultiplier (PM) and the applied voltage signals for an APGD in 5.7 slm of pure He, produced in a 3.0 mm planar gap.

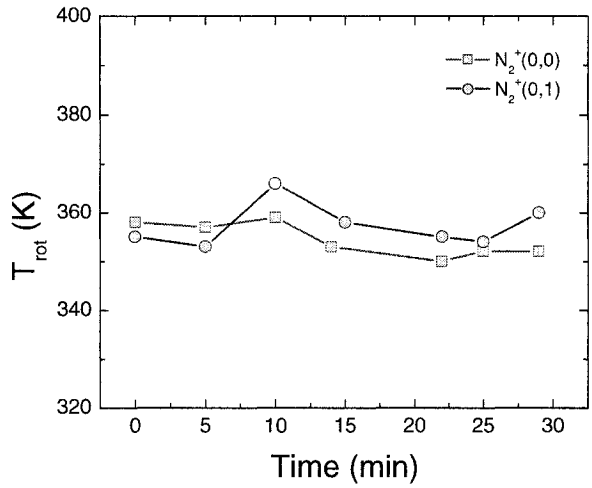

Figure 3.19 The time evolution of T_{rot} determined from SPS of N_2^+ (0,0) and (0,1) bands in the same location (r = 0); measured through lower transparent electrode (V_{pp} = 1.5 kV, f = 10 kHz, 3.0 mm planar gap, 5.7 slm of "pure" He.).

The rotational temperature, T_{rot}, measured through the lower transparent electrode (glass/ITO) in a central position of the discharge, r = 0, and determined from two different N_2^+ FNS bands (0,0) and (0,1), had the same values, ~ 360 K (Fig. 3.19); this shows that the APGD operated in a steady-state for more than 30 minutes.

Figure 3.20 shows the axial distributions of T_{rot} and I(391), in He APGD with V_{pp} of 2 kV, in the 3.0 mm planar gap, the grounded (dielectric) electrode being at z = 0 and z = 3.0 being the metallic HV electrode surface. We find $T_{rot} \approx 320$ K in mid-gap, but values about 30 K higher near both electrode surfaces. I(391), displayed two peaks, a smaller one ~ 0.4 mm in front of the metallic electrode, and a much higher one at $z \approx 0.75$ mm, above the dielectric surface. This will be explained in Chapter 4. Figure 3.21 shows radial measurements of T_{rot} and I(391) taken through the lower transparent electrode, r = 0 corresponding to the central axis of the discharge. Although I(391) was seen to decrease radially outwards from the centre, values of T_{rot} were seen to be independent of radial position, 350 ± 5 K.

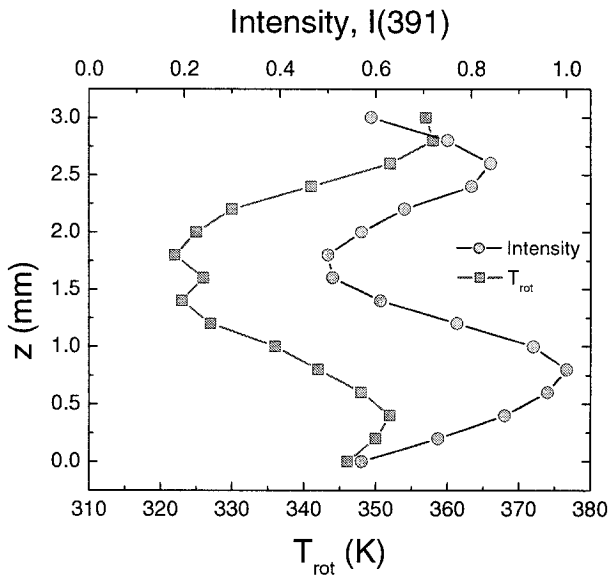

Figure 3.20 Typical axial distributions of T_{rot} and the bandhead intensity of $N_2^+(0,0)$ band, I(391), in pure He APGD in the 3.0 mm plane-plane gap (f = 10 kHz, V_{pp} = 2.0 kV).

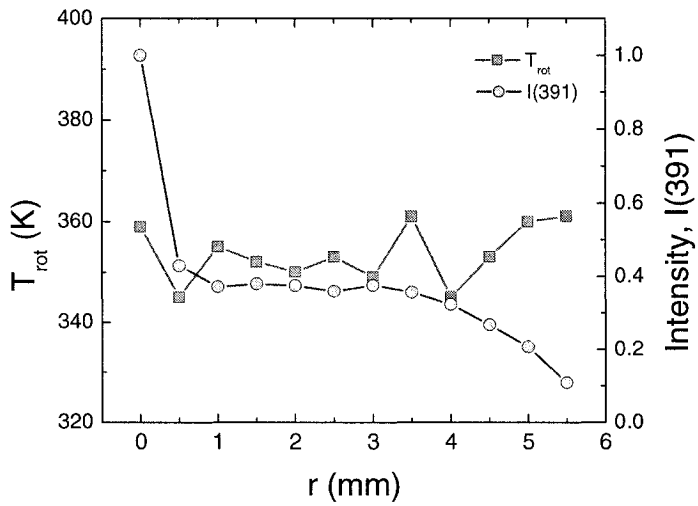

Figure 3.21 Typical radial distributions of T_{rot} and emission intensity at 391.4 nm, I(391), in pure He APGD in the 3.0 mm plane-plane gap (f = 10 kHz, V_{pp} = 1.5 kV).

3.4 Dependence of T_{rot} on other variables

3.4.1 Effect of N_2 concentration

In discussing Fig. 3.9, we noted that N_2 from presumed traces of air impurity dominated the emission spectra. Since the N_2^+ feature at 391.4 nm served for gas thermometry, it was logical to examine how T_{rot} evolved with rising N_2 concentration in deliberately "doped" He APGD. Figure 3.22 shows a plot of T_{rot} versus N_2 partial pressure at three axial positions in the 3.0 mm needle-plane gap, in a 2.0 slm flow of He: at the needle tip, at mid-gap and near the dielectric surface. While T_{rot} remained roughly constant at ~360 K in the latter location, it is seen to have risen near-linearly with increasing N_2 concentration at the others (note that values in kPa are roughly equivalent to molar %) up to about 2%. At this highest N_2 concentration, T_{rot} had the same value at the needle tip and in mid-gap. Figure 3.23 shows a similar plot, this time for the mid-gap position in a 1.0 mm cylinder-plane APGD. In this configuration, T_{rot} was found to be

independent of axial position. Again, T_{rot} is seen to have risen linearly by 120 K with increasing N_2 concentration up to ~ 1.4 %.

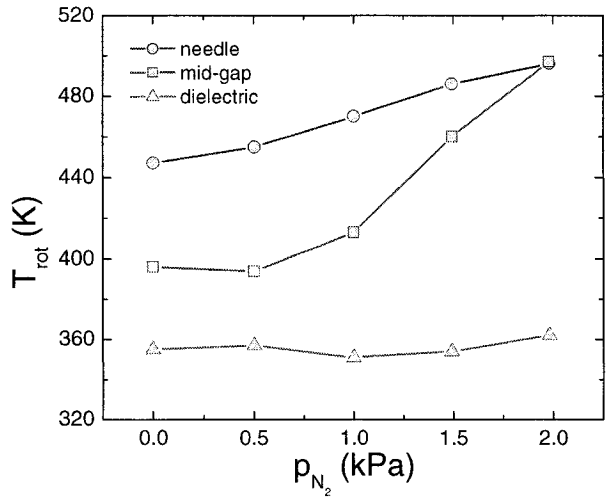

Figure 3.22 Plots of T_{rot} in three different positions during APGD in the 3.0 mm needle-plane gap, as a function of the partial pressure of N_2 gas admixed to the 2.0 slm flow of He (f = 10 kHz, V_{pp} = 2.9 kV).

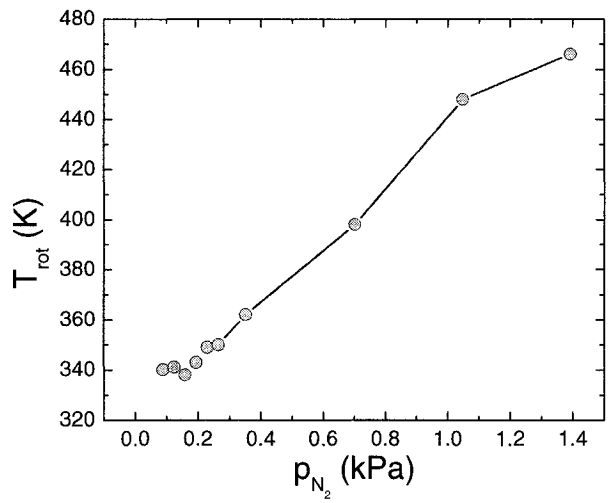

Figure 3.23 Plot of T_{rot} versus the partial pressure of N_2 gas admixed to the 5.7 slm flow of He; measurements were taken at mid-gap in a 1.0 mm cylinder-plane APGD (f = 10 kHz, V_{pp} = 1.9 kV).

In the case of the plane-plane configuration, T_{rot} increased almost linearly with N_2 partial pressure within the gap, but with different slopes as a function of axial position (Fig. 3.24). At the highest N_2 concentration, T_{rot} tended to be independent of axial position in the 1.5 mm gap. Bibinov *et al* [38, 137] reported T_{rot} measurement under experimental conditions not dissimilar from our's, namely between two 2.2 mm thick glass covered electrodes that separated a 1.5 mm gap, and using f = 19.7 kHz and V_{pp} between 1.5 and 2.0 kV. They observed a pseudo-glow discharge with about 10 current pulses per half-cycle, compared with 5 in our case at 2.0 kV and 10 kHz. In the two experiments, T_{rot} values in mid-gap position were almost equal in pure He, but differed significantly with increasing of N_2 concentration, Bibinov's values rising with a much greater slope (see Fig. 3.24). However, the reader should remember that T_{rot} in our case was obtained using only the rotational lines from the R branch between K = 6 and K = 14; had one used more lines to draw the Boltzmann plot, like in Bibinov's case, one would have obtained higher T_{rot} values, close to those reported by Bibinov (see Fig. 3.25). As discussed earlier, the intensity of the R(16) line can be perturbed by the (3,6) band emission of N_2 SPS (see Fig. 3.12), that increased with rising partial pressure of N_2 (see below); the increase in R(16) intensity accounts for the rise in apparent T_{rot} values.

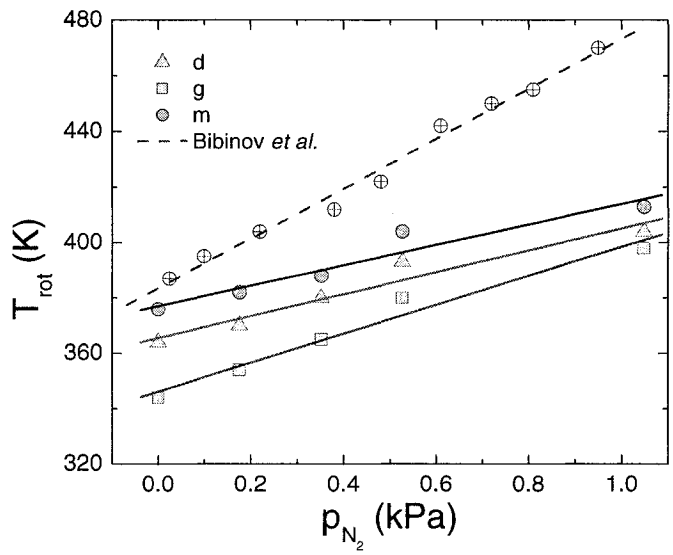

Figure 3.24 Plots of T_{rot} in three different positions during He APGD in a 1.5 mm gap, as a function of the partial pressure of N_2 (f = 10 kHz, V_{pp} = 2.0 kV); d, m: near dielectric and metal electrode surfaces, respectively, g: in mid-gap.

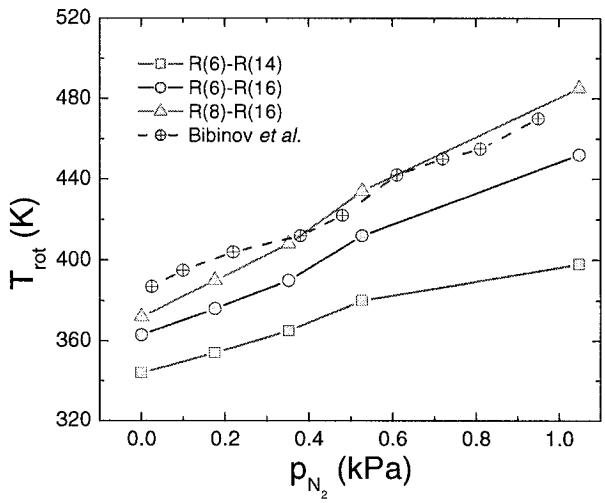

Figure 3.25 Three comparative plots of T_{rot} in the mid-gap position, determined from different sets of emission lines in the R branch manifold of $N_2^+(0,0)$, versus partial pressure of N_2 in He/N_2 mixtures, under conditions described in the caption of Fig. 3.24.

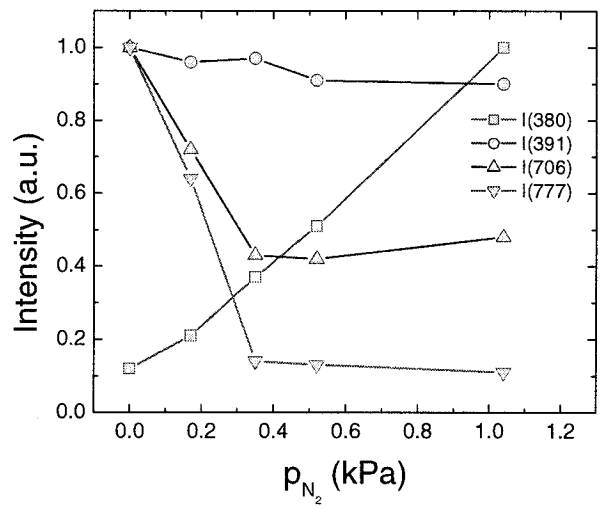

Figure 3.26 The relative emission intensities in mid-gap of a planar He APGD: N_2 SPS (0,2) bandhead at 380.5 nm, N_2^+ FNS (0,0) bandhead at 391.4 nm, He I at 706.5 nm and O I at 777 nm, versus partial pressure of N_2, under conditions described in the caption of Fig. 3.24.

Figure 3.26 shows the emission intensities versus partial pressure of N_2 in pseudo-glow discharges in He/N_2 mixtures, corresponding to various excited species, namely the N_2 SPS (0,2)

bandhead at 380.5 nm, the N_2^+ FNS (0,0) bandhead at 391.4 nm, He I at 706.5 nm and O I at 777 nm. While the N_2 emission intensity near 380 nm rose almost linearly, the other emissions decreased in intensity, some gradually (N_2^+), others more abruptly (He I, O I).

3.4.2 Effect of gap width, d, in the plane-plane configuration

Figure 3.27 shows the effect of gap width on T_{rot} values near the upper electrode in "pure" He APGD, when the gap was reduced from d = 3.0 to 0.25 mm. The discharge was sustained at 10 kHz, $V_{pp} \approx 2.7$kV, and manifested a single current pulse per half-cycle for d = 1.0 to 3.0 mm gap; for d < 1.0 mm, the discharge presented two current pulses per half-cycle. T_{rot} was seen to rise with decreasing d, while the total light emission intensity (PM signal) and N_2^+ (0,0) bandhead emission (I391) decreased in intensity.

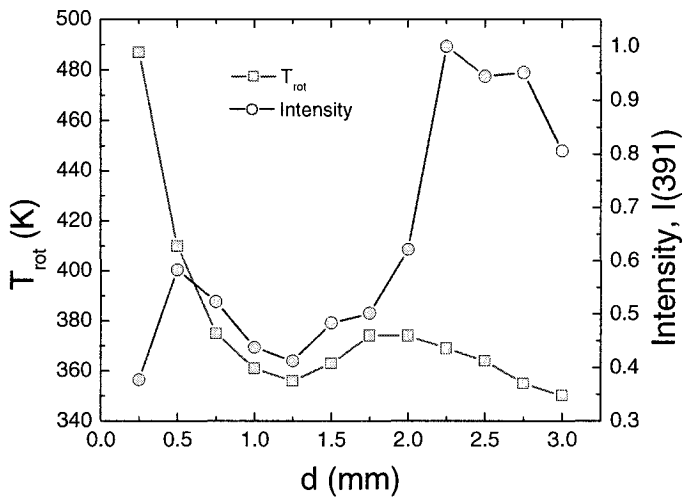

Figure 3.27 T_{rot} and I(391) near the metal electrode in a "pure" He APGD, versus gap width, d (f = 10 kHz, $V_{pp} \approx 2.7$ kV, plane-plane electrode configuration, 5.7 slm).

The gap width affected also the axial T_{rot} distributions in the discharges: Figure 3.28 shows the evolution of T_{rot} with gap width in three axial positions, namely near the dielectric surface ("d"),

in the mid-gap ("g"), and near the metallic electrode ("m"), where the highest T_{rot} values were observed, while the lowest were found in the mid-gap position. Clearly, T_{rot} was highest in the case of the smallest gap (d ≈ 0.5 mm) almost independent of axial position. As will be discussed in Chapter 4, those observations can readily be explained in terms of heat transfer.

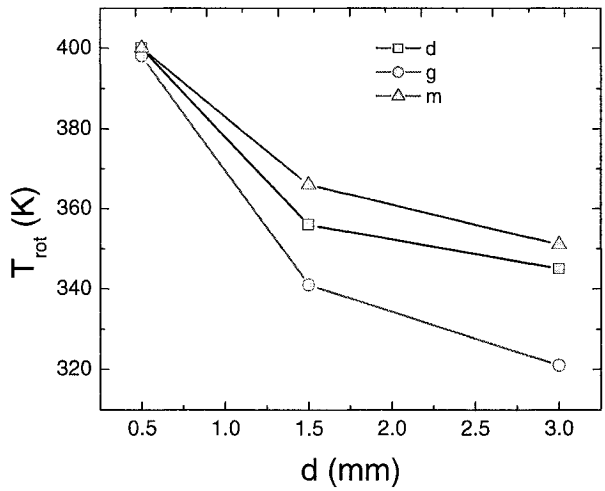

Figure 3.28 Plots of T_{rot} in three different axial positions in the gap during He APGD, versus gap width, d (f = 10 kHz, V_{pp} = 2.5 kV); d, m: near dielectric and metal electrode surfaces, respectively, g: in mid-gap.

3.4.3 Voltage (V_{pp}) and frequency (f) dependence

The relatively long (multi-μs) durations of current pulses observed in He APGD may give rise to certain dependences upon V_{pp} of measured values of I and T_{rot}. This becomes apparent upon examination of Fig. 3.6 (a), which depicts the current pulses in the two polarities for 10 kHz a.c. high voltage across the test cell. It can be perceived that the discharge in the positive polarity was initiated at V ≈ 620 V, which gave rise to a discharge pulse of 15 μs duration over which the voltage across the gap changed due to capacitive division by approximately 110 V. During this time interval, the increasing voltage imparted additional energy to the charge-carrying species in

their migration across the gap. The energy of the charge carriers, which increased with further voltage increases across the gap as the charge transfer progressed, was ultimately dissipated in collision processes. Figure 3.29 depicts plots of I(391) as a function of radial distance for the 3.0 mm needle-plane configuration with a 5.7 slm flow rate of "pure" He, with voltage across the gap as a parameter and f constant at 10 kHz. The intensity is seen to have been augmented at the more elevated V_{pp} values and decreased with increasing radial distance, r, as anticipated.

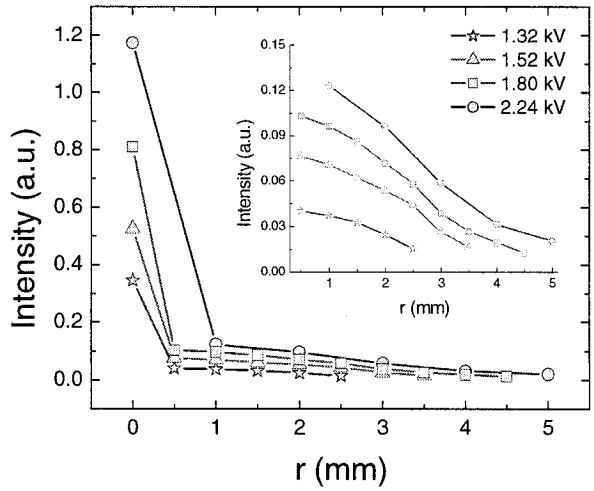

Figure 3.29 Radial profiles of I(391) corresponding to four different values of V_{pp}, for APGD in "pure" He in a 3.0 mm needle-plane gap, measured through the transparent planar electrode (see also Figs. 3.15 and 3.16; He flow = 5.7 slm, f = 10 kHz). The inset represent the same radial profiles of I(391) detailed for radii greater than 0.5 mm.

Here, a comment must be made concerning the V_{pp} parameter in the family of curves in Fig. 3.29. The magnitude of even the positive discharge current pulse in Fig. 3.6 (a) was extremely low and the voltage decrement step, (V_b-V_r), where V_b is the breakdown voltage and V_r the residual voltage, was so minute as to render it indiscernible on the scale of the ac voltage waveform across the gap in series with the dielectric. However, on an expanded scale (c.f. Ref. [28]), its position is perceptible from a slight irregularity in the sinusoidal trace. The voltage waveform across the needle-plane gap in series with the dielectric, presented in Fig. 3.6 (a), may thus be essentially considered as the voltage across the gap itself, because of its minuscule capacitance. In addition, since the waveform has no measurable abrupt discontinuity at the phase

of breakdown event, it can be considered as the apparent voltage across the gap just prior to breakdown. This is in contrast to the voltages across the cylinder-plane or plane-plane gaps for which the capacitive voltage drop across the dielectric must be taken into account; in addition, a further correction must be made for the V_{pp} value due to the breakdown discontinuities in the two half-cycles (c.f. Ref. [29]). Details for determining the voltage waveforms across the dielectric barrier, the apparent voltage and the actual voltage across the discharging gap may be found in Ref. [18]. The apparent existing voltage constitutes an important parameter, since it, together with the value of the breakdown voltage, determines the number of breakdowns per half-cycle.

The temperature, T_{rot}, (Fig. 3.30) is found to have exhibited a converse behaviour, diminishing with increasing V_{pp} and rising with increasing r. The reasons for this apparently conflicting result are not obvious at this time. A possible approach that may help resolve this question concerns the real and imaginary (reactive) power components in the discharge. The power loss in any discharge is composed of real and reactive components, the magnitudes of which depend upon the phase position of the discharge current pulse with respect to the voltage across the gap. Since the reactive power is returned to the source, a detailed analysis is necessary to determine the intricate dependences of I(391) and T_{rot} upon the overall power dissipated in the discharge in order to elucidate the reasons for the two apparently conflicting results.

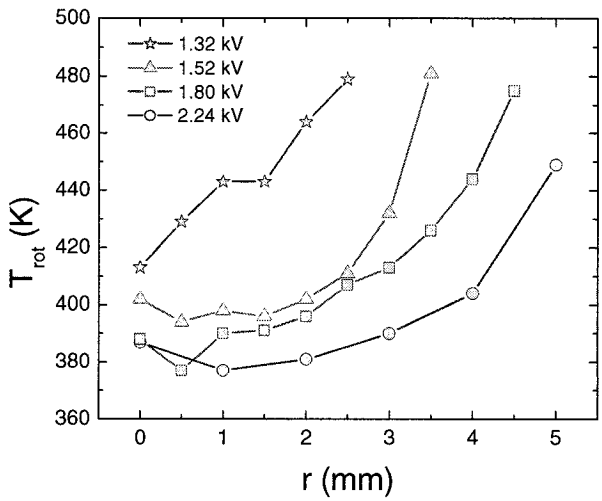

Figure 3.30 T_{rot} versus radial position at different applied voltages, V_{pp} (f = 10 kHz, for He APGD in a 3.0 mm needle-plane gap).

In Fig. 3.31, the values of T_{rot} and I(391) along the discharge axis (r = 0) are plotted versus the frequency, f, at a constant peak-to-peak voltage of 2.25 kV across the 3.0 mm needle-to-plane gap. The time-average values of T_{rot} indicated here were nearly constant (390 ± 5 K), and I(391) is seen to have increased with rising f, since for a discharge rate of one pulse per half-cycle an increase in f is equivalent to an increase in the number of pulses per unit time. It is important to emphasise here that the effects of both f and V_{pp} are inextricably connected in Fig. 3.31, because as f of the source was altered, the voltage changed as well. As f was decreased below 10 kHz, the half-period of the voltage wave obviously increased with the result that over the time interval of the electrical current pulse, the corresponding overall change in voltage over the same time interval was reduced. As a consequence, the resulting increase in T_{rot} with rising f was partially offset by its decrease with increasing voltage. Thus, while I(391) exhibited a strong increase (c.f. Fig. 3.31), not only due to increasing f but also due to increasing voltage, as in Fig. 3.29, the value of T_{rot} changed only marginally with increasing f because the latter was compensated by its inverse relationship with voltage.

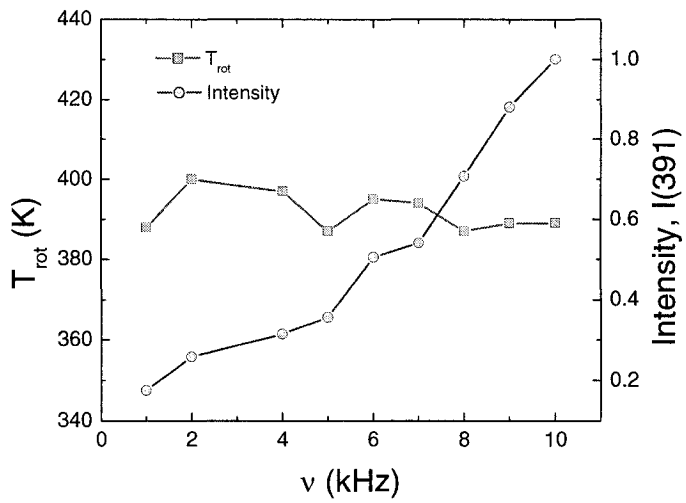

Figure 3.31 Plots of T_{rot} and I(391) versus f, for APGD in "pure" He in a 3.0 mm needle-plane gap, measured at r = 0 through the transparent planar electrode (He flow = 5.7 slm, V_{pp} = 2.2 kV).

In a d = 0.5 mm plane-plane gap configuration, T_{rot} decreased by almost 30 K when f = 10 kHz and V_{pp} was increase from 1.3 to 2.8 kV (Fig. 3.32), while the number of current pulses per half-

cycle rose from 1 to 3. For this short gap, T_{rot} was seen to be almost independents of the axial position, while I(391) was seen to increase linearly. We note that the highest emission intensity was observed in the mid-gap position, the case for d = 1.5 mm. However for d > 1.5 mm, I had maxima near both electrodes, and a minimum in the mid-gap position, (see Fig. 3.20), like in the other electrode configurations. The influence of V_{pp} on T_{rot} was much smaller in the case of higher d values. In Fig. 3.33, T_{rot} in the mid-gap positions for d = 0.5, 1.5 and 3.0 mm, are plotted versus V_{pp} at f = 10 kHz, and we note near-constant T_{rot} values in the case of larger gaps.

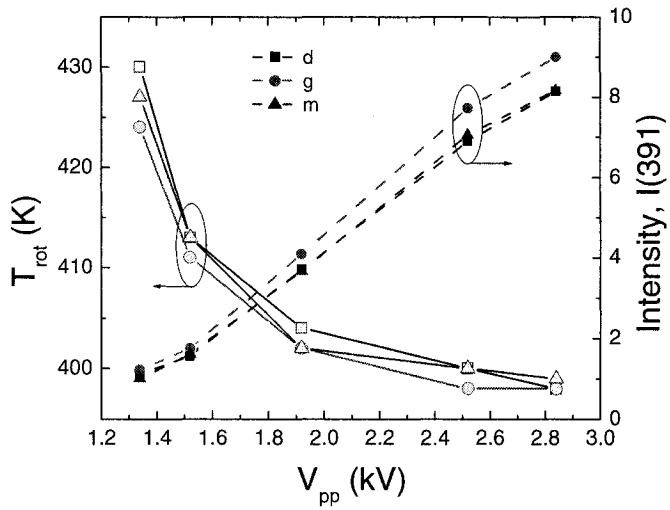

Figure 3.32 Plots of T_{rot} and I(391) in three different axial positions measured in a d = 0.5 mm gap in He APGD (f = 10 kHz); d, m: near dielectric and metal electrode surfaces, respectively, g: in mid-gap.

When f was increased from 2 to 10 kHz at constant V_{pp} = 2.5 kV, T_{rot} manifested a linear reduction by about 25 K in the 0.5 mm gap (Fig. 3.34), while, I(391) increased near-linearly, the highest value occurring in the mid-gap position. However, in the case of longer gaps, for example d = 1.5 mm, Fig. 3.35 shows a more complex behaviour of T_{rot} with rising f: For, f < 4 kHz, T_{rot} was almost independent of the axial position but decreased slightly with rising f, while

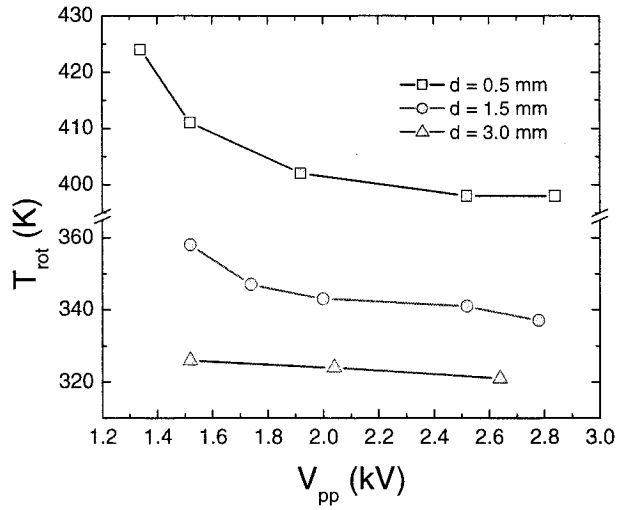

Figure 3.33 T_{rot} versus V_{pp} for "pure" He APGD at three different gap widths (f = 10 kHz).

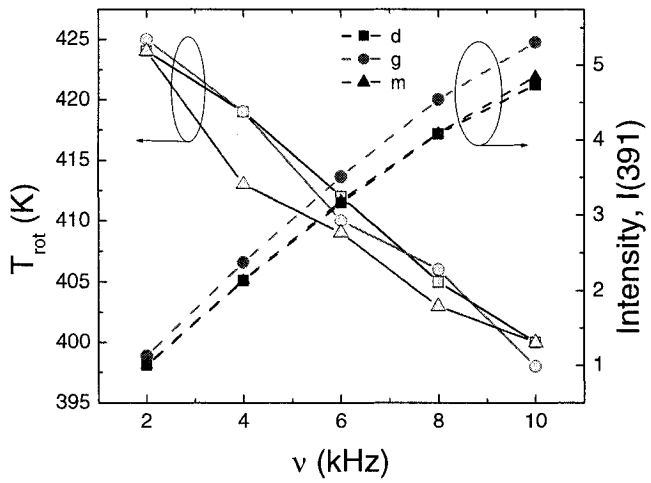

Figure 3.34 T_{rot} and I(391) in three different axial positions plotted versus f, for "pure" He APGD in a 0.5 mm planar gap; "d" - dielectric, "g" – mid-gap, "m" – metallic electrode (V_{pp} = 2.5 kV).

for higher f, T_{rot} displayed different dependences at different positions in the gap: nearly constant at the dielectric surface, decreasing slightly and rising sharply with increasing f at mid-gap and at the metal surface, respectively. However, for a 3.0 mm gap T_{rot} decreased in the entire gap with rising f (Fig. 3.36), as in the case of the shortest (0.5 mm) gap. T_{rot} values were generally

highest near the metallic (high-voltage) electrode, as can be seen in Figs 3.34 to 3.36. Possible explanations about the observations presented above are discussed in Chapter 4.

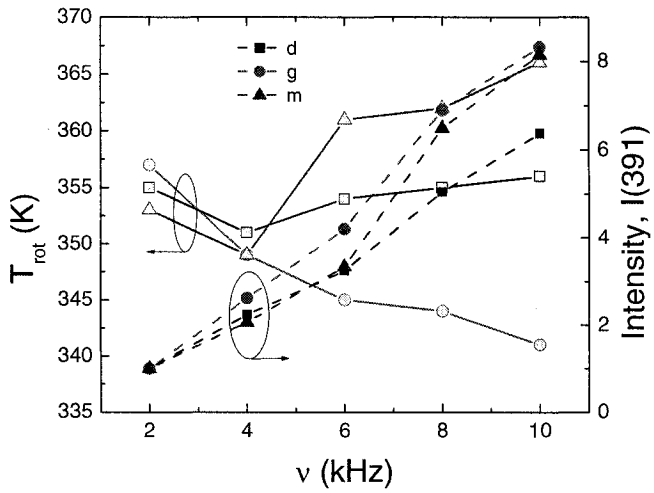

Figure 3.35 T_{rot} and I(391) in three different axial positions plotted versus f, for "pure" He APGD in a 1.5 mm planar gap; "d" - dielectric, "g" – mid-gap, "m" – metallic electrode (V_{pp} = 2.5 kV).

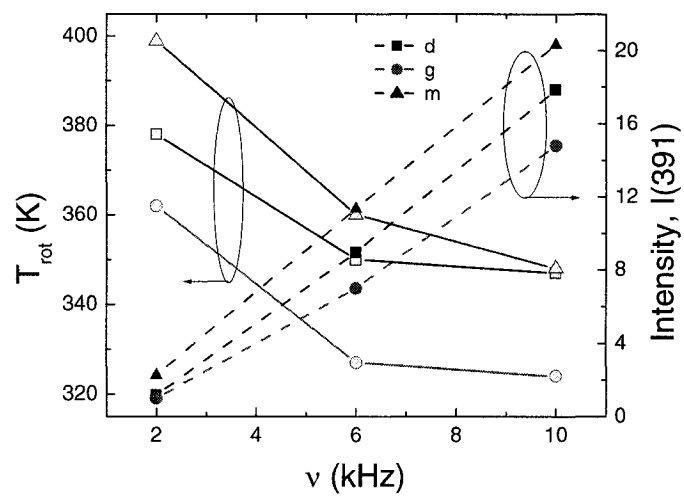

Figure 3.36 T_{rot} and I(391) in three different axial positions plotted versus f, for "pure" He APGD in a 3.0 mm planar gap; "d" - dielectric, "g" – mid-gap, "m" – metallic electrode (V_{pp} = 2.5 kV).

Chapter 4 GENERAL DISCUSSION

There is now abundant evidence that APGD in helium possesses the usual structure of a dc glow discharge, namely a cathode layer, a Faraday dark space, a positive column, and anode glow [25, 33, 65, 75, 76]. These features are observed here in Figs. 3.5, 3.8, 3.13, 3.14, 3.17 and 3.20, for example. There also exists agreement that Penning ionisation of impurities (for example, N_2 [58]) plays an important role in providing copious supplies of "seed electrons" between APGD current pulses, and that these facilitate the formation of an uniform, diffuse APGD, as opposed to spark-type breakdown [21, 22, 25, 28-36, 65, 75, 76]. This, too, is convincingly borne out by our present and earlier data [22]. Also, the relative magnitudes of the emission intensities measured at the electrodes and the intervening gap space in the present investigation are substantiated by discharge formation studies [124], which indicate the occurrence of a greatly enhanced electric field at the cathode and a correspondingly lower field at the anode, with a pronounced reduction of the field in mid-gap as the discharge develops.

While research on APGD in He published by other authors almost exclusively deals with parallel planar electrodes, hence quasi-uniform electric fields, we have focused our attention here also on inhomogeneous fields from needle-plane, cylinder-plane and sphere-plane electrode configurations, mostly on the first of those former. This geometry has the advantage of being "uni-dimensional", which facilitates observations of the types we have conducted, including of radial discharge propagation phenomena, to be addressed presently. Another original feature of this work are the temporally and spatially-resolved measurements of T_{rot}, a logical addendum to the spectroscopic measurements.

Let us first return to the glow discharge structure mentioned above and to related observations: as early as 1999, Tochikubo *et al.* [75] showed spatiotemporal optical emission of He I (706.5 nm) and N_2 (337.1 nm) in a planar-electrode He discharge at 100 kHz. The threshold energy of these transitions being very different, 22.7 eV and 11.03 eV, respectively, the former line may be associated with regions of high electric fields, while the latter also occurs in low-field regions. Those authors, and others more recently [76], observed intense luminosity near the instantaneous cathode as well as N_2 emission in the positive column of the He APGD. Clearly, strong cathode glow and less intense luminosity near the anode can be noted in our Figs. 3.13 and 3.17, for the

needle- and cylinder-based geometries, respectively. Even in the plane-plane geometry, the cathode glow is stronger than the luminosity near the anode (Fig. 3.20). The spatiotemporally and spectrally-resolved features of the former, portrayed in Figs. 3.5(a) and 3.14, shed much further light on events occurring in the discharge. For instance, during the 3 or 4 μs period including and following discharge propagation from the needle-anode to the dielectric cathode, all three species monitored (N_2, N_2^+, and He I) manifest their strongest emission intensities in the cathode layer less than 1 mm above the dielectric surface. This is particularly striking for the case of the He I line at 706.5 nm, while the other two emissions at 380.5 and 391.4 nm are also quite intense in the remainder of the 3.0 mm gap, including near the anode, z = 3.0. As mentioned above, the intense He I emission indicates the presence of a strong electric field, associated with very energetic (> 22.7 eV) secondary electrons resulting from ion bombardment of the cathode surface. Recalling that N_2^+ is primarily created by Penning ionisation, eq. (1.4), its emission intensity in the gap is indicative of the density of He* and He_2 species, while near the cathode surface it may also be due to the "hot" electrons, eq. (1.2). Evidently, all of those possess more than the 15.6 eV energy required to ionize N_2. Regarding the long-duration luminous emission near the needle electrode during both half periods of ac voltage, especially the negative one (see Fig. 3.5(b)), this is presumably due to the strong electric field concentration in the vicinity of the 20 μm needle tip radius (with a field enhancement factor of 46), which results in (Fowler-Nordheim) field emission of "hot" electrons [140]. However, in the case of Ne APGD no strong luminous emission near the needle electrode is observed during the positive half-period that precedes discharge propagation (Fig. C.2). In other words, the presence of the former emission appears to be particular for the case of He APGD (Fig. 3.3, 3.5(a) and 3.8) in the needle-plane geometry, and this can indicate the presence of a high electron density in the gas before breakdown. These electrons may be the result of Penning ionisation (eq. (1.4)), that in the case of He is more pronounced than in Ne, considering their metastable energies of 20 and 16.6 eV, respectively, as will also be discussed further below.

We now turn to the luminous ring that propagates along the cathode surface, as illustrated in Figs. 3.2 and 3.4(a), and in earlier reports [28, 32]. The observed phenomenon may be explained in terms of surface charging effects. In a glow discharge, the expansion of the discharge channel is driven by the radial space charge field induced expansion of the ion channel, enhanced by the feedback via the ion impact-induced electron emission at the cathode; there are also metastable

impact and photoemission effects, but these are negligible compared to those due to ions [34, 35, 36, 124]. In the incipient stages of the discharge, ion trapping occurs first at and in the vicinity of the centre of the cathode (r = 0, z = 0); the deposited ions on the dielectric cathode surface create a counter field, which repels the subsequent incoming ions from the ionic space charge layer adjacent to the cathode. If the number of impacting ions is reduced below a certain critical level necessary to maintain electron emission from the cathode and thereby to sustain the discharge process in the central region of the cathode, the emission intensity falls in that region, giving rise to a luminous annulus. This annulus grows because the discharge channel expands, and the dark central area increases in size due to surface charging beneath the expanding annulus. The expansion of the discharge channel and the outward propagation of the luminous annulus is determined by the magnitude and geometry of the radial space charge field. With electrode systems having rotational symmetry, a Gaussian distribution is likely, as illustrated by Fig. 1.18. For example, with parallel-plane electrodes, the radial component of the space charge field, impelling the radially-outward migration of the ions, is Gaussian in form, its maximum being located approximately at r/2 [35]; it is noteworthy that Anderson *et al.* [76] report an expanding annular glow in their parallel-plane He discharge.

The foregoing process may be further assisted by the nonlinear ponderomotive force [140],

$$\vec{F} = -\frac{\omega_p^2}{\omega^2}\vec{\nabla}\frac{\langle E^2 \rangle}{8\pi} \tag{4.1}$$

where E is the electric field, and ω and ω_p are the voltage and plasma angular frequencies, respectively. This force provides a net drift to the electrons and eventually the ions, from the strong field region to the weak-field region, in other words, radially outward. Considering that $\omega_p \propto n_e$, the electron density in the plasma, and that ω^2 is relatively small here, the value of $(\omega_p / \omega)^2$ is quite large under the present conditions. It is interesting to note that the speed of radial spreading calculated from Fig. 3.4(a), $v \approx 10^3$ m s^{-1}, is quite close to Anderson's value, 2×10^3 m s^{-1}, in spite of the very different electrode geometries. On the basis of Fig. 3.15, which shows roughly parallel intensity decay curves with increasing radius for all of the emission lines examined, the cathode layer is still strong enough at r > 2 mm to provide the "hot" electrons (>22.7 eV) required to excite He I at 706.5 nm. It is also noteworthy that we have observed many of the same phenomena reported here for the case of APGD in Ne, including the above-

described ring-spreading (see Figs. C.1 and C.2), but not in the case of Ar [32]. The presumed reason is that metastables of the former two gases, He and Ne, have energies of 20 and 16.6 eV, respectively, above the 15.6 eV ionisation threshold of N_2, while Ar metastables (11.6 eV) are insufficiently energetic.

The dielectric that covers the lower planar electrode has a very important effect on the discharge characteristics through γ, the secondary electron emission coefficient, and through its capacitance (Figs. 3.5, 3.8 and C.3). We never observed pseudo-glow discharges in the needle-plane configuration, but in Fig. 3.8 we can clearly notice the presence of a second discharge that propagates 1 mm (Fig. 3.8(a)) and 1.5 mm (Fig. 3.8(b) in the gap before disappearing. An APGD can be even obtained between two metallic surfaces, if the planar surface is a metal at floating potential, or if an equivalent capacitance is introduced in series with the discharge circuit (Fig. C.4). In the former case, the discharge is very rapid and presents a different spatial emission, with maximum intensity near the needle tip during the positive half-cycle, like in the case of a Townsend discharge. Near the planar surface, the discharge intensity is relatively low and there is no radial spreading on the lower electrode, due to uniform positive charge distribution on the conducting surface. The maximum value of the electric field obviously exists at the shortest distance between the two (metallic) electrodes, namely below the needle tip.

Finally, we discuss the measurements of T_{rot}, based on the rotational band spectrum adjacent to the 391.4 nm N_2^+ bandhead. In section 3.3 we already compared and commented upon time-averaged T_{rot} values along the axes of the needle- (Fig. 3.13), cylinder- (Fig. 3.17) and planar (Fig. 3.20) electrode configurations. It should be emphasized that these values are in keeping with $T_{rot} \approx 380$ K reported by Bibinov *et al.* [38] for planar discharge geometry. Like those authors, we are convinced that the kinetic and rotational T values are identical for "pure" He and He/N_2 mixtures containing up to 2% N_2. Also like them, we have examined T_{rot} in parallel-plane He APGD; for the three geometries we have studied, T_{rot} values measured at z = 3.0 mm were found to be $T_n \approx 440$ K, $T_c \approx 390$ K, and $T_p \approx 360$ K, where "n" "c", and "p" refer to "needle", "cylinder" and "plane", respectively. On the other hand, at z = 0 the temperatures were virtually identical, $T_{rot} \approx 360 \pm 10$ K, in the three cases. Those results can probably be explained by greater plasma heating in the cases where field concentrations exist (cases "n" and "c"), combined with improved heat exchange near the more massive electrodes.

T_{rot} presents an axial dependence that is strongly influenced by d, V_{pp}, and f, and by the gas composition. For d = 3.0 mm in the plane-plane geometry, T_{rot} has a minimum of about 320 K in the mid-gap position, and a value of about 355 K near the electrode surfaces (Fig. 3.20). When the gap is decreased, we observed a maximum T_{rot} value in the mid-gap when d < 1.5 mm width, and a rise in the entire gap to about 400 K for d = 0.5 mm, independent of the axial position (Figs 3.27 and 3.28). The effects of V_{pp} and f on T_{rot} were most prominent in the case of small d values: Figs. 3.22, 3.33, 3.34 and 3.36 show that T_{rot} increased at by about 30 K for a 0.5 mm gap. A similar situation can be also observed in the needle-plane configuration (Fig. 3.30), the most surprising aspect being the "counter-intuitive" fact that T_{rot} was highest for the lowest V_{pp} values.

The relationship between T_{rot} and N_2 concentration in the He/N_2 mixtures, Figs. 3.23 and 3.24, shows a near-linear rise with a slope of ~ 100 K (% N_2)$^{-1}$. Rising N_2 concentration in the discharge, is seen in Fig. 3.26 to result in an almost linear increase in emission intensity at 390 nm, hence in a strong influence on the average electron energy: The concentration of high-energy electrons required to excite He I decreases rapidly for [N_2] ≤ 0.4 %vol; the emission intensity from O I at 777 nm deceases even more rapidly and virtually disappears under these same conditions. The fact that the emission intensity of N_2^+(0,0) at 391.4 nm decreases very slowly with rising N_2 concentration suggests that the radiative excited states $N_2^+(B^2\Sigma_u^+)$ are mostly created by electron impact collisions, and that Penning ionization makes only a relatively small contribution. This result also supports the view that T_{rot} is in fact equal to the kinetic energy of the neutral species in the discharge.

Further strong evidence that T_{rot} measured with the help of the 391.4 nm N_2^+emission is near-identical to the gas kinetic temperature comes from the work of W. Choe and his collaborators [141, 142]. In a first article [141], they reported optical measurements of temperature in atmospheric pressure 13.56 MHz RF discharges in He + 4% Ar gas mixture, using OH molecular emission bands near 308 and 309 nm. The optically determined values, between 400 and 700 K, depending upon input power, were found to agree well with gas temperatures measured with thermocouples. In a second article [142], they compared T_{rot} values determined from OH (308 nm), N_2^+ (391 nm) and O_2 (768 nm region) measured and calculated band spectra, determined from the case of an atmospheric pressure ac discharge in 60% He + 40% O_2 gas mixture. In one particular experiment they found T_{rot} values of 930, 935 and 920 K from the

three species above, respectively, values that agreed very closely with the gas temperature measured using a thermocouple. The authors conclude that T_{rot} measurements, even with a spectrometer of modest resolution, can provide reliable thermometric data.

Bibinov's [38] and Choe's [141, 142] strong evidence that T_{rot} measurements in atmospheric pressure discharges in "pure" He or He-rich gas mixtures are reliable for determining the true gas temperature can only reinforce the belief of the present author. With this in mind, however, the research we report here leaves us with some intriguing unanswered questions, foremost the rise of T_{rot} with increasing r during radial spreading of the annular glow region (Fig. 3.16) in needle-plane geometry. However, in the case of a planar discharge, a constant value of about 350 K, independent of the radial position, was observed (Fig. 3.21). The mechanism we discussed earlier in this section to explain radial spreading may provide some clues, for example a drastic change in plasma energetics that favours gas heating as opposed to excitation by hot electrons, as the outward-moving plasma region weakens. These questions warrant further investigation, still in progress in this laboratory.

Chapter 5 CONCLUSION

The main objective of this research was to study the influence of different dielectric barrier discharge parameters, namely the electrode geometries, gas gap width, amplitude and frequency of applied a.c. high voltage, and the concentration of N_2 in He, on the spatial (axial and radial) distributions of gas temperature in the atmospheric pressure glow discharge (APGD) in He, by using optical emission spectroscopy (OES).

In order to achieve the objective, an existing experimental set-up was modified, and the APGD produced in He and He/N_2 mixtures were investigated by OES with a good spatial and/or spatio-temporal resolution. The gas kinetic temperature was assumed to be equal to the rotational temperature, T_{rot}, determined from the emission spectrum of the (0-0) R-branch of FNS $N_2^+(B^2\Sigma_u^+ - X^2\Sigma_g^+)$ bands near 391 nm. Bibinov's [38] and Choe's [141, 142] published results present strong evidence that T_{rot} measurements in atmospheric pressure discharges in "pure" He or He-rich gas mixtures are, indeed, reliable for determining the true gas temperature, T.

The axial distributions of T in APGDs obtained in four different electrode geometries, namely needle-, cylinder-, sphere- and plane-plane, were evaluated. For the cases of the first and the last of those electrode geometries, the radial distributions of T were also determined.

The gas in the discharge gap appears to have regions of higher temperatures close to each of the two electrode surfaces. In the plane-plane geometry T values in the vicinity of the two electrode surfaces are almost the same, while in the needle-plane geometry a much higher T value is measured near the electrode tip. The gas in the mid-gap position is cooler in all of the geometries, being almost at ambient temperature in the case of large gaps.

When reducing the gap width, d, it was generally observed that T increased and tended to be independent of the axial position; furthermore the axial distribution of light emission in the gap, I, changed from one with two maxima near the two electrodes, to only one maximum in the mid-gap position.

Raising N_2 concentration (up to ~ 1 vol %) in the discharge led to a near-linear rise of T within the entire gap, with a slope of ~ 100 K $(\%\ N_2)^{-1}$, behaviour also reported by Bibinov *et al* [38].

The gas temperature manifested an unexpected radial distribution in the case of the needle-plane geometry: While in the plane-plane geometry T was nearly independent of the radial position, r, T was found to increase with increasing r in the needle-plane case, even though I decreased. Another surprising result, observed in all of the electrode geometries, was that T rose with decreasing applied voltage amplitude or frequency. This effect was quite pronounced at low frequency, when the intensity of light emission from the gap was very low.

The interpretation of these experimental results is difficult in the absence of a theoretical model that can simulate the discharge conditions. However, the study of spatio-temporal discharge propagation in He and He/N_2 mixtures, and also in Ne and N_2, using an ultra-high speed digital camera has permitted us to develop a plausible theoretical explanation for the axial T distributions in discharges. However, the questions of radial dependence of T and also of its dependence on applied voltage and frequency are still elusive at this time.

APGD is still far from being well understood and controlled, and more research is required in future for its full industrial application. In this present research, we have investigated only a very small portion of this extremely complex phenomenon, named "APGD", and we have identified ways to improve the experimental set-up. For instance, with the present set-up it is too expensive to study APGD in Ne because an excessively high gas flow rate is needed. On the other hand, the current system can allow many useful experiments to be realized, from the influence of the dielectric barrier (composition, surface, thickness) on discharge behaviour, to experiments with other electrode geometries and different gas mixtures that may be of interest in industrial applications.

REFERENCES

[1] S. Habibi, M. Totsuka, J. Tanaka, T. Kinoshita and S. Matsumoto, *J. Vac. Sci. Technol. B* **13** (1995) 247

[2] I.W. Boyd and J.Y. Zhang, *Nucl. Instrum. and Meth. In Phys. Res.(NIM B) B* **121** (1997) 349

[3] T. Yokoyama, M. Kogoma, S. Kanazawa, T. Moriwaki, and S. Okazaki, *J. Phys. D: Appl. Phys.* **23** (1990) 374

[4] P. Bergonzo and I.W. Boyd, *J. Appl. Phys.* **76** (1994) 4372

[5] J.Y. Zhang and I.W. Boyd, *Electron. Lett.* **33** (1997) 911

[6] A. Sobel, *IEEE Trans. Plasma Sci.* **19** (1991) 1032

[7] J.P. Boeuf and H. Douyeux, *Europhys. News* **27** (1996) 46

[8] T. Nozaki, Y. Kimura, and K. Okazaki, *J. Phys. D: Appl. Phys.* **35** (2002) 2779

[9] T. Urakabe, S. Harada, T. Saikatsu and M. Karino, 7th International Symp. on the Science and Technology of Light Sources (Kyoto, Japan) (1995) 159

[10] L.A. Rosocha, Processing of hazardous chemicals using silent-discharge plasmas Plasma Science and the Environment, W. Manheimer et al., eds. (Woodbury, NY: American Institute of Physics) (1997) 261

[11] A.C. Gentile and M.J. Kushner, *J. Appl. Phys.* **78** (1995) 2074

[12] D.G. Storch and M.J. Kushner, *J. Appl. Phys.* **73** (1993) 51

[13] M. Laroussi, G. S. Sayler, B. B. Glascock, B. McCurdy, M. E. Pearce, N. G. Bright, and G. M. Malott, *IEEE Trans. Plasma Sci.* **27** (1999) 34

[14] Y. Sawada, H. Tamaru, M. Kogoma, M. Kawase, and K. Hashimoto, *J. Phys. D: Appl. Phys.* **29** (1996) 2539

[15] Y. Sawada, S. Ogawa, and M. Kogoma, *J. Adhes.* **53** (1995) 173

[16] U. Kogelschatz, *Plasma Chem. Plasma Process.* **23** (2003) 1

[17] R. Bartnikas, *Br. J. Appl. Phys., J. Phys. D (Ser. 2)* **1** (1968) 659

[18] R. Bartnikas, *J. Appl. Phys.* **40** (1969) 1974

[19] R. Bartnikas, *Archiv. für Electrotechnik* **52** (1969) 348

[20] R. Bartnikas, *IEEE Trans. Electr. Insul.* **EI-6** (1971) 63

[21] I. Radu, R. Bartnikas, G. Czeremuszkin and M.R. Wertheimer, *IEEE Trans. Plasma Sci.* **31** (2003) 411

[22] I. Radu, R. Bartnikas and M.R. Wertheimer, *IEEE Trans. Plasma Sci.* **31** (2003) 1363

[23] U. Kogelschatz, *IEEE Trans. Plasma Sci.* **30** (2002) 1400

[24] S. Okazaki, M. Kogoma, M. Uehara and Y. Kimura, *J. Phys. D: Appl. Phys.* **26** (1993) 889

[25] F. Massines, A. Rabehi, P. Decomps, R. Ben Gadri, P. Ségur, and C. Mayoux, *J. Appl. Phys.* **83** (1998) 2950

[26] J.R. Roth, Industrial Plasma Engineering: Volume I—Principles, Institute of Physics, Bristol, UK, (1995)

[27] S. Guimond, I. Radu, G. Czeremuszkin, D. Carlsson and M.R. Wertheimer, *Plasmas Polym.* **7** (2002) 71

[28] I. Radu, R. Bartnikas, and M. R. Wertheimer, *J. Phys. D, Appl. Phys.* **36** (2003) 1284

[29] I. Radu, R. Bartnikas, and M. R. Wertheimer, *J. Phys. D: Appl. Phys.* **37** (2004) 449

[30] I. Radu, R. Bartnikas, and M. R. Wertheimer, *J. Appl. Phys.* **95** (2004) 5994

[31] I. Radu, R. Bartnikas, and M. R. Wertheimer, *J. Phys. D: Appl. Phys.* **38** (2005) 539

[32] I. Radu, R. Bartnikas and M.R. Wertheimer, *IEEE Trans. Plasma Sci.* **33** (2005) 280

[33] F. Massines, P. Ségur, N. Gherardi, C. Khamphan, A. Ricard, *Surf. and Coatings Technol.* **174 –175** (2003) 8

[34] J.P.Novak and R. Bartnikas, *J. Appl. Phys.* **62** (1987) 3605

[35] J.P.Novak and R. Bartnikas, *J. Appl. Phys.* **64** (1988) 1767

[36] R. Bartnikas and J.P.Novak, *IEEE Trans. Plasma Sci.* **20** (1992) 487

[37] A. Hynes, W. Castanga, K. Carr, S. O'Shea, T. Herbert, Proc. 9th Int. Symp. on High Pressure, low Temperature Plasma Chemistry (Hakone IX), Padova, Italy (2004)

[38] N.K. Bibinov, A.A. Fateev, K. Wiesemann, *Plasma Sources Sci. and Technol.* **10** (2001) 579

[39] T. Yokoyama, M. Kogoma, T Moriwaki and S. Okazaki, *J. Phys. D: Appl. Phys.* **23** (1990) 1125

[40] M. Kogoma and S. Okazaki, *J. Phys. D: Appl. Phys.* **27** (1994) 1985

[41] A Fridman, A Chirokov and A Gutsol, *J. Phys. D: Appl. Phys.* **38** (2005) R1

[42] J.J. Coogan and A.D. Sappey, *IEEE Trans. Plasma Sci.* **24** (1996) 91

[43] B. Eliasson and U. Kogelschatz, *IEEE Trans. Plasma Sci.* **19** (1991) 309

[44] B. Eliasson, M. Hirth, and U. Kogelschatz, *J. Phys. D: Appl. Phys.* **20** (1987) 1421

[45] D. Braun, U. Kuchler, and G. Pietsch, *J. Phys. D: Appl. Phys.* **24** (1991) 564

[46] D. Braun, V. Gibalov, and G. Pietsch, *Plasma Sources Sci. Technol.* **1** (1992) 166

[47] G. Steinle, D. Neundorf, W. Hiller, and M. Pietralla, *J. Phys. D: Appl. Phys.* **32** (1999) 1350

[48] S. Martin, S. Carré, C. Jimenez, N. Gherardi and F. Massines, *16th International Symposium on Plasma Chemistry, ISPC16,* Taormina, Italy, (2003)

[49] D. Trunec, A. Brablec and J. Buchta, *J. Phys. D: Appl. Phys.* **34** (2001) 1697

[50] Yu.B. Golubovskii, V.A. Maiorov, J. Behnke and J.F. Behnke, *J. Phys. D: Appl. Phys.* **35** (2002) 751

[51] P. Ségur and F. Massines, *Proc. 13th Int. Conf. on Gas Discharges and their Applications, GD 2000,* (2000) 15

[52] Yu.B. Golubovskii, V.A. Maiorov, J. Behnke and J.F. Behnke, *J. Phys. D: Appl. Phys.* **36** (2003) 39

[53] D. Trunec, A. Brablec, F. Stastny, *Contrib. Plasma Phys.* **38** (1998) 435

[54] A.J. Palmer, *Appl. Phys. Lett.* **25** (1974) 138

[55] J.L. Levatter, S.-C. Lin, *J. Appl. Phys.* **1** (1980) 210

[56] J.P. Novak and R. Bartnikas, *Proc. IX Int. Conf. on Gas Discharges and Applications*, Venice, (1988) 375

[57] R. Bartnikas and J.P. Novak, *IEEE Trans. on Electrical Insulation* **27** (1992) 3

[58] G. Nersisyan, T. Morrow, and W.G. Graham, *App. Phys. Lett.* **85** (2004) 1487

[59] J.R. Roth, Industrial Plasma Engineering: Volume II —Applications to Nonthermal Plasma Processing, Institute of Physics, Bristol, UK (2001)

[60] Yu.B. Golubovskii, V.A. Maiorov, J. Behnke and J.F. Behnke, *J. Phys. D: Appl. Phys.* **36** (2003) 975

[61] N. Gherardi, E. Croquesel and F. Massines, *16th International Symposium on Plasma Chemistry, ISPC16,* Taormina, Italy, (2003)

[62] T. Nozaki, Y. Unno and K. Okazaki, *Plasma Sources Sci. Technol.* **11** (2002) 431

[63] D.G. Boyers and W.A. Tiller, *Appl. Phys. Lett.* **41** (1982) 28

[64] N. Merbahi, N. Sewraj, F. Marchal, Y. Salamero and P. Millet, *J. Phys. D: Appl. Phys.* **37** (2004) 1664

[65] L. Mangolini, C. Anderson, J. Heberlein and U. Kortshagen, *J. Phys. D Appl. Phys.* **37** (2004) 1021

[66] Yu.B. Golubovskii, V.A. Maiorov, J.F. Behnke, J. Tepper and M. Lindmayer, *J. Phys. D: Appl. Phys.* **37** (2004) 1346

[67] N. Naudé, J.-P. Cambronne, N. Gherardi and F. Massines, *J. Phys. D: Appl. Phys.* **38** (2005) 530

[68] F. Massines, G. Gouda, N. Gherardi, M. Duran, E. Croquesel, *Plasmas and Polymers* **6** (2001) 35

[69] N. Gherardi, G. Gouda, E. Gat, A. Ricard and F. Massines, *Plasma Sources Sci. Technol.* **9** (2000)

[70] F. Massines, P. Ségur, N. Gherardi, C. Khamphan and A. Ricard, *Proc. 8th International Conference on Plasma Surface Engineering (PSE 2002,* (2002)

[71] P.F. Little, in: Electron Emission Gas Discharges I, Springer Verlag, (1956) 574

[72] Y. Motoyama, H. Matsuzaki and H. Murakami *IEEE Trans. on Electron Devices* **48** (2001) 1568

[73] J.P. Boeuf, *J. Phys. D Appl. Phys.* **36** (2003) R53

[74] V. v Elsbergen, P.K. Bachmann and G. Zhong, *Int. Display Workshop* **IDW'00** (2000) 687

[75] F. Tochikubo, T. Chiba, and T. Watanabe, *Jpn. J. Appl. Phys., Part 1* **38** (1999) 5244

[76] C. Anderson, M. Hur, P. Zhang, L. Mangolini, and U. Kortshagen, *J. Appl. Phys.* **96** (2004) 1835

[77] S. Kanazawa, M. Kogoma, T. Moriwaki, and S. Okazaki, *J. Phys. D: Appl. Phys.* **21** (1988) 1838

[78] K.G. Donohoe and T. Wydeven, *J. Appl. Polymer Sci.* **23** (1979) 2591

[79] T. C. Manley, *Trans. Electrochem. Soc.* **84** (1943) 83

[80] Z. Falkenstein and J.J. Coogan, *J. Phys. D: Appl. Phys.* **30** (1997) 817

[81] U. Kogelschatz, Advanced ozone generation, in Process Technologies for Water Treatment (S. Stucki, ed.), Plenum Press, New York, NY (1988), pp. 87–120

[82] C. Hudon, R. Bartnikas, and M. R. Wertheimer, *IEEE Trans. Elect. Insulation*, **28** (1993) 1

[83] P.P. Woskov, D.Y. Rhee, P. Thomas, D.R. Cohn, J.E. Surma, C.H. Titus, *Rev. Sci. Instrum.* **67** (1996) 3700

[84] K. Pochner, W. Neff, R. Lebert, *Surf. Coat. Technol.* **74** (1995) 394

[85] C. Penache, M. Miclea, A. Bräuning-Demian, O. Hohn, S. Schössler, T. Jahnke, K. Niemax and H. Schmidt-Böcking, *Plasma Sources Sci. Technol.* **11** (2002) 476

[86] E.A.H. Timmermans, M.J. van de Sanden and J.J.A.M. van der Mullen, *Plasma Sources Sci. Technol.* **12** (200) 324

[87] R.G. Daniel, K.L. McNesby and A.W. Miziolek, *Appl. Opt.* **35** (1996) 4018

[88] N. Beverini, G. Cicconi, G.L. Genovesi and E. Piano, *Plasma Sources Sci. Technol.* **6** (1997) 185

[89] J. Luque, M. Kraus, A. Wokaun, K. Haffner, U. Kogelschatz, and B. Eliasson, *J. Appl. Phys.* **93** (2003) 4432

[90] J.M. Williamson, P. Bletzinger and B.N. Ganguly, *J. Phys. D: Appl. Phys.* **37** (2004) 1658

[91] S. Pellerin, J.M. Cormier, F. Richard, K. Musiol, J. Chapelle, *J. Phys. D: Appl. Phys.* **29** (1996) 726

[92] C. de Izarra, *J. Phys. D; Appl. Phys.* **33** (2000) 1697

[93] S.Y. Moon, W. Choe, H.S. Uhm, Y.S. Hwang, J.J. Choi, *Phys. Plasmas* **9** (2002) 4045

[94] O. Motret, C. Hibert, S. Pellerin, J.M. Pouvesle, *J. Phys. D: Appl. Phys.* **33** (2000) 1493

[95] P.W.J.M. Boumans, Inductively Coupled Plasma Emission Spectroscopy Part 2, John Wiley & Sons, New York, 1987, Chap. 10.

[96] G.H. Dieke, H.M. Crosswhite, *J. Quant. Spectrosc. Radiat. Transfer.* **2** (1962) 97

[97] M. Touzeau, M. Vialle, A. Zellagui, G. Gousset, M. Lefebvre, M. Pealat, *J. Phys. D: Appl. Phys.* **24** (1991) 41

[98] J.M. Workman, P.A. Fleitz, H.B. Fannin, J.A. Caruso, C.J. Seliskar, *Appl. Spectroscopy* **42** (1988) 96

[99] D. Robinson, *J. Quant. Spectrosc. Radiat. Transfer* **4** (1964) 335

[100] S. Ishihara, A. Otsuka and S. Nagata, *Appl. Phys. Lett.* **55** (1989) 2396

[101] A. Okada and K. Kijima, *J. Phys. D: Appl. Phys.* **35** (2002) 2126

[102] N.N. Sobolev, Electron-excited molecules in nonequilibrium plasma, Proc. Lebedev Physics Institute vol 179 (Supplemental vol 2) (Commack, New York: Nova Science) (1989)

[103] B. Benstaali, P. Boubert, B.G. Cheron, A. Addou and J.L. Brisset, *Plasma Chem. Plasma Process.* **22** (2002) 553

[104] B. Michelt, G. Lins and R.J. Seeböck, *J. Phys. D: Appl. Phys.* **28** (1995) 2600

[105] P. Macko and P. Veis, *J. Phys. D: Appl. Phys.* **32** (199) 246

[106] A. Chelouah, E. Marode, G. Hartmann and S. Achat, *J. Phys. D: Appl. Phys.* **27** (1994) 940

[107] A. Chelouah, E. Marode and G. Hartmann, *J. Phys. D: Appl. Phys.* **27** (1994) 770

[108] K. Slahi, L. Hochard and A.M. Pointu, *Meas. Sci. Technol.* **4** (1993) 685

[109] H. Nassar, K. Meguernes, A. Czernichowski and J. Chapelle, *Proc. 12th Int. Symp. on Plasma Chemistry, ISPC12* (Minnesota, USA) vol 2 (1995) p 651

[110] S. Pellerin, K. Musiol, O. Motret, B. Pokrzywka and J. Chapelle, *J. Phys. D: Appl. Phys.* **29** (1996) 2850

[111] C. Vivien, J. Hermann, A. Perrone, C. Boulmer-Leborgne and A. Luches, *J. Phys. D: Appl. Phys.* **31** (1998) 1263

[112] J.S. Kim and M.A. Cappelli, *J. Appl. Phys.* **84** (1998) 4595

[113] J. Luque, W. Juchmann, E.A. Brinkmann, and J. B. Jeffries, *J. Vac. Sci. Technol. A* **16** (1998) 397

[114] C. Vivien, J. Hermann, A. Perrone and C. Boulmer-Leborgne, *J. Phys. D: Appl. Phys.* **32** (1999) 518

[115] S. Acquaviva, A.P. Caricato, M.L. de Giorgi, G. Dinescu, A. Luches and A. Perrone, *J. Phys. B: At. Mol. Opt. Phys.* **30** (1997) 4405

[116] K. Kutasi, Z. Donkó, M. Mohai, L. Nemes and G. Marosi, *Vacuum* **68** (2003) 311

[117] S. Stamou, D. Mataras and D. Rapakoulias, *J. Phys. D: Appl. Phys.* **31** (1998) 2513

[118] H. Nassar and A. Czernichowski, *J. Phys. Coll.* **51** (1990) 289

[119] C.O. Laux, R.J. Gessman, C.H. Kruger, F. Roux, F. Michaud and S.P. Davis, *Quant. Spectrosc. Radiat. Transfer* **68** (2001) 473

[120] A. Czernichowski, *J. Phys. D: Appl. Phys.* **20** (1987) 559

[121] J. Röpcke and A. Ohl, *Contrib. Plasma Phys.* **34** (1994) 575

[122] A.N. Goyette, W.B. Jameson, L.W. Anderson and J.E. Lawler, *J. Phys. D: Appl. Phys.* **29** (1996) 1197

[123] D.M. Phillips, *J. Phys. D: Appl. Phys.* **9** (1976) 507

[124] J.P. Novak and R. Bartnikas, *IEEE Trans. Plasma Science*, **19** (1991) 95

[125] A. Ricard, Ph. Décomps, F. Massines, *Surf. and Coatings Technol.* **112** (1999) 1

[126] G. Herzberg, "I. Spectra of Diatomic Molecules", 2nd edn., New York, Van Nostrand (1950)

[127] B. Massabieaux, A. Plain, A. Ricard, M. Capitelli, and C. Gorse, *J. Phys. B: At. Mol. Opt. Phys.* **16** (1983)

[128] S.P. Brühl, M.W. Russell, B.J. Gómez, G.M. Grigioni, J.N. Feugeas, and A. Ricard, *J. Phys. D: Appl. Phys.* **30** (1997) 2917

[129] J.M. Pouvesle, A. Bouchoule and J. Stevefelt, *J. Chem. Phys.* **77** (1982) 817

[130] A. Lofthus and P.H. Krupenie, *J. Phys. Ref. Data* **6** (1977) 1

[131] K.A. Dick, W. Benesch, H.M. Crosswhite, S.G. Tilford, R.A. Gottscho, and R.W. Field, *J. Molec. Spectrosc.* **69** (1978) 95

[132] G. Nersisyan, B. Fox, T. Morrow and W.G. Graham, *38th Int. Universities Power Engineering Conf., UPEC 2003* (Thessaloniki, Greece), Conference Proceedings (2003) 69

[133] G Nersisyan and W G Graham, *Plasma Sources Sci. Technol.* **13** (2004) 582

[134] K.V. Kozlov, H.-E. Wagner, R. Brandenburg and P. Michel, *J. Phys. D: Appl. Phys.* **34** (2001) 3164

[135] http://www.mksinst.com/techmassflofaq.html

[136] A.N. Goyette, J.R. Peck, Y. Matsuda, L.W. Anderson and J. E. Lawler, *J. Phys. D: Appl. Phys.* **31** (1998) 1556

[137] N.K. Bibinov, A.A. Fateev, K. Wiesemann, *J. Phys. D: Appl. Phys.* **34** (2001) 1819

[138] M.R. Wertheimer, I. Radu, R. Bartnikas, *Proc. 12th Int. Sym. On Electrets (ISE12),* Salvador, Brazil, sept. 2005, pp. 231-234

[139] R.H. Fowler and L.W. Nordheim, *Proc. Roy. Soc. (London)* **A124** (1929) 699

[140] F.F. Chen, "Introduction to Plasma Physics", Plenum Press, New York (1974), p. 256

[141] J.H. Kim, Y.H. Kim, Y.H. Choi, W. Choe, J.J. Choi, Y.S. Hwang, *Surf. Coatings Technol.* **171** (2003) 211

[142] S.Y. Moon, W. Choe, *Spectrochim. Acta B* **58** (2003) 249

Appendix A Evaluation of the voltage across the gap

The equivalent circuit of a DBD (Fig. 1.13) permits one to determine the voltage across the gas gap as a function of the other parameters that can be measured or theoretically evaluated, under the hypothesis that the discharge covers the entire dielectric surface:

$$u_{appl}(t) = u_d(t) + u_g(t) + u_T(t) + u_R(t) \tag{A.1}$$

where $u_R(t) = i_d(t).R$ is the voltage across the resistor R, $u_d(t)$ is the voltage across the dielectric, C_d, and $u_g(t)$ is the voltage across the gas gap [25, 132]. In order to determine the voltage across the dielectric a capacitor must be introduced into the circuit between the lower metallic electrode and the resistor R. The voltage across the capacitor C, given by the equation:

$$u_T(t) = \frac{1}{C}\int_0^t i_d(t')\,dt' = \frac{q(t)}{C} \tag{A.2}$$

permits one to determine $u_d(t)$ [133].

During a uniform or filamentary discharge the charged species are transferred to the electrode surfaces. On a dielectric surface, charges transferred from the discharge persist for a longer time than from one discharge to another in the next half-cycle, because the dielectric has become a capacitor. The charge accumulated on the dielectric surface influences the voltage across the gas gap and can be written:

$$u_m(t) = u_d(t) + u_m(t_0) \tag{A.3}$$

where $u_m(t_0)$ is the voltage determined by the charge accumulated on the dielectric surface from the previous discharge (the charge has apposite polarity). Then, the voltage across the gap is given by

$$u'_m(t) = u_{appl}(t) - u_m(t) \tag{A.4}$$

From equation (A.4) it results that even when the voltage applied to the electrodes is zero, the voltage across the gap has a non-zero value, determined by the charge accumulated on the dielectric surface (or two dielectric surfaces), so that the next breakdown is produced earlier and at a lower applied voltage than under normal conditions (without any charge on the dielectric surface) [133].

Appendix B Calculation of the gas flow correction factor

For the case of gas mixtures, the calculated gas correction factor (GCF) of the mass flow controllers (MFC) are not simply the weighted averages of each component's GCF. Instead, the GCF (relative to nitrogen) is calculated by the following expression (for the general case of a mixture of n gases) [135]:

$$GCF = \frac{0.3106(a_1 s_1 + a_2 s_2 + \ldots + a_n s_n)}{a_1 d_1 c_{p1} + a_2 d_2 c_{p2} + \ldots + a_n d_n c_{pn}} \tag{B.1}$$

Here, a_1 through a_n are the fractional flow values of gases 1 through n; s_1 through s_n are the molecular structure factors; d_1 through d_n are the densities at STP; and c_{p1} through c_{pn} are the specific heats at constant pressure. Values for s, d, and c_p are tabulated for most gases, and many are listed in our MFC manuals. The values for a_1 through a_n will depend upon the application (remember that a_1 through a_n must add up to 1.0). Molecular Structure correction factor(s) are as follows:

- 1.030 for monoatomic gases (e.g. He, Ar, ...);
- 1.000 for diatomic gases (e.g. N_2, O_2, H_2, ...);
- 0.941 for triatomic gases (e.g. CO_2, ...);
- 0.880 for polyatomic gases (four or more atoms, e.g SiH_4, CH_4, NH_3, ...).

For example:

Gas 1 = argon at 150 sccm

Gas 2 = nitrogen at 50 sccm

$$\begin{aligned} &a_1 = \frac{150}{200} = 0.75,\ a_2 = \frac{50}{200} = 0.25 \\ &s_1 = 1.030,\ s_2 = 1.000 \\ &d_1 = 1.782\,g/l,\ d_2 = 1.250\,g/l \\ &c_{p1} = 0.1244\,cal/g^oC,\ c_{p2} = 0.2485\,cal/g^oC \\ &\rightarrow GCF = 1.302 \end{aligned} \tag{B.2}$$

Appendix C Spatio-temporal studies of APGD in Ne

As also reported by Radu *et al* [21], neon gas has very similar APGD behaviour to that of its helium counterpart, namely a single multi-μs current pulse per half-cycle of the applied (multi-kHz) a.c. high voltage. Nitrogen gas, too, is known to present APGD behaviour, but as pointed out by Massines and coworkers [33], the physics underlying N_2 APGD differs from that of He and Ne. In the present appendix (Appendix C) and the following one (Appendix D), we describe certain APGD experiments carried out in atmospheric pressure flows of Ne and N_2, respectively. Figure C.1 depicts "long-duration" exposure side-view images of three APGD events in a 5.6 slm flow of Ne gas, in a d = 3.0 mm needle-plane electrode configuration. We can distinguish two types of behaviours: the first, Figs. C.1 (a) and (b), between the needle (of 40 μm radius) and a dielectric surface, and a second distinct type (Fig. C.1 (c)) when the dielectric material was coated, on its top surface, too, with a metal at floating potential. Around the needle tip, luminosity was more intense, as in He (see section 3.1), for the same reasons. Also like in the case of He, luminous emission occurred in the vicinity of the dielectric surface, but of lower intensity, as in mid-gap. However, the discharge in Fig. C.1(c) between two metallic surfaces was quite different, with very little radial spreading. This too, had been reported in the case of He, in a similar experiment by Radu *et al* [28].

(a) (b) (c)

Figure C.1 "Long-duration" exposure images of Ne APGD in a d = 3.0 mm needle-plane gap. In each of the three cases a different dielectric has been used as the lower (grounded) electrode: (a) Al_2O_3, (b) glass, and (c) a metallic layer at floating potential superimposed on the Al_2O_3 dielectric surface.

"Film" sequences of Ne APGD in the 3.0 mm needle-plane gap during the positive half-cycle are shown in Fig. C.2 for glass (a) and Al_2O_3 (b), while the corresponding I-t maps are presented in Figs. C.3 (a) and (b). The exposure time of each image in Fig C.2 was 10 ns (1000

accumulations). The "PM" signals corresponding to the discharge events in Figs. C.2 and C.3 are presented in Fig. C.4 (a) and (b), and may be compared with their counterparts for APGD in He, in the

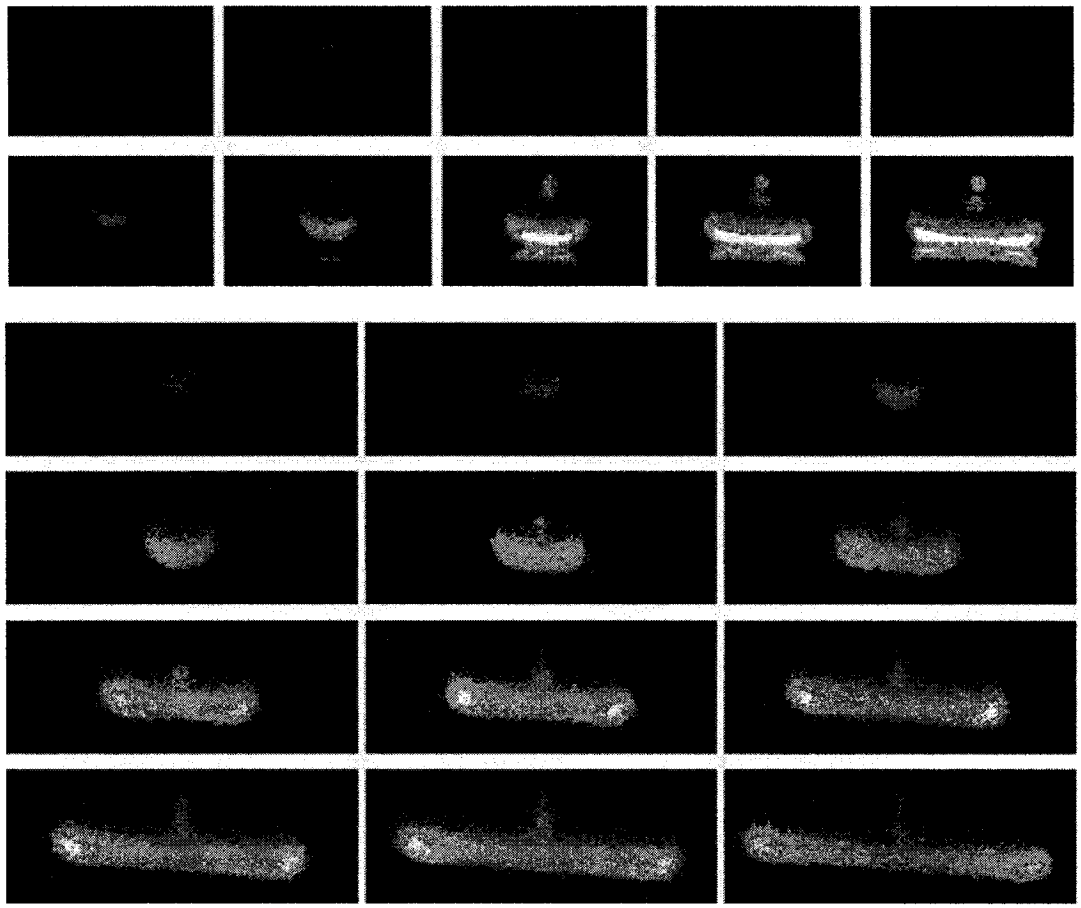

Figure C.2 "Film" sequences showing axial propagation of a Ne APGD during the positive half-period of the applied voltage, for two different dielectric surfaces: (a) glass and (b) Al_2O_3. Each image corresponds to an exposure time of 10 ns, and the time between consecutive images is 100 ns. The discharge occurred in a 3.0 mm gap between a needle (40 μm radius) and a dielectric (glass/ITO).

positive half-cycle of the needle-plane discharge pulse, Fig 3.5 (a) and Fig. 3.7 (a), respectively. Several similarities, but also significant differences, emerge from the comparisons of the two cases corresponding to the Al_2O_3 dielectric surfaces, namely:

(i) In both He and Ne the time taken for the discharge front to propagate from the needle tip to the dielectric surface, τ_p, is much less than the time for the PM intensity, I, to reach its maximum, τ_m.

(ii) For the case of the Al_2O_3 dielectric, τ_p and τ_m values for He and Ne were:

He: $\tau_p \approx 2$ μs, $\tau_m \approx 10$ μs,

Ne: $\tau_p \approx 3$ μs, $\tau_m \approx 9$ μs.

(iii) However, the I-t maps (Figs. 3.5 (a) and C.3 (b)) are clearly quite different in the two cases, Ne displaying longer-lasting luminous emission from the mid-gap region after propagation of the front.

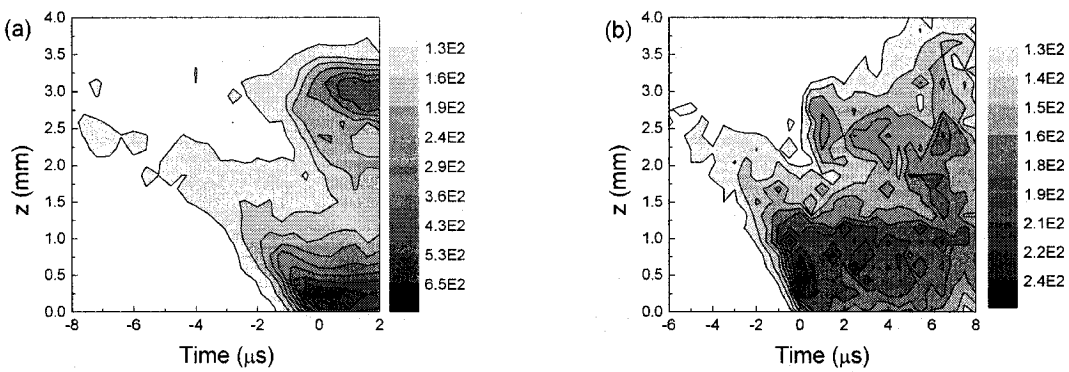

Figure C.3 The axial spatio-temporal distributions of total light emission intensity, I, from APGD in Ne in a 3.0 mm needle-plane gap recorded during the positive half-cycle, when the grounded dielectric electrode was (a) glass, and (b) Al_2O_3; the dielectric surface corresponds to z = 0, the needle tip to z = 3.0 mm.

Comparing glass and Al_2O_3 counterparts ((a) and (b), respectively, of Figs C.3 and C.4), we note subtle differences in the behaviours of Ne APGD for those two dielectric surfaces: τ_p appears to be of shorter duration in the case of glass (~ 2 μs, vs 3 μs for Al_2O_3), and I-t maps differ somewhat. This is probably related to higher surface conductivity for glass, which permits charges deposited on the surface to spread more rapidly [138]. This interpretation appears to be confirmed by Fig. C.5, the I-t map for the case of the metallized surface at floating potential (see also Fig. C.1 (c)), for which $\tau_p < 1$μs, as had also been reported by Radu *et al* for the case of He [28].

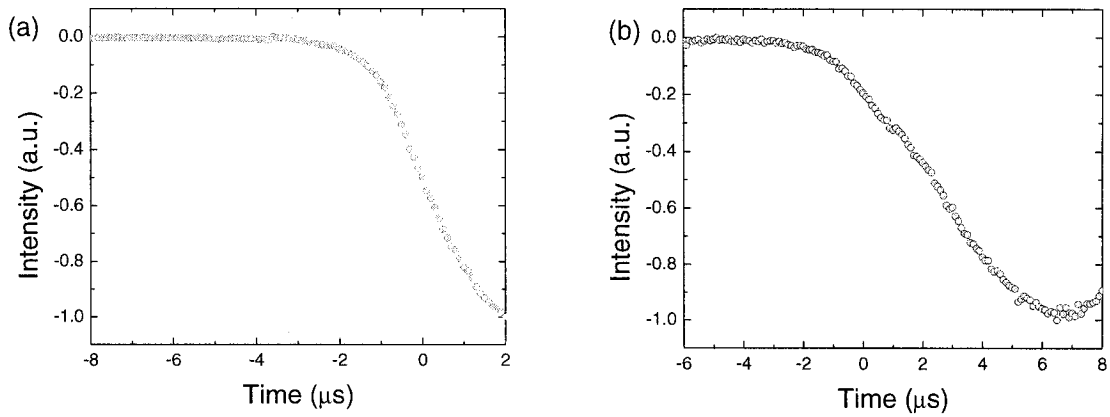

Figure C.4 The PM signals that correspond to the discharge events in Figs. C.2 and C.3.

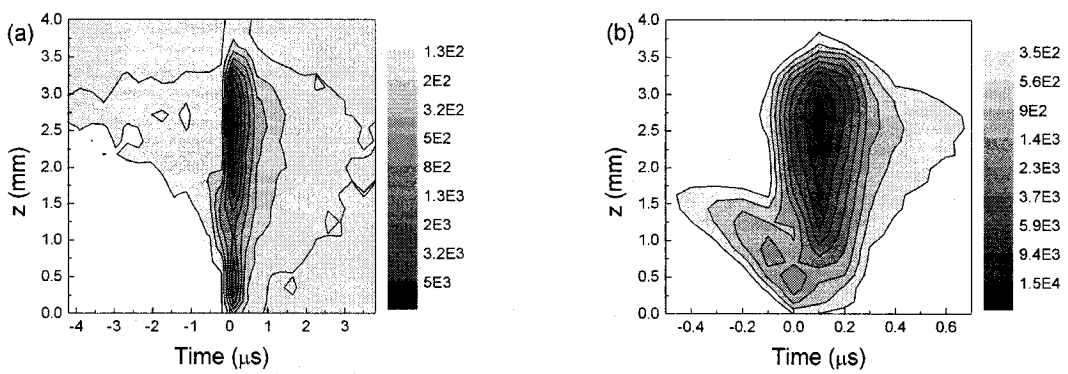

Figure C.5 The axial spatio-temporal distributions of total light emission intensity, I, from APGD in Ne in a 3.0 mm needle-plane gap recorded during the positive half-cycle, when the planar surface was metal at floating potential that covered the Al_2O_3 dielectric surface: (a) the entire discharge sequence, (b) expanded time scale during discharge propagation.

Appendix D Spatio-temporal studies of APGD in N_2

Figure 1.5 shows the well-known characteristics of APGD in pure N_2 gas [21, 25, 33], namely a single long-duration (tens of μs) current pulse per half-cycle, for the case of a plane-plane electrode configuration. As reported by Massines *et al* [33], however, N_2 "APGD" can also manifest a filamentary nature under certain conditions. Figure D.1 shows examples of "long-duration" exposure images in flowing pure N_2 gas for the case of different electrode geometries:

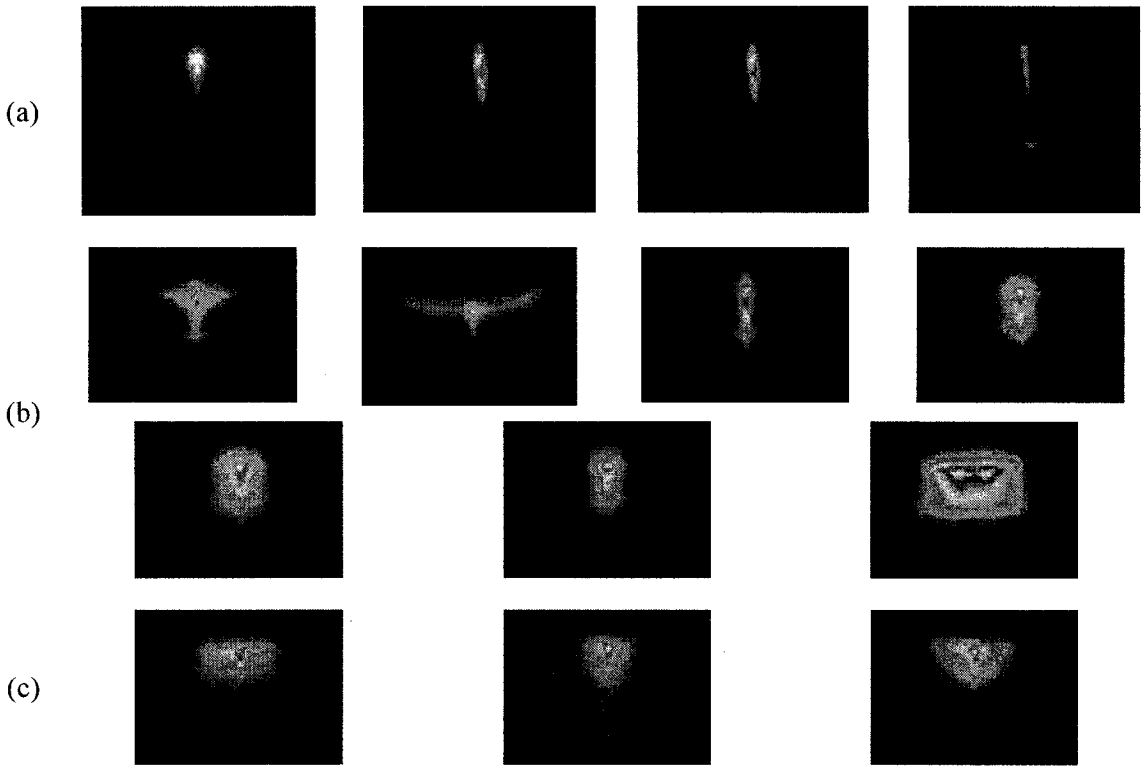

Figure D.1 Examples of "long-duration" exposure images from N_2 atmosphere pressure discharges produced in (a) 3.0 mm gap needle-plane configuration; (b) 1.0 mm gap, and (c) 0.5 mm gap in the sphere-plane configuration (pure N_2 flow rate 4 slm, f = 10 kHz).

(a) shows a series of (positive half-cycle) discharge events in d = 3.0 mm needle-plane geometry, while (b) and (c) represent the cases of d = 1.0 and 0.5 mm sphere-plane geometries, respectively, the planar (low-potential) electrode having been MgO dielectric in all cases. The dominant feature emerging from Fig D.1 is the fact that the luminous patterns were not

reproducible from one event to the other, contrary to the cases of He and Ne presented earlier in this document: even in the sphere-plane cases, the discharges could become "filamentary" (see Fig D.1 (b)), although all parameters (V_{pp}, gas flow rate, f, etc.) were maintained rigorously constant.

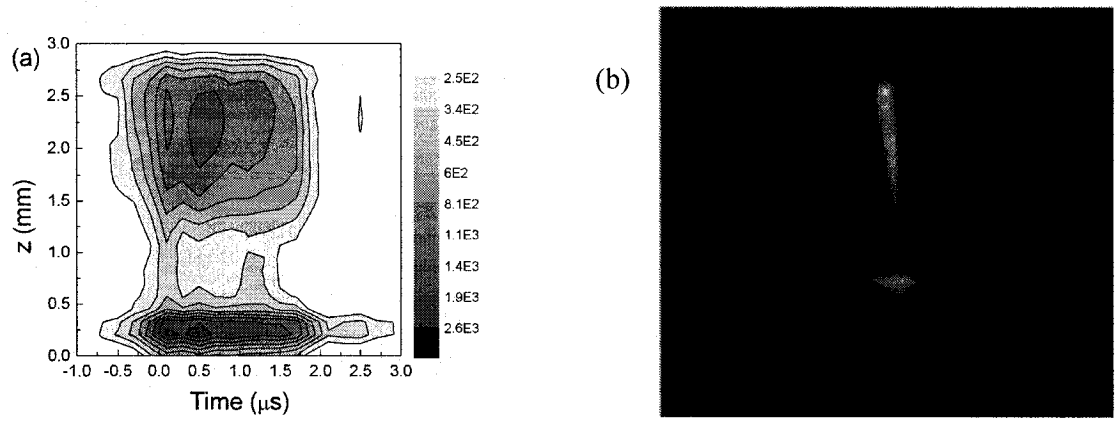

Figure D.2 (a) Total light emission intensity, I, from a N_2 discharge at atmospheric pressure in a 3.0 mm needle-plane gap; (b) "long-duration" exposure image for the same discharge event. The dielectric surface (MgO in this case) corresponded to z = 0.

Figures D.2 and D.3 correspond to the d = 3.0 mm needle-plane and the d = 0.5 mm sphere-plane discharges in pure, flowing N_2, respectively, again during positive half-cycles. The I-t map, Fig. D.2 (a) bore witness to both longer-term (multi-μs) luminosity in the region $1.0 \leq z < 3.0$ mm, but short-term (sub-μs) "filamentary" characteristics for $z \leq 1.0$ mm. On the other hand, Figs. D.3 (a) and (b) manifested stable patterns of luminous emission, both axially (z direction, (a)) and radially (r direction, (b)) over periods well in excess of 10 μs, characteristics of a true "atmospheric pressure glow discharge (APGD)". It is noteworthy (see t = 0 on Fig. D.3 (a)) that the discharge appeared to initiate in the mid-gap region, not near an electrode.

Finally, Fig. D.4 (a) and (b) respectively show I-t maps corresponding to the "z" and "r" directions of a d = 0.5 mm sphere-plane N_2 discharge during the negative polarity half-cycle. As discussed earlier in this text and in various articles [21, 22, 29-31], the discharge characteristics can differ very considerably between the positive and negative half-cycle in highly asymmetric electrode configurations; comparing Figs. D.3 and D.4 shows that this is very much the case here, too: Contrary to the long-duration (~ 30 μs) luminous event during the positive half-cycle,

its duration was only ~ 1 μs during negative polarity, the actual propagation of the discharge front being ultra-rapid (≤ 0.2 μs).

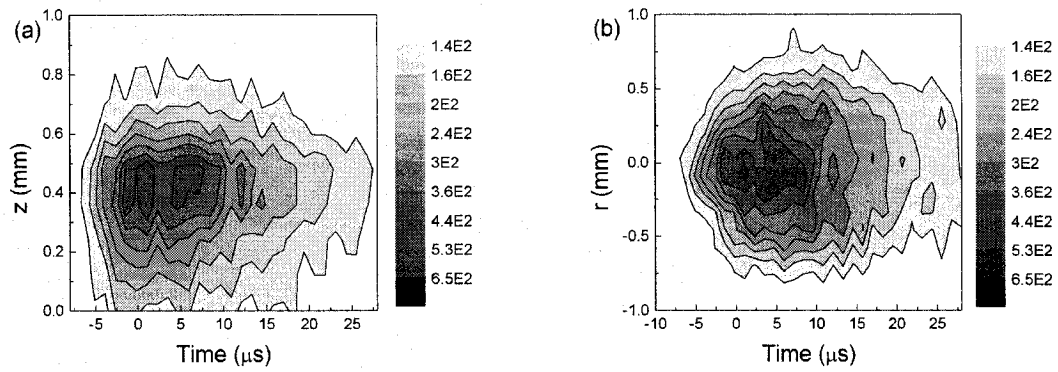

Figure D.3 Total light emission intensity, I, from APGD in N_2 in a 0.5 mm sphere-plane gap during the positive half-cycle: (a) along the discharge axis at r = 0; (b) the radial distribution at z ≈ 0.5 mm. The MgO dielectric surface corresponded to z = 0 (N_2 flow rate 4 slm, f = 10 kHz, V_{pp} = 8 kV).

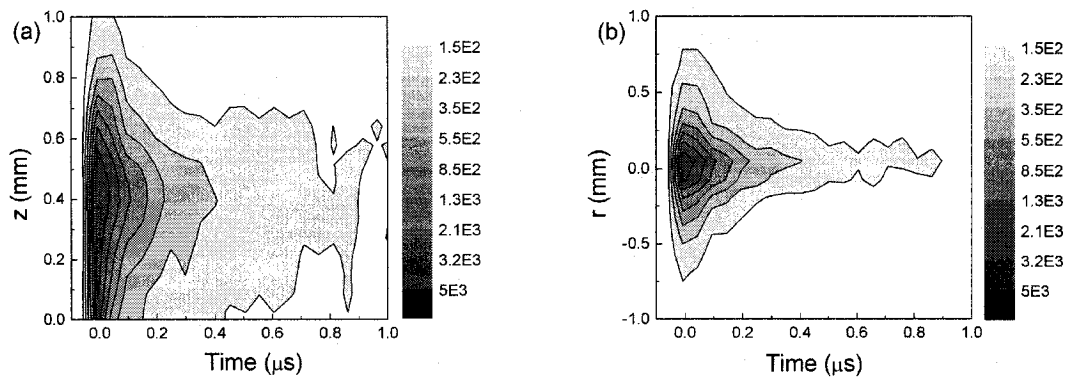

Figure D.4 Total light emission intensity, I, from APGD in N_2 in a 0.5 mm sphere-plane gap during the negative half-cycle: (a) along the discharge axis at r = 0; (b) the radial distribution at z ≈ 0.5 mm. The MgO dielectric surface corresponded to z = 0 (N_2 flow rate 4 slm, f = 10 kHz, V_{pp} = 8 kV).